THE MECHANISMS EXPLAINING THE EAST ASIAN SUMMER MONSOON (EASM) RESPONSE TO GLOBAL CLIMATE CHANGE

by

Yan Jin
A Dissertation
Submitted to the
Graduate Faculty
of
George Mason University
In Partial fulfillment of
The Requirements for the Degree
of
Doctor of Philosophy
Climate Dynamics

Committee:

______________________ Dr. Cristiana Stan, Dissertation Director

______________________ Dr. David Straus, Committee Member

______________________ Dr. V. Krishnamurthy, Committee Member

______________________ Dr. Joseph Weingartner, Committee Member

______________________ Dr. Edwin Schneider, Department Chair

______________________ Dr. Donna M. Fox, Associate Dean, Office of Student Affairs & Special Programs, College of Science

______________________ Dr. Peggy Agouris, Dean, College of Science

Date: ______________________ Summer Semester 2016
George Mason University
Fairfax, VA

The Mechanisms Explaining the East Asian Summer Monsoon (EASM) Response to Global Climate Change

A dissertation submitted in partial fulfillment of the requirements for the degree of Doctor of Philosophy at George Mason University

By

Yan Jin
Bachelor of Science
Nanjing University of Information Science and Technology, China, 2010

Director: Dr. Cristiana Stan, Associate Professor
Department of Atmospheric, Oceanic, and Earth Sciences

Summer Semester 2016
George Mason University
Fairfax, VA

Dedication

To Mom and Dad,
who guide me to where I am today.

To my husband, Suhao Qin.
For his love and encouragement.

To my daughter, Katherine.
For her amazing accompaniment towards the end of my Ph.D. study.

Acknowledgments

Firstly I would like to give my special thanks to my advisor, Dr. Cristiana Stan, for all her guidance, support, patience, encouragement, and help that she has provided throughout my graduate study. Also for her positive, confident, and optimistic attitude, which will benefit me the whole life.

I would also like to thank the rest of my dissertation committee, Dr. V. Krishnamurthy, Dr. David Straus, and Dr. Joseph Weingartner, for their time and helpful suggestions and advice to my research and dissertation.

I also thank Dr. Barry Klinger and Dr. Jagadish Shukla, for offering me the opportunity to study in the department of Climate Dynamics and work with so many great professors. I appreciate their help and support during the last four and half years. I would like to thank the faculty of the Climate Dynamics department for their generously imparting knowledge to me. I thank my classmates for our corporations and discussions on scientific problems. I also thank my friends for their encouragement and friendship.

This work has been supported by the Regional and Global Climate Modeling Program funded by U.S. Department of Energy, Office of Science under award number SC0006722, and by the National Science Foundation and Technology Center for Multi-scale Modeling of Atmospheric Processes managed by Colorado State University under cooperative agreement No. ATM-0425247. This research used resources of the National Energy Research Scientific Computing Center, which is supported by the Office of Science of the U.S. Department of Energy under Contract No. DE-AC02-05CH11231 and the Extreme Science and Engineering Discovery Environment (XSEDE), which is supported by National Science Foundation grant number OCI-1053575. I would like to thank all the scientists and software engineers who contributed to the development of the CCSM4 and the super-parameterization. I appreciate the comments on the manuscript by Dr. V. Krishnamurthy and Nicholas Lybarger.

Table of Contents

List of Tables

List of Figures

Abstract

THE MECHANISMS EXPLAINING THE EAST ASIAN SUMMER MONSOON (EASM) RESPONSE TO GLOBAL CLIMATE CHANGE

Yan Jin, PhD

George Mason University, 2016

Dissertation Director: Dr. Cristiana Stan

The mechanisms responsible for the East Asian Summer Monsoon (EASM) changes in a global warming scenario are investigated. Previous studies have shown that the EASM response to a warmer climate is primarily caused by the changes in western North Pacific Subtropical High (WNPSH), and the variations of WNPSH is attributed to the mean state of boundary conditions. However, none of these studies analyzed the impact of the remote air-sea interactions over tropical areas on the WNPSH. The main objective of this study is to investigate this remote air-sea interaction mechanism.

The EASM simulation under present climate using Super-Parameterized CCSM4 (SP-CCSM4) is firstly evaluated. SP-CCSM4 is a coupled climate model which implements a new representation of cloud-scale processes. It reveals that SP-CCSM4 captures the main features of observed EASM climatology, as well as the mechanisms associated with the northward propagation of the intraseasonal oscillation. Additionally, SP-CCSM4 has a higher model skill in simulating the mean state and annual cycle of the EASM than the conventionally-parameterized CCSM4.

The response of the EASM under the global warming scenario is analyzed using SP-CCSM4. In the future warmer climate the mean state of the EASM is intensified, with

enhanced precipitation and stronger monsoon circulation. The Mei-yu season has longer duration, and the precipitation over northern EASM domain is intensified and persists longer. The interannual variability of the EASM is amplified, with enhanced precipitation over northern East Asia.

Due to the influence of the WNPSH on the EASM, the mechanisms responsible for the changes of WNPSH in the warmer climate are essential to understand the mechanisms explaining the EASM variations. Based on the analysis of the EASM simulation under various warming scenarios, a remote air-sea interaction mechanism is proposed. It reveals that the changes in the WNPSH in the warmer climate are due to two factors: the warming of the boundary conditions, and the convective activities over tropical South China Sea (SCS) and West Pacific Ocean (WP). The warming of the boundary conditions is more important than the atmospheric warming, and it favors the WNPSH extend westward in the warmer climate. At meantime, the weak (strong) convection over tropical SCS and WP favors (inhibits) the westward extension of the WNPSH.

In order to test this mechanism, two numerical experiments are designed. The control-type experiment tests how the ocean mean state influences the atmosphere, and the sensitivity-type experiment aims to prove that the weak convection over SCS and adjacent WP leads to the westward extension of the WNPSH. This mechanism is confirmed by analyzing the mean state and the interannual variability of the EASM in these model experiments. The weaker convective activity over tropical SCS and adjacent WP induces an anti-cyclonic circulation to its northwest, plus a Rossby wave train from tropical to mid-latitude Pacific Ocean. The westerly anomaly on the northern side of the anti-cyclonic circulation intensifies the prevailing westerly/southwesterly flow, amplifying the western edge of the WNPSH and strengthening the monsoon circulation, thus favoring the westward extension of the WNPSH. However, the impact of the convection over tropical area on the WNPSH persists from May to June. During July and August, the changes in the WNPSH are affected by the systems in mid-latitudes.

Chapter 1: Introduction

1.1 East Asian Summer Monsoon (EASM) in Observations

1.1.1 Mean State

The East Asian Monsoon is an important component of the global monsoon system (Ding, 1992; He et al., 2007; Tao and Chen, 1987; Wang et al., 2008). The well-known monsoon regions are Asia, Australia, Africa, and America. The boreal summer monsoon over East Asia, which is referred to as the East Asian Summer Monsoon (EASM), is a unique component of the Asian climate system due to its complicated land-sea distribution (Tao and Chen, 1987; Wang et al., 2005, 2008). The landmass has a "C" shape distribution, with the Eurasian Continent located to its west, the Maritime Continent and Australia to its south, and Pacific Ocean to its east. The EASM is also influenced by the Tibetan Plateau, the world's highest and largest plateau (Tao and Ding, 1981).

Figure 1.1 (Wang et al., 2005, Fig.1) shows the difference of the mean state of the precipitation and 925-hPa wind over the Asia-Australian monsoon regions between July-August and January-February. In boreal summer, the southeasterlies to the north of Australia flow across the equator, and change to southwesterlies in the Northern Hemisphere (cross-equatorial flow). The large amount of precipitation over the South China Sea (SCS) and the nearby West Pacific (WP) Ocean is referred to as the western North Pacific (WNP) monsoon trough (Wang et al., 2005). To the north of the WNP trough lies the subtropical monsoon trough, which is characterized by an east-west elongated rain belt extending from Central China to southern Japan. The subtropical monsoon trough forms when the warm, moist air from south meets the cold, dry air from mid-latitudes (Ding, 1992).

The strength, shape, and position of the western North Pacific subtropical high (WNPSH) influence the precipitation of the EASM system (Lu and Dong, 2001; Mao et al., 2010). The WNPSH links the tropical and extra-tropical circulations (Sun and Ying, 1999), and the low-level jet at the northwestern edge of WNPSH transports large amounts of moisture to the region to its north (Lu, 2001; Lu and Dong, 2001; Lu et al., 2008; Zhang et al., 2009). Also, the meridional shifts of WNPSH have been observed to be associated with the onset and retreat of the EASM (He et al., 2001; Lu and Dong, 2001; Yang and Sun, 2003; Zhang and Tao, 1999; Zhou et al., 2009). Therefore, the EASM is affected by the systems from tropics, subtropics, and mid-latitudes, which makes it a hybrid tropical-subtropical monsoon system.

The domain of the EASM varies from study to study. Sometimes it only covers subtropical East Asia (Wang et al., 2005, Fig.1) whereas other times it includes the SCS (Ding, 1992). In this study, we adopt the domain which covers both subtropical East Asia and SCS (110°E-140°E, 10°N-45°N) to emphasize the hybrid subtropical-tropical characteristics of EASM.

1.1.2 Onset and seasonal march

The earliest onset of the Asian Summer Monsoon occurs at the end of April or early May, and is characterized by an abrupt increase of precipitation in the central and southern Indochina Peninsula. By mid-May the precipitation extends to the SCS, triggering the breakout of the monsoon over the SCS region. After this sudden onset, the easterlies (westerlies) at lower-level (upper-level) rapidly reverse direction to westerlies (easterlies). Meanwhile, the dry season switches to wet season, initiating the rainy season over Asian-North Pacific monsoon region (Ding and Chan, 2005; Ding et al., 2005; He, 2009).

The changes in precipitation associated with the sudden onset of Asian Summer Monsoon is illustrated in Figure 1.2. Over East Asia, there are two rain bands before mid-May. One is located at tropics (15°S-10°N), and the other one at subtropics (20°N-28°N). The subtropical rain band is called the pre-summer rainy season in South China (Lau et al., 1988). Around mid-May, the tropical rain belt suddenly jumps northward and merges with

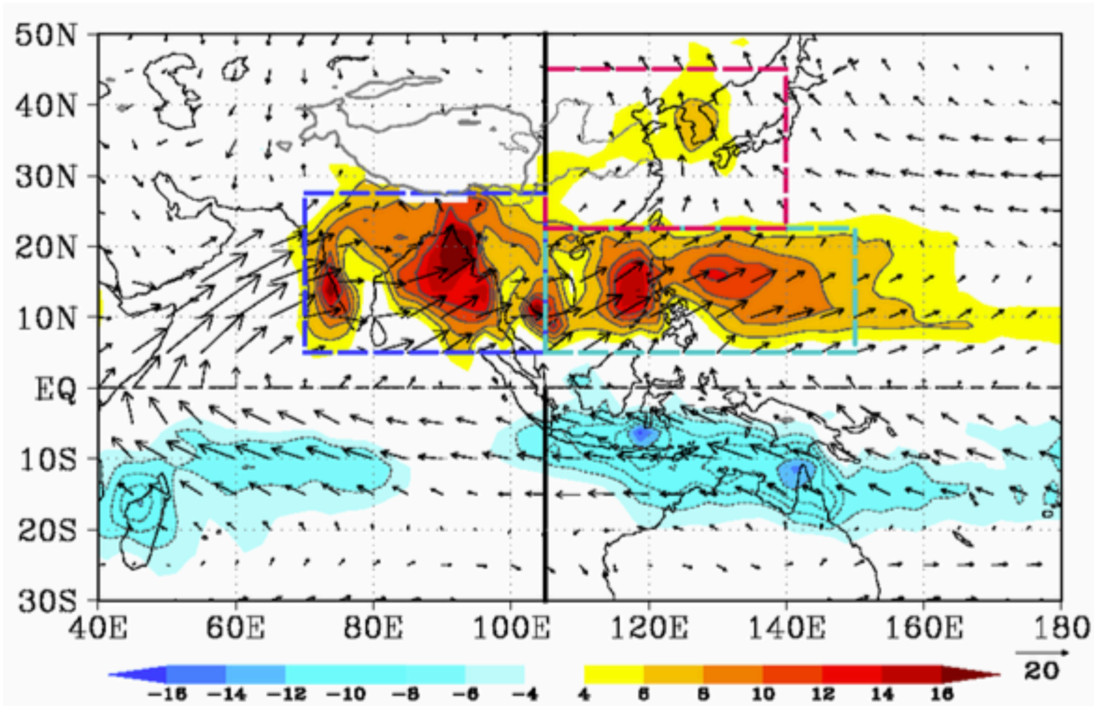

Figure 1.1: Difference in climatological precipitation rates (color shading in mm/day) and 925 hPa wind vectors (arrows) between the July-August and January-February in the Asian-Australian monsoon region. The precipitation and wind climatology are derived from CMAP (Xie and Arkin, 1997) (1979-2000) and NCEP/NCAR reanalysis (1951-2000), respectively. The three boxes define major summer precipitation areas of the Indian tropical monsoon (5°N-27.5°N, 65°E-105°E), western North Pacific tropical monsoon (5°N-22.5°N, 105°E-150°E), and the East Asian subtropical monsoon. *Figure from (Wang et al., 2005)*

the precipitation over South China, bringing large amounts of precipitation there. This process is accomplished within a short time period of about two weeks (Fig. 1.2). After the onset, the Asian-Pacific monsoon evolves into two systems: one system propagates northwestward to India, leading to the onset of the Indian Summer Monsoon (ISM), and the other propagates northward and northeastward to East Asia, leading to the EASM.

The seasonal advance of the EASM shows a stepwise northward propagation, which is characterized by two abrupt northward jumps and three standing stages (Ding and Chan, 2005; Ding et al., 2005). It is more clear to see this feature when only showing the precipitation over the subtropical region between April and September (Fig. 1.3). The first

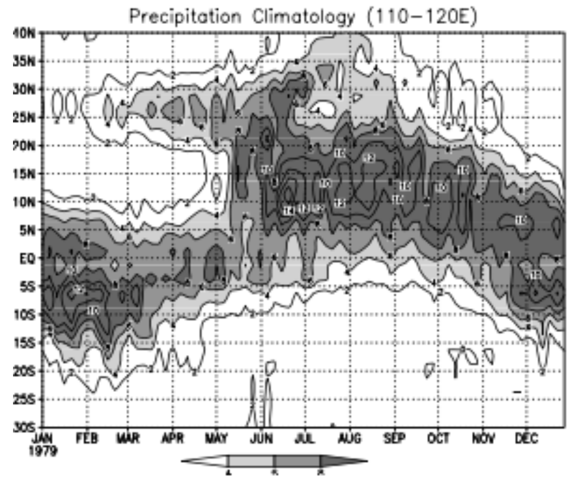

Figure 1.2: Latitude-time cross-sections of mean precipitation (1979-2001) along 110°E-120°E. The CMAP precipitation dataset is used here. Unit: mm/day. *Figure from (Ding and Chan, 2005)*

standing stage corresponds to the steep rise of precipitation over South China (18°N-25°N) starting from the first ten days of May. It generally lasts up to the first ten days of June. Afterwards, the rain belt jumps northward to Yangtze River valley and persists for around 20-30 days. This rainy episode represents the Mei-yu season and is also referred to as the second standing stage of the EASM seasonal march. From early or mid-July, the rain belt advances northward again to North China, reaching the northernmost position of EASM. This rainy episode lasts for around one month, which represents the third standing stage of the EASM seasonal march.

The Mei-yu rainy episode in the EASM's seasonal march is a unique feature among the monsoon systems (Ding and Chan, 2005; Ding et al., 2005). It is characterized by an elongated low-pressure trough extending from the Yangtze River valley to Korean Peninsula and Japan (reviews by Ding 1992; Ding and Chan 2005; Ding et al. 2005 provide a comprehensive description of these features). In different regions different terminologies have been used to denote this seasonal rain belt, for instance, Baiu in Japan and Changma in Korea. But there are regional difference in starting time and duration. In China, the Mei-yu season is usually referred to as the rainy episode over the Yangtze River valley from mid-June to

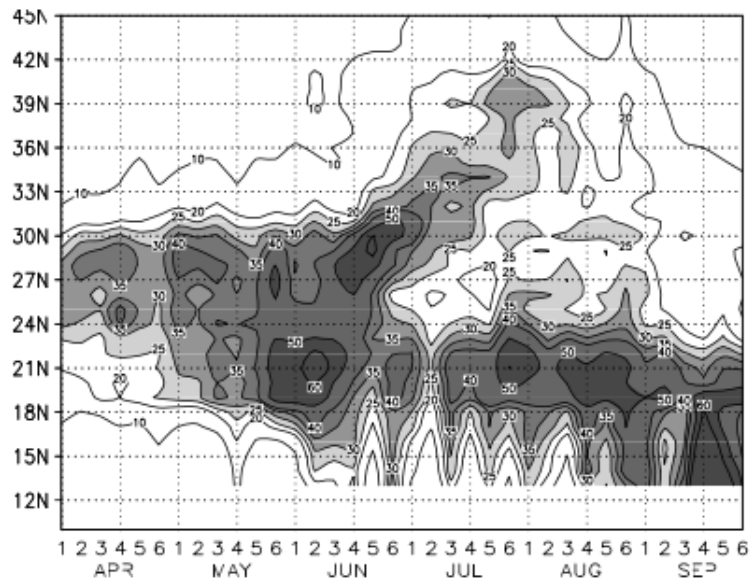

Figure 1.3: Latitude-time section of 5-day mean rainfall over eastern China (110°E-120°E) from April to September averaged for 1961-1990. Regions of heavy rainfall (>50 mm) are shaded. Unit: mm. *Figure from (Ding and Chan, 2005)*

mid-July (Ding et al., 2005; Tao and Chen, 1987), and this definition is adopted in this study.

1.1.3 Intraseasonal Variability (ISV) of the EASM

The intraseasonal variability (ISV) of the EASM is closely related to the advance and retreat of the EASM precipitation (Huang et al., 2003). The ISV of boreal summer is weaker and more complex than in boreal winter. It exhibits northward and westward propagation in addition to the underlying eastward Madden-Julian Oscillation (MJO) propagation. The ISV over SCS and East Asia has several contributions: It triggers the monsoon onset (Chan et al., 2002; Chen and Chen, 1995; Ju et al., 2005; Qian et al., 2002; Qian and Lee, 2000), modulates the active and break cycles of the rainy season (Wang and Xu, 1997), and connects the regional monsoon systems around SCS (Ding and Chan, 2005; Lau and Weng, 2002; Li and Zhang, 1999).

The ISV of EASM is in general characterized by two modes of variability: the 10-20-day mode (or the biweekly mode) (Xu and Zhu, 2002) and the 30-60-day mode (Ding and Chan, 2005; He et al., 2007; Xu and Zhu, 2002). The 30-60-day mode prevails over SCS and is characterized by the northward propagation of enhanced and suppressed convection, whereas the 10-20-day mode shows a westward migration of the cyclonic/anticyclonic systems from tropical WP to SCS (Mao and Chan, 2005).

The 30-60-day mode associated with EASM is generally referred to as the Intraseasonal Oscillation (ISO). The mechanisms proposed to explain the formation and propagation are attributed to the atmospheric internal dynamics (Drbohlav and Wang, 2005; Jiang et al., 2004; Wang et al., 2009) and to external influences, such as air-sea interactions (Hsu and Weng, 2001; Kemball-Cook and Wang, 2001; Mao et al., 2010; Tsou et al., 2005; Wang et al., 2009, 2000; Wang and Zhang, 2002; Zhang et al., 2009).

1.1.3.1 Air-Sea Interaction Mechanisms

Wang et al. (2009) divided the air-sea interaction theories into two categories: the propagating air-sea interaction theory and the stationary air-sea interaction theory. In both theories, a warm sea surface temperature (SST) anomaly leading the convective activity favors the propagation of convection.

The propagating air-sea interaction theory was initially developed for explaining the northward propagation of ISO in the Indian Ocean (IO) (Kemball-Cook and Wang, 2001), and later extended to the northward propagation of boreal summer ISO over WNP and SCS (Hsu and Weng, 2001; Wang et al., 2009). According to this theory, the heating associated with the convection over the equatorial eastern IO induces convectively coupled Kelvin and Rossby waves. The Kelvin waves generate abnormal easterly flow to the east of the convective anomaly, leading to the decrease (increase) of the southwesterly (southeasterly) wind in the northern (southern) tropics during boreal summer. The changes of the low-level circulation modify the upward latent heat flux (LHFLX) and thus change the thermal conditions over the tropics. The LHFLX decreases (increases) in the northern (southern) tropics favor the positive (negative) SST anomaly to develop over the northern (southern) tropics. Similarly, the Rossby waves induced by the ISV-related convection reduce the surface wind and increase SST over the northern tropics. At the same time, the small cloud cover to the north of convection allows the downward solar radiation to warm up the surface and destabilize the low-level atmosphere, thus favoring the northward propagation of ISO.

The stationary air-sea interaction supports the ISO by providing a restoring mechanism of the summer monsoon trough over SCS when perturbed by a high-pressure ISO anomaly. Wang and Zhang (2002) defined this restoring mechanism as the collective effects of two thermodynamic feedbacks: SST-cloud/radiation and SST-wind/evaporation, which change the high-pressure anomaly into a low-pressure anomaly. Over the monsoon trough area, the ISO-related high pressure anomaly reduces the surface wind and LHFLX loss, thus increases the SST and decreases the pressure there. When this high pressure anomaly disappears, the positive SST anomaly reaches the peak. The warming up of ocean surface induces convective anomaly, and lowers surface pressure.

1.1.3.2 Internal Dynamics Mechanism

The theories based on the atmospheric internal dynamics include the vertical shear mechanism (Drbohlav and Wang, 2005) and the boundary layer moisture-convection feedback mechanism (Jiang et al., 2004; Wang et al., 2009). The process associated with the vertical shear mechanism is the generation of a positive (negative) barotropic vorticity to the north (south) of the convection developing in a region dominated by vertical easterly wind shear. The barotropic vorticity aloft triggers the moisture convergence in the boundary layer to the north of the convection due to Ekman pumping, and favors the northward propagation of convection. In the moisture-convection feedback mechanism, the northward propagation of the convection is favored by the asymmetric distribution of the specific humidity in the meridional direction.

1.2 EASM Simulations in Previous Studies

1.2.1 Present Climate

The complex characteristics of EASM pose numerous challenges for numerical models, and most of the atmosphere-ocean general circulation models (AOGCMs) do not accurately simulate the spatial and/or intraseasonal variation of the monsoon precipitation (Randall et al., 2007).

Rajendran et al. (2004) analyzed the summer monsoon over South Asia, East Asia and WNP in the MRI-CGCM2. This model simulates many of the observed features of the South Asian summer monsoon and WNP summer monsoon, except for the EASM. The model underestimates the precipitation over Southeast China and simulates an earlier onset of EASM along with an earlier occurrence of the rainfall over Southeast China. In addition, the model fails to simulate the northward propagation of the monsoon rain belt. Kusunoki and Arakawa (2012) evaluated the June-July mean precipitation of EASM simulated by the models in the Coupled Model Intercomparison Project 3 (CMIP3) and found that most models underestimate the precipitation climatology and precipitation intensity over the East Asian region (110°E -150°E, 20°N -50°N).

Previous modeling studies have identified the horizontal resolution and the representation of convection as the main causes of these model biases. Sperber et al. (2013) noted that the multi-model mean of the CMIP5 models has a better simulation of seasonal mean precipitation, large-scale circulation, and boreal summer ISO than the CMIP3 multi-model mean. They attributed the improvements to the higher resolution of CMIP5 than CMIP3 models and different convective parameterizations. However, CMIP5 models still underestimate precipitation in the rainy season (Kusunoki and Arakawa, 2015), and Sperber et al. (2013) attribute the error to the weaker than observed cross-equatorial flow in the models. Zhou and Li (2002) used a resolution-varying atmospheric GCM with a local zoom centered on China, where the resolution was 1.5° (longitude) $\times$ 1° (latitude). The model captures the main characteristics of EASM such as the large-scale monsoon airflows and the cross equatorial southwesterly flow, but is unable to simulate most of the characteristics of the monsoonal precipitation. The observed heavy rain belt along the Yangtze River valley is missed in the simulation because the model produces a weaker than observed WNPSH and land-sea thermal contrast.

Chen et al. (2010) analyzed the ability of CAM3.5 to simulate the EASM and the sensitivity of the simulation to changes in the convection scheme. The simulation of the seasonal mean precipitation of EASM shows some improvements, but the magnitude of rainfall remains smaller than observed over the tropical and subtropical regions. Additionally, the seasonal march of precipitation does not improve with the changes in the parameterization of convective processes. For example, the subtropical rain belt is located at a higher latitude, the onset of the Mei-yu season begins three months earlier than in the observations, and the precipitation is overestimated and lasts longer in the northern part of the EASM region. The authors found that none of the changes in the parameterization of convection improves the simulation of the meridional monsoon circulation in the EASM region, which can be a source of error for the precipitation simulation.

1.2.2 Climate Change and EASM

As pointed out by the Fifth Assessment Report of the Intergovernmental Panel on Climate Change (IPCC AR5) (Stocker et al., 2013), the global-averaged surface temperature shows an increasing trend since the 1950s. This globally warming trend is highly related to the increased concentration of the greenhouse gases (Stocker et al., 2013). Under the global warming background, the changes of EASM has been observed in recent decades (e.g., Jiang and Wang, 2013; Li et al., 2010; Zhang et al., 2013; Zhang, 2015; Zuo et al., 2012). Several studies found that the changes in EASM precipitation shows a "southern-flooding-and-northern-drought" pattern (i.e. increased precipitation over southern China and decreased precipitation over northern China) (Hu et al., 2003; Xu, 2001; Yu and Zhou, 2007). Such pattern is considered as a weakening EASM (Wang, 2001; Zuo et al., 2012). This conclusion is in agreement with the findings by Jiang and Wang (2013), Xue (2001), and Zhu et al. (2012). However, other studies pointed out that the summer-time mean EASM does not show notable weakening or strengthening trend, but exhibits interannual-to-decadal fluctuations during recent decades (Li et al., 2010; Zhang et al., 2013; Zhang, 2015) (a detailed description of the decadal variability is summarized by Zhang, 2015).

The difference in the observed EASM changes during recent decades may be related to the definition of EASM intensity or the EASM index. For example, Li et al. (2010) defined the EASM intensity based on the area-averaged June-July-August (JJA) mean precipitation over tropical monsoon trough and subtropical monsoon trough. Zhang et al. (2013) used an WNP-EASM index (Wang et al., 2001), which is defined as the "difference of 850hPa westerlies between a southern region (5°-15°N, 100°-130°E) and a northern region (20°-30°N, 110°-140°E)". They both found that the EASM shows interannual-to-decadal variability in the past half century, rather than an obvious decreasing or increasing trend. In addition, the spatial distribution of the EASM is changed (Li et al., 2010; Zhang et al., 2013; Zhang, 2015). The leading mode of the EASM precipitation shifts southward from the "cool epoch" (1958-1980) to the "warm epoch" (1980-2009), leading to an enhanced rainfall over Southeast China and suppressed precipitation over SCS (Li et al., 2010).

In the studies which show the weakening of EASM in recent decades, various EASM indices are used. For instance, Jiang and Wang (2013) used a sea level pressure (SLP) index defined by Guo (1983). Xue (2001) used an index based on the 850-hPa wind defined by Wang (2000). Zhu et al. (2012) applied an index based on the land-sea thermal contrast defined by Zhu et al. (2005). Also the "southern-flood-and-northern-drought" pattern in East Asia is considered as a weakening EASM (Wang, 2001; Zuo et al., 2012). However, as pointed out by Wang et al. (2008), it is not appropriate to regard such pattern as a weak EASM. Moreover, Wang et al. (2008) recommended an EASM index which can reflect the EASM variability. This EASM index recommended by Wang et al. (2008) has a negative correlation with the indices mentioned above. Therefore, if one uses the EASM index defined by Wang et al. (2008) one should see a strengthening EASM during recent decades.

1.2.3 Future Climate

Numerous efforts have been devoted to study how the EASM would change under various global warming scenarios (e.g., Kripalani et al., 2007; Lee and Wang, 2014; Sun and Ding, 2010). Sun and Ding (2010) analyzed 12 models used in the IPCC Special Report on Emission Scenarios (SRES) A1B (a medium emission scenario) and showed that EASM will intensify in a warming climate due to enhanced monsoon circulation, water vapor, and moisture transport into the EASM region. Their explanation is that, as temperature rises, an El Niño-like pattern (increased sea surface temperature over eastern Pacific Ocean) will develop more frequently. This pattern will reduce the SST gradient across the equatorial Pacific Ocean and strengthen the downward airflow over the tropical western Pacific Ocean and WNPSH, and thus enhancing the moisture transport.

In the study by Hu et al. (2003), the EASM changes in a global warming scenario ($2\times CO_2$) was evaluated using 16 models in CMIP2. It reveals that the summer-time mean surface temperature is increased in China, and the precipitation is also enhanced over almost the whole country. In a subsequent study based on the models of CMIP3 and CMIP5, Lee and Wang (2014) also found an intensification of EASM in response to global warming. Their results indicate that the intensified EASM may be attributed to the enhancement and westward displacement of WNPSH. Besides the intensification of the mean state of EASM, its annual cycle would also change in future climate (Kitoh and Uchiyama, 2006; Kripalani et al., 2007; Kusunoki and Arakawa, 2012). Kripalani et al. (2007) analyzed 22 models of IPCC AR4 with doubled atmospheric CO_2 and found that the EASM precipitation shows longer persistence. It lasts from late spring to early fall. Using 15 coupled AOGCM under the SRES A1B scenario at the end of the 21^{st} century, Kitoh and Uchiyama (2006) showed that the rainy season over Japan will be delayed. This result is consistent with Kusunoki and Arakawa (2012) in which they used MRI-AGCM3.1S with 20-km and 60-km resolution.

1.2.4 Mechanisms related to EASM Changes

Previous model simulations generally attribute the variation of EASM in the global warming scenarios to the enhanced and westward displaced WNPSH as well as the strengthening of the moisture transport. The existing relationship between the EASM and WNPSH (e.g., Huang and Sun, 1992; Lu, 2001; Lu and Dong, 2001; Mao et al., 2010; Sun and Ying, 1999; Yang and Sun, 2003; Zhang et al., 2009; Zhang and Tao, 1999; Zhou et al., 2009) implies that the mechanisms explaining the changes in WNPSH in a warmer climate are essential to understand the variations in EASM.

Li et al. (2012) proposed that the intensification of WNPSH in response to higher greenhouse gas concentrations is primarily caused by the increase in the land-sea thermal contrast. In a warmer climate, the enhanced diabatic heating (cooling) over land (ocean) induces an anticyclonic anomaly over the ocean, leading to the strengthening of WNPSH.

Zhou et al. (2009) found that the westward extension of WNPSH is related to the Indian Ocean-western Pacific (IWP) warming induced by the global warming. They designed a numerical experiment in which an SST anomaly is added to SST climatology over IWP region. The warmer SST over IWP increases precipitation locally and intensifies convective heating. The positive SST anomalies over IWP affect the Walker Circulation and result in a deficient precipitation over central and eastern tropical Pacific Ocean, leading to a negative heating anomaly there. The negative heating anomaly induces a Gill-like response (Gill, 1980), generating an anticyclonic anomaly in the WNP. In addition, the low-level equatorial flank of WNPSH can be partly interpreted as Kelvin wave response to the condensation heating of South Asian monsoon (Zhou et al., 2009). The warming-up of the IWP induces easterly anomalies to the east of the heat source, which intensifies the easterlies on the equatorial flank of the WNPSH. This mechanism, proposed by Rodwell and Hoskins (1996), plays a secondary role in the westward extension of the WNPSH. However, the increased SST over IWP reduces the land-sea thermal contrast. As pointed out by Li et al. (2012) the weaker land-sea thermal contrast is not favorable for the intensification of WNPSH.

Moreover, the air-sea interaction also plays an important role in the WNPSH variability

(Wang et al., 2013; Xiang et al., 2013). To the southeast of the WNPSH anomaly, the anomalous northeasterlies strengthen the mean easterly wind. The increased northeasterlies enhance the evaporation/entrainment and reduce the SST. The cooling SST generates the anticyclonic vorticity to its north (Gill-type) and further enhances the WNPSH anomaly. Also to the southwest of WNPSH, the easterly anomaly weakens the mean southwesterly flow and warms up the IO. The warming-up of IO induces Kelvin waves to its east and favors to sustain WNPSH. These theories have been confirmed by numerical experiments (Wang et al., 2013), in which the SST is reduced over central Pacific Ocean by adding an initial SST perturbation to a coupled model. The results indicate that the WNPSH variation is "primarily controlled by central Pacific cooling/warming and a positive atmosphere-ocean feedback between the WNPSH and the Indo-Pacific warm pool oceans" (Wang et al., 2013). In their model experiment the SST is decreased directly over the area where there is positive GPH anomaly.

1.3 Objectives of this Study

The understanding of physical mechanisms underlying the formation and maintenance of the EASM system is limited by the ability of current generation of climate models to simulate the observed features associated with EASM. The representation of convective processes in the model is one of the causes identified as a large source of errors in the simulation of intraseasonal variability of the tropical atmosphere. In the conventional parameterization of cloud processes, the intraseasonal variability tends to be damped by the various assumptions used by the parameterization schemes. The multi-scale modeling framework (MMF) (Grabowski, 2001; Khairoutdinov and Randall, 2001) or super-parameterization (Grabowski, 2002) of cloud processes, which is a bridge between the conventional parameterization methods and the global cloud-resolving models, has shown significant improvements in the simulation of many of the components of the global monsoon systems (DeMott et al., 2011; McCrary et al., 2014). A climate model based on the super-parameterization of cloud processes is used in this study to explore the response of EASM and its variability to climate change, and to validate a new mechanism explaining the EASM variability induced by the global warming. The new mechanism emphasizes the role of remote air-sea interactions in modulating the position WNPSH via the convective activity of the tropics.

The ability of the super-parameterized model to simulate the observed features of EASM is not known. To demonstrate the adequacy of this model for the objectives of this study, the EASM simulation of this model is first evaluated. The aims of the evaluation are twofold: i) to identify the model skill in capturing the mean state, annual cycle, and intraseasonal variability of EASM, and ii) to quantify the advantages of using super-parameterization versus the conventional parameterization.

In addition, the response of the EASM to the global warming scenario is analyzed using the super-parameterized model. It aims to explain how and why the EASM would change in a warmer climate. As discussed in Section 1.2.4, the EASM changes in a future warmer climate are closely related to the variations in WNPSH, which is attributed to the changes in the mean state of the boundary conditions (Wang et al., 2013; Xiang et al., 2013; Zhou et al., 2009). However, neither of these two mechanisms looked at the influence of the remote air-sea interaction. Zhou et al. (2009) proposed that the warmer SST over IWP lowers the SST over tropical eastern Pacific Ocean via Walker Circulation, and further intensifies the WNPSH through a Gill-type response to this decreased SST. However they did not change the SST over tropical eastern Pacific Ocean. In addition, in the studies by Wang et al. (2013) and Xiang et al. (2013) the SST is changed directly over the region where there are GPH anomalies, which will have a large impact on the WNPSH through the local air-sea interaction. Therefore, in this study a new mechanism is proposed to explain the WNPSH changes in a warmer climate. This mechanism focuses on the impact of the remote air-sea interaction on the changes of the WNPSH.

To sum up, the objectives of this study include the following aspects:

- Evaluate the performance of SP-CCSM4 in simulating the EASM under present climate.

- Study the intraseasonal variability of the EASM.
- Analyze the EASM changes under global warming scenario using SP-CCSM4.
- Study the mechanisms related to the future changes of the EASM.

The rest of the dissertation is organized as follows: Chapter 2 describes the models used in this study, the validation dataset, and the methods applied to do the analysis. Chapter 3 discusses the EASM simulation in SP-CCSM4, including its comparison with observations and CCSM4 in seasonal mean state, annual cycle, and intraseasonal variability. In Chapter 4 the EASM simulations under various warming scenarios are analyzed, plus a remote air-sea interaction mechanism is proposed to explain the changes of the EASM. Chapter 5 shows how the proposed mechanism is tested. Conclusions and discussions are in Chapter 6.

Chapter 2: Model, Data, and Methods

2.1 Model Description

The model used in this study is the Super-Parameterized Community Climate System Model version 4 (SP-CCSM4), which uses an explicit 2D cloud resolving model (CRM) embedded in each GCM grid column. The CRMs are aligned in the east-west direction, have a horizontal resolution of 4 km and 30 levels in the vertical. The simulation was carried out at the horizontal resolution for the host atmospheric model of 2.5° (longitude) ×1.9° (latitude) using a finite volume representation of the dynamical core. The resolution of the ocean model is 1° × 1° in the horizontal. The sea-ice model uses the same resolution as the ocean model, and the horizontal resolution in the land model is the same as in the atmosphere model. A complete description of the model is given by Stan and Xu (2014). The simulation is initialized in January 2006, spans 150 years, and is driven by a constant external forcing. In Chapter 3, the data between 2071-2100 were used for evaluating the simulation of the EASM. In Chapter 4, the data between 2125-2154 were used to analyze the EASM changes under various global warming scenarios.

To assess the performance of the SP-CCSM4, the EASM simulation by SP-CCSM4 is compared with that by CCSM4. In CCSM4, the cloud process is represented by the conventional convection parameterization (Neale et al., 2013), while SP-CCSM4 uses a 2D CRM embedded in each GCM grid column as described above. The CCSM4 used the same initial condition and external forcing as that in SP-CCSM4. Therefore, the only difference between SP-CCSM4 and CCSM4 is the representation of cloud-scale processes (Stan and Xu, 2014).

2.2 Data

The observational data used in this study consist of:

1. Monthly and pentad precipitation from the Global Precipitation Climatology Project (GPCP) (Huffman et al., 1997). The precipitation data cover the period between 1983 and 2012, with $2.5^\circ \times 2.5^\circ$ spatial resolution.

2. Monthly and daily 2D and 3D atmospheric variables from the National Centers for Environmental Prediction (NCEP) reanalysis (Kalnay et al., 1996). The horizontal resolution of the 3D data is $2.5^\circ \times 2.5^\circ$, and vertically, there are 17 levels. The 2D data set has approximately $1.9^\circ \times 1.9^\circ$ spatial resolution.

3. The European Center for Medium-range Weather Forecasts Reanalysis-Interim (ERA-Interim) (Dee et al., 2011). Both 3D and 2D data have approximately $0.703^\circ \times 0.703^\circ$ spatial resolution, and vertically, there are 37 levels for 3D data. The 3D atmospheric variables include geopotential height (GPH), wind, specific humidity and temperature, while the 2D fields contain surface temperature, sensible heat flux and latent heat flux. The ERA-Interim monthly data are for 1983-2012, while the daily data are from 1979-2006.

4. Daily mean Outgoing Longwave Radiation (OLR) data from National Oceanic and Atmospheric Administration (NOAA) (Liebmann and Smith, 1996). The grid spacing of OLR is $2.5^\circ \times 2.5^\circ$ (longitude $\times$ latitude) and the time period spans from 1979 to 2006.

5. Daily SST data from NOAA Optimum Interpolation (OI) daily 0.25-degree SST (Reynolds et al., 2002) from 1982 to 2006.

All data sets used in the analyses, including the model output, are interpolated from their original grid to the $2.5^\circ \times 2.5^\circ$ horizontal resolution.

2.3 Methods

2.3.1 Climatology and Annual Cycle

The May-June-July-August (MJJA) climatological means were computed for observations, SP-CCSM4, and CCSM4 using monthly data. The annual cycle of the EASM was evaluated by constructing pentad means from daily averages and taking the zonal mean between 110°E-120°E (East China) and 120°E-140°E (WNP, Japan, and Korean Peninsula).

2.3.2 Diabatic Heating

The MJJA mean vertically integrated diabatic heating is calculated by using daily wind and temperature data. It is firstly computed for each month, and then averaged for MJJA. The diabatic heating is diagnosed as a residual in the thermodynamic equation, and is based on the method by Nigam (1997) and Nigam et al. (2000). The equation below is the one given by Nigam et al. (2000).

$$\dot{Q} = \overline{\frac{\Delta T}{\Delta t}} + \overline{v} \cdot \nabla \overline{T} + (p/p_0)^{(R/c_p)} \overline{\omega} \frac{\partial \overline{\theta}}{\partial p} + (p/p_0)^{(R/c_p)} \left[\nabla \cdot \overline{v'\theta'} + \frac{\partial \overline{\omega'\theta'}}{\partial p} \right], \tag{2.1}$$

where

$\dot{Q}$ = daily diabatic heating rate

T = temperature

v = horizontal wind

p = pressure

p_0 = standard reference pressure, 1000 hPa

R = universal gas constant of dry air, 287J K^{-1} kg^{-1}

c_p = specific heat capacity at a constant pressure, 1004J $K^{-1}kg^{-1}$

ω = pressure vertical velocity

θ = potential temperature

The overbar term denotes the monthly average, and the prime term denotes the departure of the daily data from the monthly mean. The first term on the right hand side of the equation means the change of daily temperature between two consecutive days. The second term is the horizontal advection of the temperature. The third term means the vertical advection of the temperature. The fourth term in the bracket is the transient component, which represents "both synoptic and low-frequency (but submonthly) fluctuations" (Chan and Nigam, 2009). It denotes the horizontal and vertical heat transport.

2.3.3 850hPa GPH index

The position of the WNPSH can be described by the index of WNPSH (Zhang and Tao, 1999). The index is computed using the pentad mean zonal wind at 850hPa. Firstly, for each longitude within a domain (115°E-140°E, 15°N-45°N), find the latitude where the zonal wind changes from easterlies to westerlies. Then do a linear interpolation based on the magnitude of the zonal wind at this latitude to find the latitude where the zonal wind equals zero (y_0) for each longitude. Afterwards calculate the mean of y_0. This index indicates the meridional movement of the WNPSH.

2.3.4 Trajectory of WNPSH

The trajectory of the WNPSH is denoted by the intersection of subtropical ridge and the 1540m isoline. It illustrates the movement of the WNPSH in both zonal and meridional directions. It is calculated based on pentad mean GPH and zonal wind at 850hPa. Firstly, find the the latitude (y_0) where the zonal wind changes from easterlies to westerlies for each longitude over (100°E-170°E, 5°N-40°N). Then, find the intersections of the curve defined by y_0 with the 1540-m isoline. The intersection point is also based on linear interpolation.

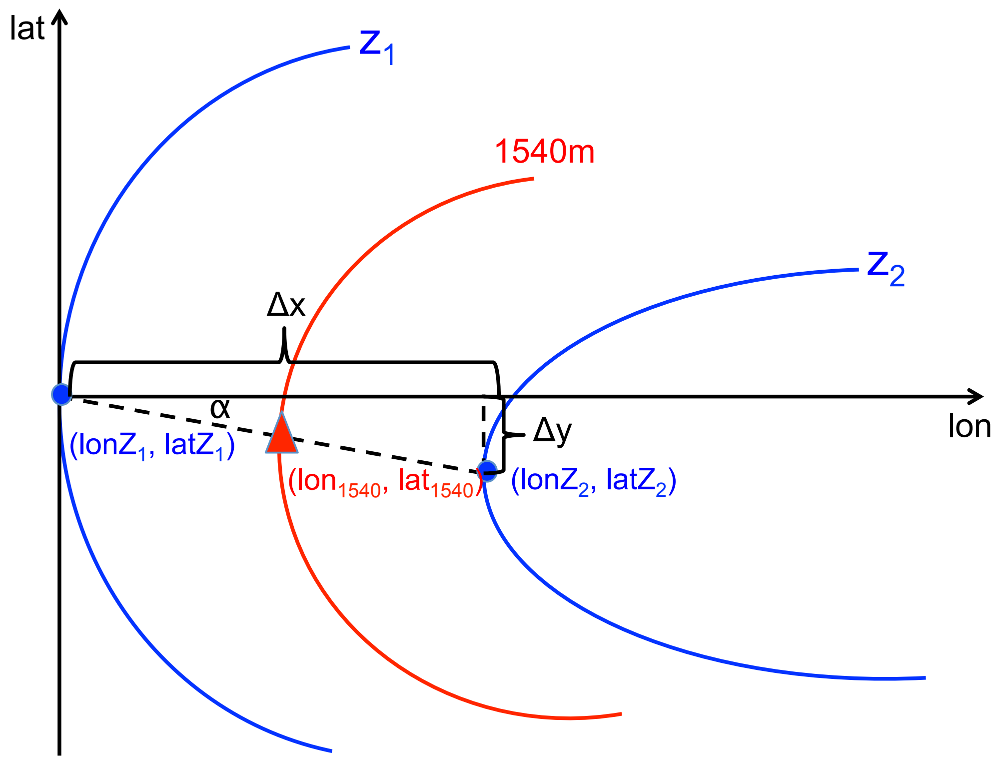

Figure 2.1: A sketch for the calculation of the WNPSH trajectory.

The steps of calculation are as follows, and a sketch is shown in Fig. 2.1.

$$\Delta x = 2.5 \quad \Delta y = y_{x+1} - y_x \tag{2.2}$$

$$cos\alpha = \frac{\Delta x}{\sqrt{\Delta x^2 + \Delta y^2}} \quad sin\alpha = \frac{\Delta y}{\sqrt{\Delta x^2 + \Delta y^2}} \tag{2.3}$$

$$Lon_{1540} = lon(z_1) + \frac{\sqrt{\Delta x^2 + \Delta y^2}}{z_2 - z_1} \cdot (1540 - z_1) \cdot cos\alpha \tag{2.4}$$

$$Lat_{1540} = lat(z_2) + \frac{\sqrt{\Delta x^2 + \Delta y^2}}{z_2 - z_1} \cdot (1540 - z_1) \cdot sin\alpha \tag{2.5}$$

2.3.5 Composite Analysis

The evolution of the intraseasonal variability of EASM was evaluated in the composite analysis (Hsu and Weng, 2001; Tsou et al., 2005) of 30-60-day (10-20-day) bandfiltered daily anomalies. The daily anomalies were computed by removing the mean annual cycle (mean plus the first three harmonics) from the daily data. Since the northward propagation of EASM occurs mostly during May through July, the composite analysis is based on May, June, and July (MJJ). The composite analysis of the EASM life cycle follows the method of Kemball-Cook and Wang (2001). The life cycle of an event was defined based on an OLR index. This OLR index was constructed by taking the area average (defined later) of the 30-60-day bandfiltered OLR anomaly over SCS where the bandfiltered OLR variance reaches the maximum. Day 0 of the cycle is centered on the day when the OLR index during MJJ is less than a certain threshold (e.g., minus one standard deviation) over SCS. The region and threshold are the same for observations and models. The life cycle of an EASM event for 30-60-day (10-20-day) mode consists of 12 phases starting from 15 (10) days before and 40 (12) days after Day 0. The statistical significance of the composite is assessed using the Student's t test.

2.3.6 Multivariate Empirical Orthogonal Function (MV-EOF)

The multivariate Empirical Orthogonal Function analysis (MV-EOF), discussed by Wang et al. (2008), is used to study the variability of the EASM. It extends the conventional EOF by using various variables. It captures dominant patterns in the spatial phase relationships among various fields (Wang, 1992). In this study the MV-EOF is applied on a set of three variables: MJJA mean precipitation, zonal and meridional wind component at 850 hPa. To emphasize the hybrid tropical-subtropical feature of the EASM, the domain of MV-EOF is (105°E-140°E, 10°N-50°N), which includes both tropical and subtropical East Asia area. All the three variables (precipitation, 850-hPa zonal wind, and 850-hPa meridional wind) have been normalized before doing the MV-EOF. The covariance matrix is constructed by combing the three normalized variables. The spatial phase relationships among low-level circulation and precipitation can be captured by using MV-EOF method (Wang et al., 2008).

2.3.7 Canonical Correlation Analysis (CCA)

Canonical correlation analysis (CCA) is a method for measuring the linear relationships between two multi-dimensional sets of variables (vectors). It calculates the maximum correlation between two linear combinations of variables, thus identifying the maximized interrelationship between two data sets. In practice, the CCA is applied to a truncated set of principal components (PCs) (Barnett and Preisendorfer, 1987). The details of the CCA method will be fully described in Chapter 5.

Chapter 3: EASM simulation in SP-CCSM4 Under Present Climate Condition

This chapter is focused on evaluating the ability of a model with explicit representation of cloud processes, SP-CCSM4, to simulate the EASM. Previous studies using the super-parameterization method (Grabowski, 2001; Khairoutdinov and Randall, 2001) showed that the multi-scale representation of cloud properties improves the simulation of ISM and the northward propagation of Boreal Summer Intraseasonal Oscillation (BSISO) (DeMott et al., 2013; Krishnamurthy et al., 2014). However, the performance of SP-CCSM4 in simulating the EASM is unknown. In this chapter, the EASM simulated by SP-CCSM4 and the conventionally-parameterized CCSM4 are evaluated against observations, including the mean state, the annual cycle, and the ISO. The mechanisms related to the northward propagation of the EASM are also investigated in order to understand which mechanism is deficient in SP-CCSM4. In addition, the patterns of the northward propagation of the ISO is further analyzed based on the different thermal conditions of the West Pacific Warm Pool (WPWP).

This chapter is the basis of Jin and Stan (2016), which was published online in Journal of Geophysical Research-Atmospheres.

3.1 Model Biases

The SP-CCSM4 and CCSM4 models' ability to simulate the observed patterns of the climatological means is measured by the difference between each model and observation, referred to as biases, and by the centered pattern correlation (spatial mean removed). This section evaluates the model biases in simulating the seasonal mean state, annual cycle, and ISV.

The mean state includes precipitation, the large-scale monsoon airflows, meridional circulation, surface temperature, and surface heat fluxes. Because EASM is characterized by a northward propagation of the precipitation, the annual cycle of the zonal mean precipitation and WNPSH index is compared between SP-CCSM4 and observation. Both the NCEP and ERA-Interim reanalysis data are used as observation for the comparison, and they produce similar results. For this reason, only the comparison between the models and ERA-Interim is shown.

3.1.1 Seasonal Mean of EASM

Table 3.1 lists the pattern correlation coefficients between each of the two models and observations for MJJA mean of different variables. Sperber et al. (2013) used the pattern correlation to evaluate the CMIP3 and CMIP5 model skill in simulating the mean state of EASM. Generally SP-CCSM4 has higher correlation than CCSM4, and the largest difference between the two models occurs in the field of precipitation, 850-hPa wind, meridional circulation, and vertically integrated moisture transport.

Figure 3.1 shows the MJJA mean precipitation in observation and model biases, defined as the difference between the values simulated by the model and the observed values. Both models underestimate the magnitude of precipitation over Southeast China, Korean Peninsula, and the region south of Japan, indicating a weak subtropical monsoon trough in the models. The precipitation deficiency in CCSM4 is more intense and extends to SCS (Fig. 3.1c). The SP-CCSM4 simulates excessive precipitation over WNP (Fig. 3.1b), indicating a northward displacement of the tropical monsoon trough (figure not shown). In CCSM4, the region with excessive precipitation is located over central China (figure not shown). The pattern correlation of MJJA mean precipitation is higher in SP-CCSM4 than in CCSM4 (Table 3.1), which means that the spatial distribution of mean precipitation is better simulated in SP-CCSM4. The area average of the model bias is smaller in SP-CCSM4, and the visual inspection of Fig. 3.1b and Fig. 3.1c may suggest that, in SP-CCSM4, the smaller value results from the cancelation of errors between the northern

Table 3.1: Pattern correlation coefficients of MJJA mean state between models and observations.

Variable		SP-CCSM4	CCSM4
Precipitation		**0.629**	0.238
850-hPa GPH		0.824	**0.839**
850-hPa wind	magnitude	**0.654**	0.338
	u-component	**0.638**	0.618
	v-component	**0.583**	0.402
200-hPa wind	magnitude	0.895	**0.933**
	u-component	0.943	**0.960**
	v-component	**0.689**	0.308
Meridional circulation	v-component	**0.933**	0.879
	ω-component	**0.859**	0.213
Vertically integrate moisture transport	magnitude	0.516	**0.617**
	u-component	**0.729**	0.370
	v-component	**0.720**	0.626
Latent heat flux		**0.909**	0.771
Sensible heat flux		**0.969**	0.792

The domain of each field is consistent with the spatial pattern of the mean state in Fig. 3.1 to Fig. 3.6. The domain is (110°E-150°E, 10°N-50°N) for precipitation, 850-hPa and 200hPa wind fields, vertically integrated moisture transport, surface temperature, latent and sensible heat fluxes. The domain is (105°E-180°E, 10°N-50°N) for 850-hPa geopotential height (GPH), and (110°E-120°E, 10°N-50°N, 1000 –100-hPa) for meridional circulation. The model with the higher spatial pattern correlation coefficient is in bold.

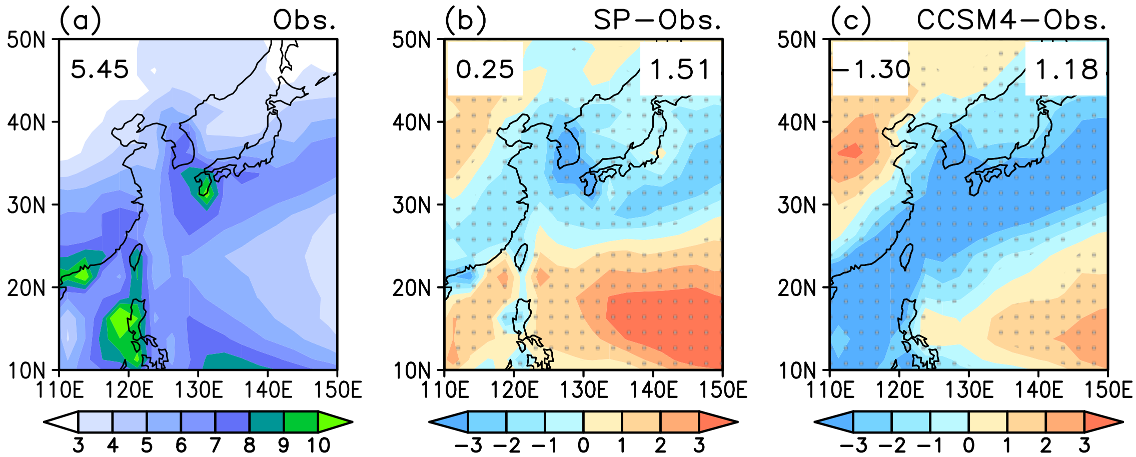

Figure 3.1: MJJA mean precipitation rate (unit: mm/day). (a) Observation, (b) the difference between SP-CCSM4 and observation, and (c) the difference between CCSM4 and observation. The grey dots in (b) and (c) denote the regions exceeding 95% significance level. The value at the top-left corner denotes the domain-averaged mean precipitation in observation (a) and the domain-averaged precipitation difference between model and observation (b and c). The value at the top-right corner of (b and c) denotes the domain-averaged root mean square of precipitation difference between model and observation.

and southern parts of the domain. The mean value of the precipitation bias for the region between 20°N-50°N in SP-CCSM4 is −0.45 mm/day and −1.61 mm/day in CCSM4. The evaluation of the two models with respect to the root mean square error (RMSE) reveals that SP-CCSM4 (1.30 mm/day) has a larger value than CCSM4 (0.88 mm/day). Since, by definition, RMSEs weigh more the errors with larger absolute values than the errors with smaller absolute values (e.g., Chai and Draxler, 2014; Willmott and Matsuura, 2005), one can speculate that RMSE in SP-CCSM4 is dominated by the outliers. The outlier may be related to one of the limitations of the multi-scale framework, namely the periodicity of the CRM domain. In some instances, the domain configuration may artificially amplify strong events.

Following Lu et al. (2008), the GPH at 850 hPa is adopted to describe the WNPSH characteristics. Figure 3.2a shows the isoline of 1500 m and the ridge line of WNPSH in observation, SP-CCSM4, and CCSM4. The model biases for the 1500-m isoline are shown

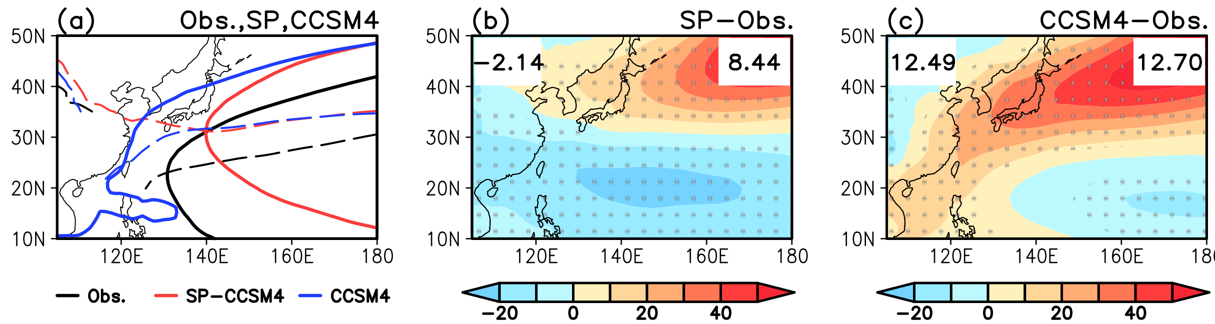

Figure 3.2: The MJJA mean GPH at 850 hPa (unit: m). (a) Observation, SP-CCSM4 and CCSM4, (b) the difference between SP-CCSM4 and observation, and (c) the difference between CCSM4 and observation. In (a) the solid contours are the isolines of 1500 m and dashed lines are the ridge line of the WNPSH for observation (black), SP-CCSM4 (red) and CCSM4 (blue). The grey dots in (b) and (c) denote regions exceeding 95 % significance level. The values at the top-left and top-right corners of (b) and (c) have the same meaning as in Fig. 3.1, except for the 850-hPa GPH.

in Fig. 3.2b and Fig. 3.2c. In observations, the western edge of the 1500-m isoline reaches 130°E, and the ridge line is located between 20°N to 30°N. Compared to the observation, the WNPSH in SP-CCSM4 is displaced northward (Fig. 3.2a) and is weaker (Fig. 3.2b). In SP-CCSM4, the western margin of 1500-m isoline retreats to 140°E; the subtropical ridge stays at approximately 30°N over the Pacific Ocean and tilts northward as it approaches the East Asia continent. This northward shift of WNPSH was also found in AOGCMs (Kusunoki and Arakawa, 2015) and AGCMs (He and Zhou, 2014; Song and Zhou, 2014) of CMIP5. In CCSM4, the WNPSH expands northwestward while the 1500-m isoline extends to the west of 120°E. The lower domain-averaged difference of 1500-m indicates that the WNPSH is better simulated in SP-CCSM4 than in CCSM4.

Figure 3.3 depicts the MJJA mean meridional circulation averaged between 110°E and 120°E in observation, SP-CCSM4, and CCSM4. Both models reproduce the observed centers of maximum ascending motion: one center is located between 10°N-20°N, and the other one to its north. However there are noticeable biases in both models. In SP-CCSM4, the rising motion between 25°N and 35°N is weaker than in observations, which is consistent

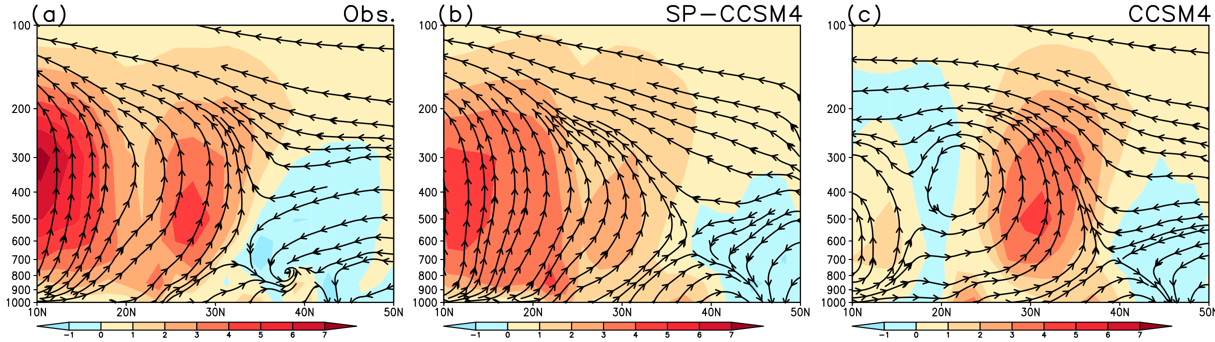

Figure 3.3: The MJJA mean streamlines of meridional and vertical velocity averaged between 110°E-120°E. (a) observation, (b) SP-CCSM4, (c) CCSM4. The shadings represent the magnitude of the vertical velocity (×-0.01 Pa s^{-1}). The yellow-red color represents the ascending motion and the blue color denotes the descending motion.

with the precipitation deficiency over the eastern coast of China (Fig. 3.1b). In CCSM4, the magnitude of the ascending branch to the south of 20°N is underestimated, plus the upward motion at around 30°N is displaced northward compared to observations. The bias in the ascending branch is related to the intensified precipitation over central China in CCSM4 (Fig. 3.1c).

In observations, the horizontal distribution of the low-level circulation consists of a southwesterly flow over the southern SCS, East Asia, and WNP, and a southeasterly flow over the subtropical west Pacific Ocean (WP) (Fig. 3.4a). In SP-CCSM4, the westerly flow is overestimated over SCS and the zonal wind is reduced over the region from 20°N to 40°N. The CCSM4 is characterized by stronger easterly wind over WNP as well as intensified southwesterlies over eastern China to Korean Peninsula. The lower-level wind pattern is consistent with the position and spatial distribution of WNPSH (Fig. 3.2a). At upper levels, the South Asian High (SAH) is the most prominent feature over the African-Asian region in boreal summer. Over the EASM region, the westerly jet to the northern side of SAH is underestimated in both models (Fig. 3.4e-f). The domain-averaged wind difference at lower and upper levels are comparable in the two models (Fig. 3.4b-c, Fig. 3.4e-f). The domain-averaged wind difference at lower and upper levels is comparable in the two models

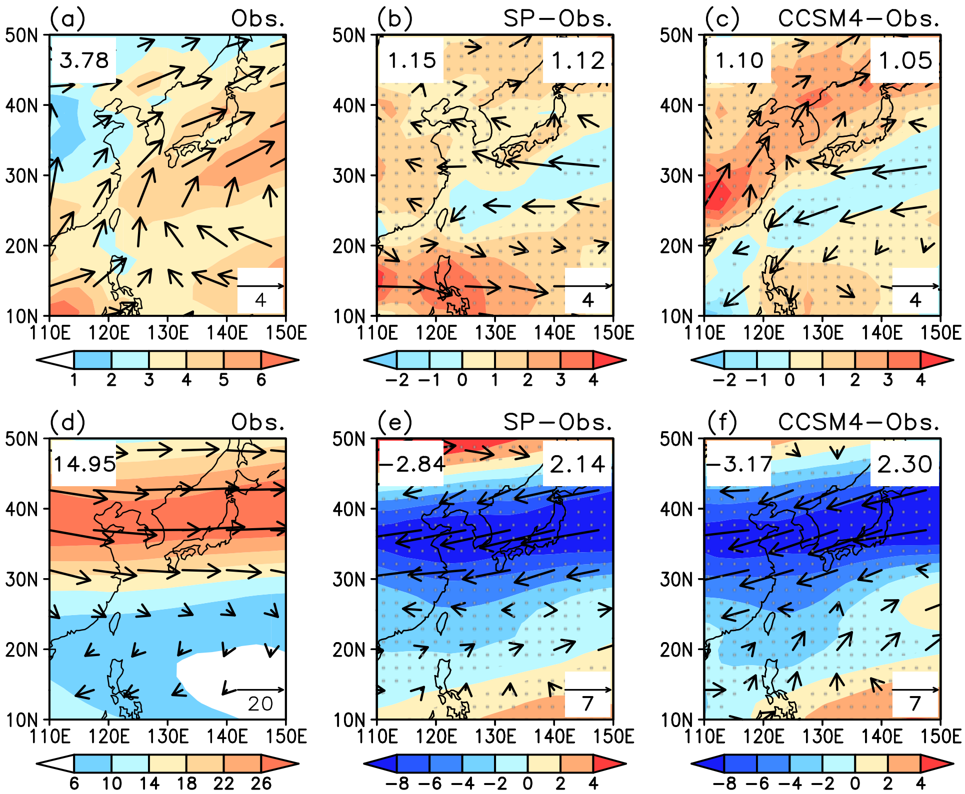

Figure 3.4: MJJA mean wind at 850 hPa (a-c) and 200 hPa (d-f) (unit: ms^{-1}). The shading denotes wind magnitudes and vectors are wind directions. (a) and (d): Observation, (b) and (e): the difference between SP-CCSM4 and observation, (c) and (f): the difference between CCSM4 and observation. The grey dots in (b), (c), (e), and (f) denote the regions where the wind magnitude exceeds 95% significance level. The value at the top-left corner denotes the domain-averaged wind magnitudes in observation (a and d) and the domain-averaged wind difference between model and observation (b, c, e, and f). The value at the top-right corner of (b), (c), (e), and (f) denotes the domain-averaged root mean square of wind difference between model and observation.

(Fig. 3.4b-c, Fig. 3.4e-f), whereas the spatial pattern correlation coefficients are generally higher in SP-CCSM4 (Table. 3.1).

Simulation of the thermodynamic surface fluxes is shown in Fig. 3.5a-c for the sensible heat flux and Fig. 3.5d-f for the latent heat flux. In both models, the sensible heat flux is overestimated approximately between 20°N and 32°N and underestimated to the north of this region. However, CCSM4 simulates a weaker sensible heat flux (Fig. 3.5b and Fig. 3.5c). Aside from the sensible heat flux, the latent heat flux over the central and eastern China

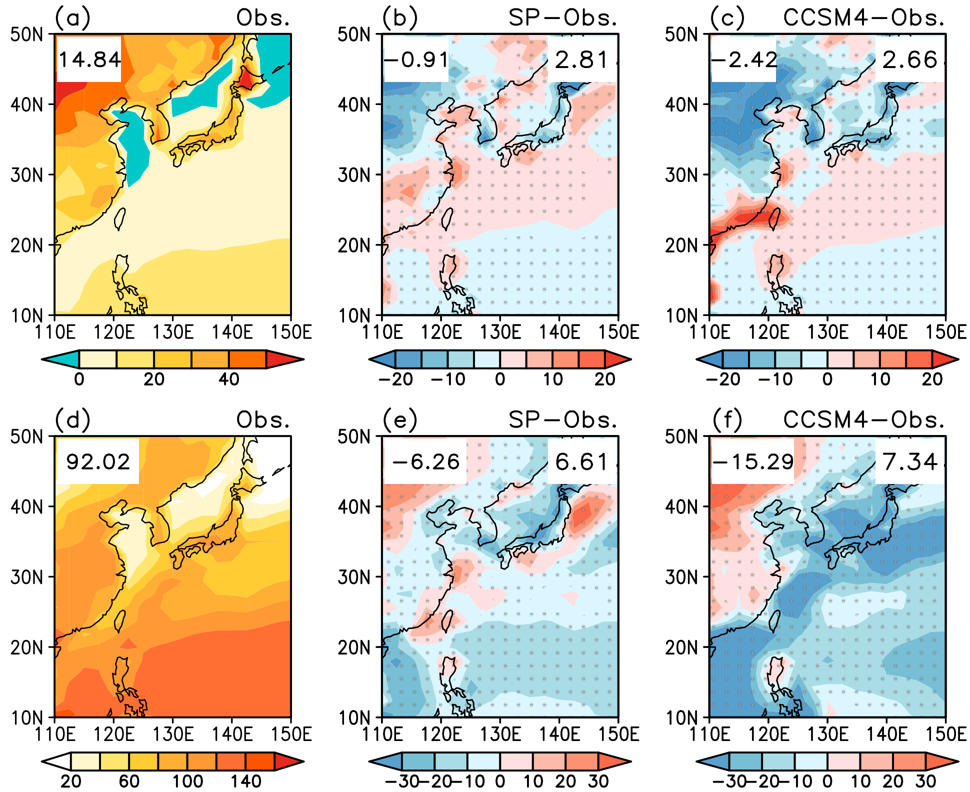

Figure 3.5: MJJA mean sensible heat flux (a-c) and latent heat flux (d-f) (unit: W m^{-2}). (a) and (d): Observation, (b) and (e): the difference between SP-CCSM4 and observation, (c) and (f): the difference between CCSM4 and observation. The grey dots in (b), (c), (e), and (f) denote the regions exceeding 95% significance level. The value at the top-left corner denotes the domain-averaged heat flux in observation (a and d) and the domain-averaged heat flux difference between model and observation (b, c, e, and f). The value at the top-right corner of (b), (c), (e), and (f) denotes the domain-averaged root mean square of heat flux difference between model and observation.

is underestimated in SP-CCSM4 (Fig. 3.5) while it is overestimated in CCSM4 (Fig. 3.5f). Therefore, over eastern China, CCSM4 simulates moist conditions and SP-CCSM4 simulates dry conditions.

The moisture transport into the monsoon region is known to influence the precipitation. In observations, the moisture transport from SCS splits into a branch that turns northward, merging with the moisture transport from WNP (Fig. 3.6a). As mentioned above, the moisture transport is associated with the spatial distribution of WNPSH. In SP-CCSM4,

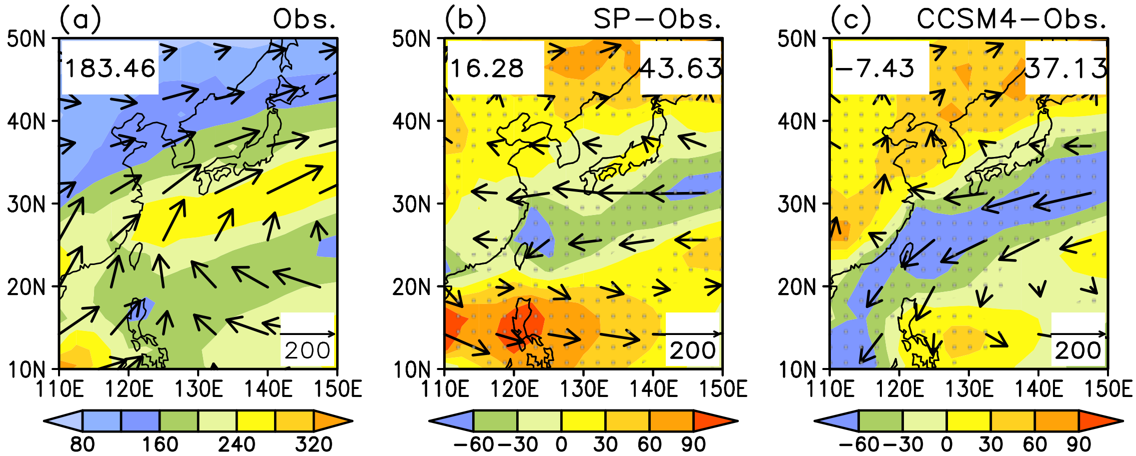

Figure 3.6: MJJA mean vertically integrated moisture transport (unit: Kg $m^{-1}s^{-1}$). The shading denotes magnitudes of moisture transport and vectors are directions. (a) Observation, (b) the difference between SP-CCSM4 and observation, and (c) the difference between CCSM4 and observation. The grey dots in (b) and (c) denote the regions here the magnitude of moisture transport exceeds 95% significance level. The value at the top-left corner denotes the domain-averaged magnitude of moisture transport in observation (a) and the domain-averaged difference of moisture transport between model and observation (b and c). The value at the top-right corner of (b) and (c) denotes the domain-averaged root mean square of moisture transport difference between model and observation.

the WNPSH is displaced northeastward (red contour in Fig. 3.2a), thus the northeastward flowing moisture transport becomes weaker (Fig. 3.6b). While in CCSM4 (blue contour in Fig. 3.2a), the WNPSH extends westward as well as northward, which induces larger amount of moisture to the western and northern sides of the EASM area (Fig. 3.6c). Therefore, the precipitation is reduced over Southeast China, Korean peninsula, and southern Japan (Fig. 3.1c).

The above analysis indicates that SP-CCSM4 has better skill in simulating the MJJA mean state of EASM due to higher spatial correlation coefficients in most of the variables analyzed. The SP-CCSM4 has higher correlation coefficients than CCSM4 for 11 out of the 15 variables (Table 3.1). The analysis also reveals that both models have shortcomings in simulating the observed features of EASM. The models' biases in simulating the precipitation field are largely due to the position and magnitude of the WNPSH, which influence the low level wind and moisture transport.

3.1.2 Annual Cycle of EASM

The annual cycle of EASM of each model is compared to observations. The time series at each grid point is constructed using climatological pentad mean data. Figure 3.7 shows the annual cycle of the zonal mean precipitation averaged between 110°E and 120°E. In observations, after the first ten days of May, the equatorial rain belt propagates northward rapidly and merges with the rain belt over South China, leading to an increase of precipitation there. This rainy episode corresponds to the first standing stage of the EASM seasonal march. Before mid-May, the rain band located between 20°N-28°N is called pre-summer rainy season in South China (Ding and Chan, 2005). Around 10 June, the rain belt shifts northward and stays between 28°N-32°N until early July. This rainy episode represents the Mei-yu season and is also referred to as the second standing stage of the EASM seasonal march. Afterwards, it advances northward again reaching to North China (Fig. 3.7a). The seasonal march of the EASM rainfall described here has also been documented by Ding et al. (2005) and Ding and Chan (2005).

Compared to the observations, SP-CCSM4 also simulates the sudden northward jump of the tropical rain belt and its mergence with the South China rain belt, as well as the stepwise march of the precipitation (Figure not shown). However, one can notice some differences between SP-CCSM4 and observations (Fig. 3.7b). In SP-CCSM4, the pre-summer rainy season over South China moves northward and the emergence of the two rain belts in mid-May is not as fast as in the observations (Figure not shown). The subtropical branch is less intense than in the observations while the tropical rain band is overestimated (Fig. 3.7b). The Mei-yu season commences earlier (approximately 1 June) and spans a shorter time period in SP-CCSM4, because it lasts only until around 20 June. Also, for the last rainy period, the rain belt starts to shift in late June and reaches a higher latitude than in observations. The bias in time and location leads to the rain deficiency over the EASM region in the model (Fig. 3.7b). This deficiency in the seasonal march of Mei-yu is also

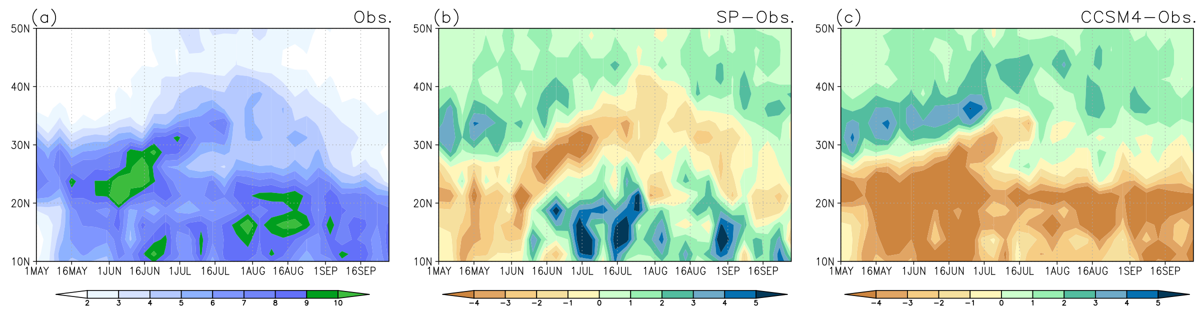

Figure 3.7: Latitude-time cross-section of pentad mean precipitation rate averaged between 110°E and 120°E (unit: mm day^{-1}). (a) Observation, (b) difference between SP-CCSM4 and observation, and (c) difference between CCSM4 and observation.

common to CMIP5 AOGCMs (Kusunoki and Arakawa, 2015).

In CCSM4, the tropical rain band is largely underestimated throughout the whole summer (Fig. 3.7c). The large decrease of precipitation between 10°N and 25°N in early summer implies that the merger of tropical and subtropical rain band at mid-May is missing, and thus the monsoon onset is not simulated properly in CCSM4. In addition, the whole subtropical rain band is displaced northward (Fig. 3.7c).

The annual cycles of the wind and vorticity at 850 hPa are also characterized by the northward propagation (Fig. 3.8a-c), consistent with the precipitation belt movement seen in Fig. 3.7. In observations (Fig. 3.8a), the prevailing winds between 10°N and 20°N turn from southeasterlies to southwesterlies in mid-May, indicating the onset of the SCS monsoon. One branch of the southwesterly flow shifts in steps toward the north over East Asia while another branch remains in the subtropical region. The northward propagation is also reflected in the migration of the low-level cyclonic vorticity.

SP-CCSM4 simulates the wind reversal over 10°N-20°N in mid-May, as well as the southern branch of the southwesterly flow in the subtropics. Compared to the observations, in SP-CCSM4, the southwesterly flow and cyclonic vorticity over subtropics move northward (Fig. 3.8b), consistent with the northward shift in the position of WNPSH. However, the southwesterly flow and the cyclonic vorticity are weaker over the EASM region starting

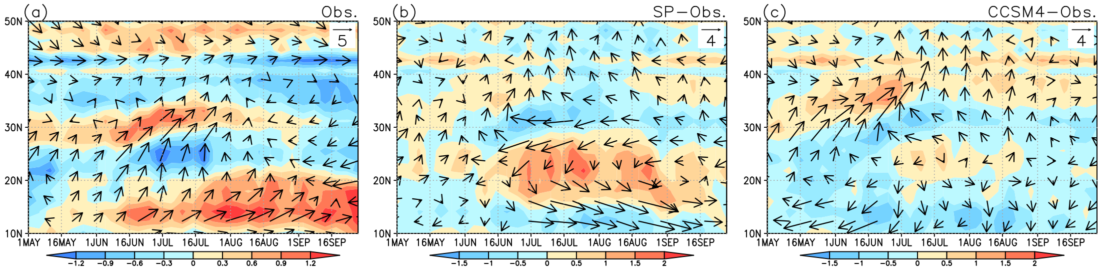

Figure 3.8: Latitude-time cross-section of pentad mean 850-hPa vorticity (shading, unit: $10^{-5}s^{-1}$) and 850-hPa wind (vectors, unit: ms^{-1}) between 110°E and 120°E (unit: mm day^{-1}). (a) Observations, (b) difference between SP-CCSM4 and observations, and (c) difference between CCSM4 and observations.

from mid-June. This feature is consistent with the deficient rainfall and shorter period of the Mei-yu season in SP-CCSM4 (Fig. 3.7b).

In CCSM4, the easterly anomalies persist over 10°N-20°N from May to June (Fig. 3.8c), which means that easterlies do not switch to westerlies there. This persistence indicates a delayed onset of SCS monsoon in CCSM4. In addition, in CCSM4, the northward propagation of cyclonic vorticity over the EASM domain is displaced northward compared to observations, which is associated with the northward displaced subtropical rain band (Fig. 3.7c).

The difference in the annual cycle of precipitation between the models and observation can be partly explained by the migration of WNPSH, because the propagation of the rain belt is related to the meridional displacement of the WNPSH ridge line. The position of the WNPSH can be described by the index of WNPSH of Zhang and Tao (1999) applied to the GPH at 850 hPa (description in Section 2.3.3). The annual cycle of the WNPSH index is shown in Fig. 3.9 for observation, SP-CCSM4 and CCSM4. In observations, the WNPSH starts shifting northward from mid-May, and reaches the northernmost position in August. In SP-CCSM4, the WNPSH starts to jump northward in early June, and reaches 40°N around mid-August, which is far more northward compared to observations. In CCSM4, the WNPSH moves northward gradually from May to early June, and also reaches the northernmost position in August. The WNPSH in CCSM4 is also displaced northward

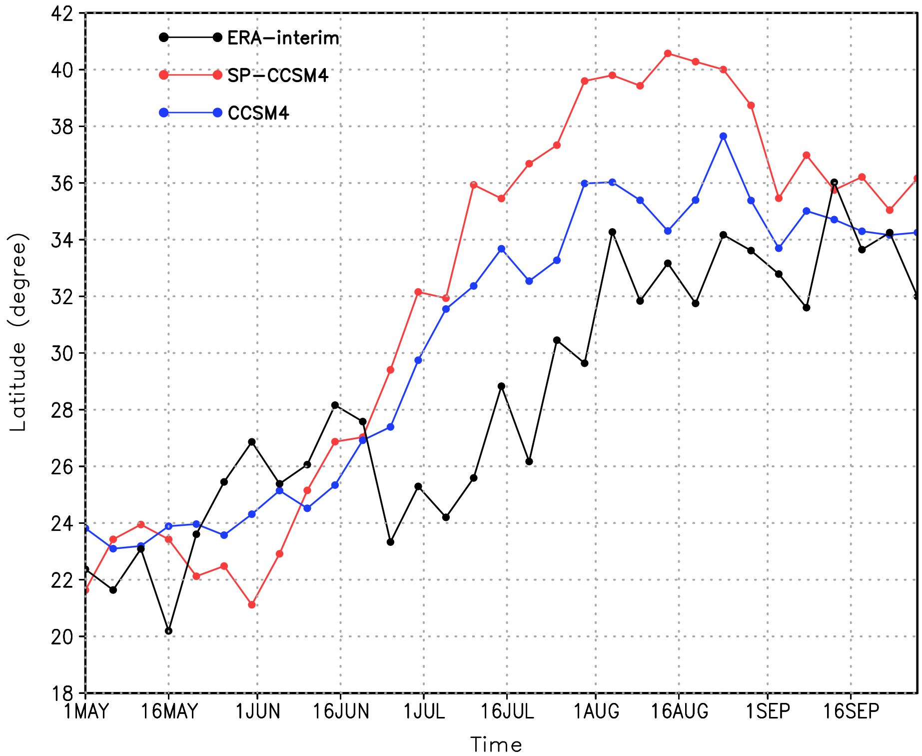

Figure 3.9: The WNPSH index based on climatological pentad mean GPH at 850 hPa, showing northward migration in observation (black), SP-CCSM4 (red) and CCSM4 (blue).

compared to observations.

3.1.3 Intraseasonal Oscillation

To compare the 30-60-day oscillation in the model and observations, a composite analysis is performed from 15 days before to 40 days after the maximum convection occurs in SCS (the method is described in Section 2.3.5). The pattern of the large OLR variance over SCS and the west Pacific is well simulated by SP-CCSM4 (Fig. 3.10a-b), but the OLR variance is larger than in observations. Here, one can also speculate that the periodicity of the CRM domain artificially enhances the variability. The maximum OLR variance in SCS present in observations is not captured by CCSM4 (Fig.3.10c). Despite the fact that variance of the

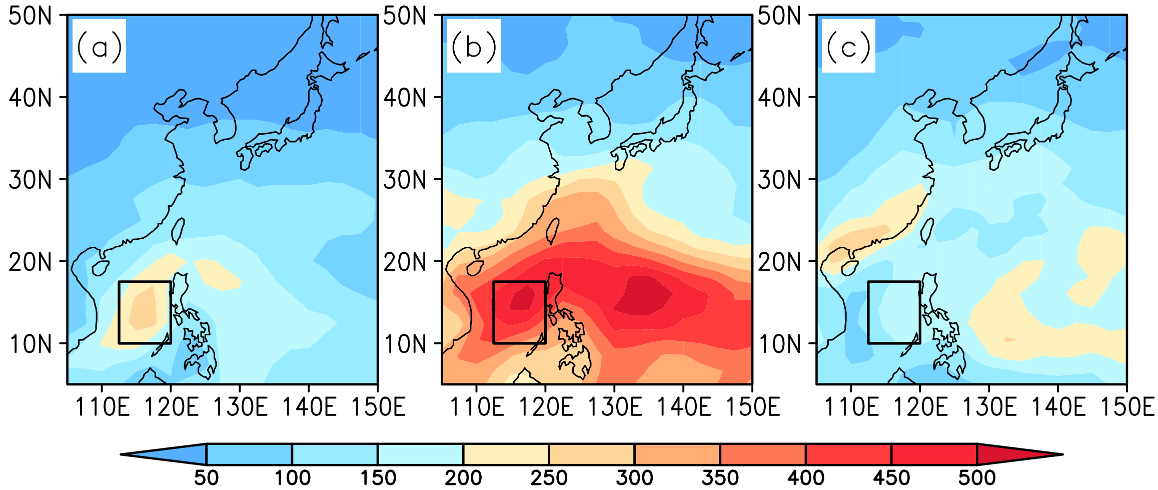

Figure 3.10: The variance of 30-60-day bandfiltered OLR daily anomaly during MJJ (unit: W^2m^{-4}). (a) Observation. (b) SP-CCSM4. (c) CCSM4. The black box (112.5-120°E, 10-17.5°N) is the region where the OLR variance reaches maximum in the observations.

SP-CCSM4 model is larger than observed, this result suggests that ISO is sensitive to the representation of cloud processes. The OLR index is defined as the area-averaged 30-60-day bandfiltered OLR where the OLR variance reaches the peak in the observation (black box in Fig. 3.10a, 112.5°E-120°E, 10°N-17.5°N). This area is unchanged when calculating the OLR index for the models. The OLR index is -13.18 W/m^2 in observation, and this index keeps the same for SP-CCSM4 and CCSM4. There are 36 events from 1979 to 2006 in observations, 53 events in SP-CCSM4, and 30 events in CCSM4 during the 30 years used in the analysis.

Figure 3.11 shows the ISO life cycle in the 30-60-day filtered OLR and 850-hPa wind field for the observations, SP-CCSM4, and CCSM4. From day -15 to day -5, both observations and models show that convection (negative OLR anomaly) over the tropical western Pacific develops and moves northwestward. In SP-CCSM4, the convective anomaly is more intense and extends further into the tropical and subtropical western Pacific. The convection starts moving northward/northwestward from day -15 in SP-CCSM4, while in the observation, the tropical convection does not propagate northwestward until day -10 when it moves eastward into the equatorial western Pacific. Therefore, the life cycle of the 30-60-day oscillation is advanced by 5 days in SP-CCSM4. In CCSM4, the convective anomaly is much weaker compared to observations (Fig. 3.11c) and moves northwestward from tropical WP into SCS from day -15 to day -5.

In SP-CCSM4, between day -10 and day -5, when the convection is intensified and moves to the tropical western Pacific, a westerly anomaly is located in the center and to the south of the convective region, and an easterly anomaly forms to its north (Fig. 3.11b). As noted in previous studies (e.g., Hsu and Weng, 2001; Kemball-Cook and Wang, 2001; Mao et al., 2010) such a flow pattern is consistent with a Gill-type Rossby wave generated by an off-equatorial heating source (Gill, 1980). However, the easterly anomaly which represents the Kelvin wave to the east of the convection is not significant after day -5. The accelerated northwestward propagation of the convection starts at around day -15 in SP-CCSM4, while in the observation it begins at day -10. In CCSM4, there are similar features in wind anomalies: cyclonic anomalies to the north of the convective center (Fig. 3.11c). These cyclonic anomalies are mostly over SCS in CCSM4.

The convection in both observations and the models reaches the peak intensity in SCS and extends to the subtropical WNP at day 0. In SP-CCSM4 (Fig. 3.11b), the convection located in the subtropical WNP is stronger and tilts northward compared to observations. The tilting can be favored by the suppressed convection (positive OLR anomaly) that SP-CCSM4 tends to produce over the West Pacific Warm Pool (WPWP). This suppressed convection appears rapidly during day 0. Afterwards, it amplifies and propagates northwestward. Meanwhile in the IO, the suppressed convection propagates westward. In the observation (Fig. 3.11a), the suppressed convection in WPWP originates from the IO and propagates eastward. Thus, the Rossby wave is more prominent in SP-CCSM4 (Fig. 3.11b). In CCSM4 (Fig. 3.11c), the magnitude of OLR anomalies and wind anomalies is smaller than observations and SP-CCSM4. Meanwhile, in CCSM4, there is no suppressed convection over WPWP as we see in SP-CCSM4. After day 0, the convection in SCS continues to move northwestward and starts dissipating in both the models and observations.

From day +5 to day +10, the dipole pattern of the active and suppressed convection over SCS and WNP has a northwest-southeast alignment in SP-CCSM4 (Fig. 3.11b), while in the observations (Fig. 3.11a) the pattern is aligned in the north-south direction. The active and suppressed convection are both stronger in SP-CCSM4. Moreover, the suppressed convection to the north of the convection dissipates rapidly in the model, whereas, in the observation, the suppressed convection persists to the north and east of the convection until day +15. It appears that the shrinkage of the northern suppressed convection favors the faster northward propagation of the convection in SP-CCSM4. In CCSM4 (Fig. 3.11c) the suppressed convection over the tropical west Pacific moves westward from day +5, and at the same time the convection over SCS dissipates rapidly.

In SP-CCSM4 (Fig. 3.11b), at day +15, the convection over SCS moves northward into Southeast China. Meanwhile the northeasterly anomaly at 30°N starts to turn into southwesterly anomaly, initiating the Mei-yu season. The Mei-yu season lasts until about day +25, and from day +30, the suppressed convection moves from WPWP into Southeast China. In the observations (Fig, 3.11a), the southwesterly flow and the convection start to develop over Southeast China at around day +20. However, the composite of band filtered wind and OLR anomalies from day +30 to day +40 are below the significance test over most regions. In CCSM4 (Fig. 3.11c), there are southwesterly anomalies and negative OLR anomalies over Southeast China from day +20 to day +25. Later on most of the OLR and wind anomalies are below 95% significance level.

The northward propagation of the active and break precipitation phases of the EASM can be seen more clearly from the zonally averaged OLR and 850-hPa wind between 110°E-120°E (Fig. 3.12a-c). In SP-CCSM4, before the Mei-yu onset, the suppressed convection to the north of convection disappears quickly, favoring the convection to move further northward. Meanwhile the convective activity at around 15°N propagates northward and rapidly moves into the Mei-yu region (around 30°N). Therefore, in SP-CCSM4, the Mei-yu season starts 5 days earlier and lasts for a shorter time period (10 days) than in observations (15 days). A similar feature can be seen in CCSM4 (Fig. 3.12c). The suppressed convection over 30°N at day 0 does not persist as long as that in observations (Fig. 3.12a), thus favoring the northward propagation of the convective anomalies.

The mechanisms proposed to explain the northward propagation of the EASM are investigated in an attempt to understand which mechanism is deficient in SP-CCSM4. Figure 3.13 shows the spatial pattern of the ISO life cycle of surface temperature superposed with OLR in observations and models. Before day 0, a warm SST anomaly is located to the northern side of the region with active convection, leading the convection to propagate northward from the Maritime Continent to SCS (Fig. 3.13a). This feature is also presented in SP-CCSM4 and CCSM4 (Fig. 3.13b and c). In observations, the maximum convection occurring in SCS is followed by a warming of SST to the south of Japan and over the Maritime Continent, and a cooling of SST in between. This cold SST leads the suppressed convection over the Maritime Continent and induces its northward propagation to SCS. At the same time, the warmer SST to the south of Japan makes the convection move northeastward. The main difference between SP-CCSM4 and observation appears after day 0 when, in SP-CCSM4, negative SST anomalies form to the south of Japan. The cold SSTs to the south of Japan do not favor the northeastward propagation of convection. In CCSM4 (Fig. 3.13c), there are positive SST anomalies to the south of Japan while negative surface temperature anomalies over East China.

In combination with the life cycle of the low-level wind pattern (Fig. 3.11), Fig. 5.12 shows that SP-CCSM4 reproduces the air-sea interaction mechanism favoring the northward propagation of the ISO. The convection (suppressed convection) induces a cyclonic (anticyclonic) circulation anomaly to its northwestern side. The northeasterly (southwesterly) anomaly to the north of the convection reduces (enhances) the prevailing southwesterly flow, and thus decreases (increases) the upward latent heat flux. The variation in latent heat flux results in the warming (cooling) of SST to the north of convection (suppressed convection), which increases (decreases) the convective instability, thus favoring the northward movement of convection (suppressed convection).

Both the models and observations (Fig. 3.14) show that before the onset of the Mei-yu

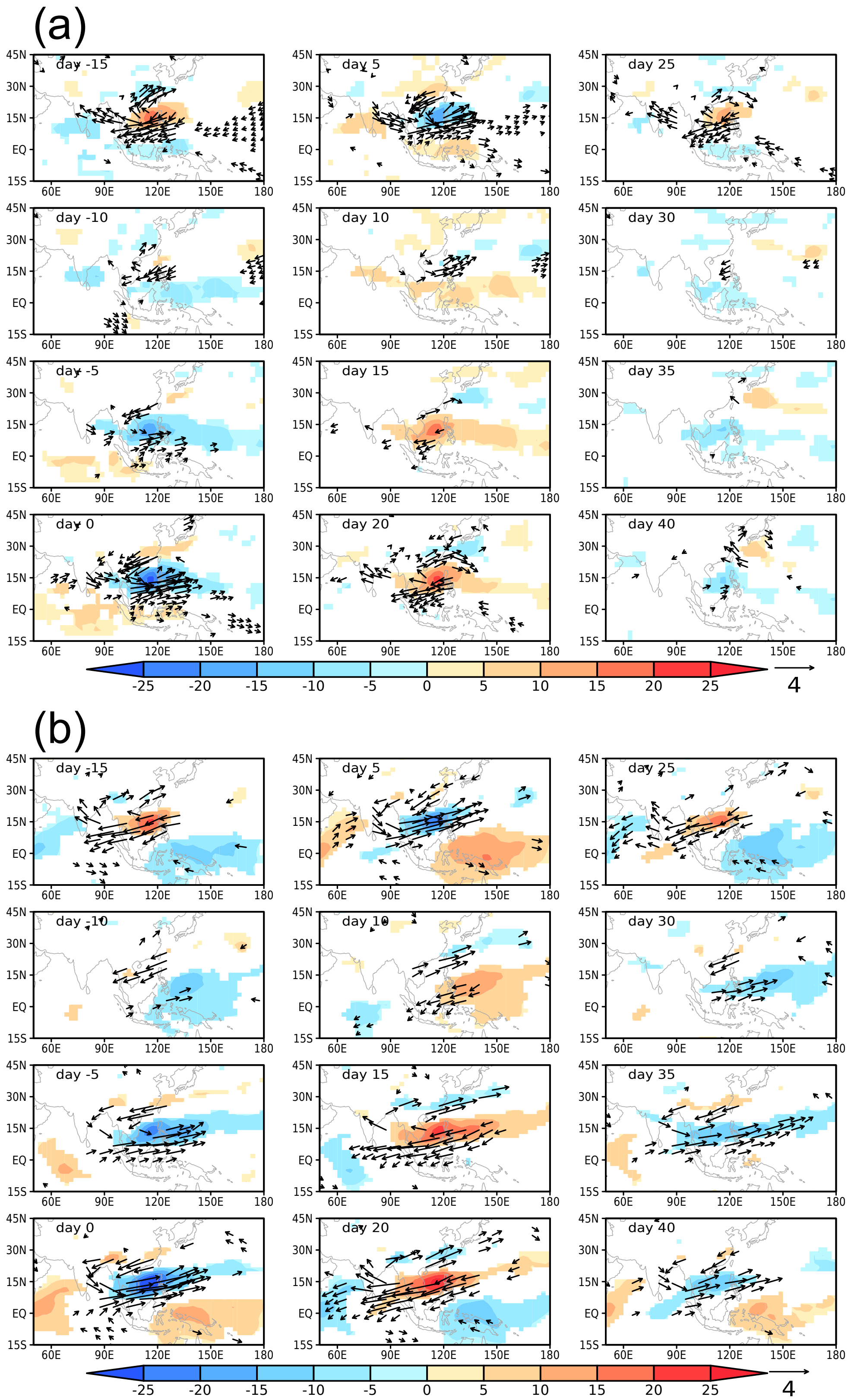
(a)
day -15
day -10
day -5
day 0
day 5
day 10
day 15
day 20
day 25
day 30
day 35
day 40
45N
30N
15N
EQ
15S
60E
90E
120E
150E
180
-25
-20
-15
-10
-5
0
5
10
15
20
25
4
(b)
day -15
day -10
day -5
day 0
day 5
day 10
day 15
day 20
day 25
day 30
day 35
day 40
-25
-20
-15
-10
-5
0
5
10
15
20
25
4

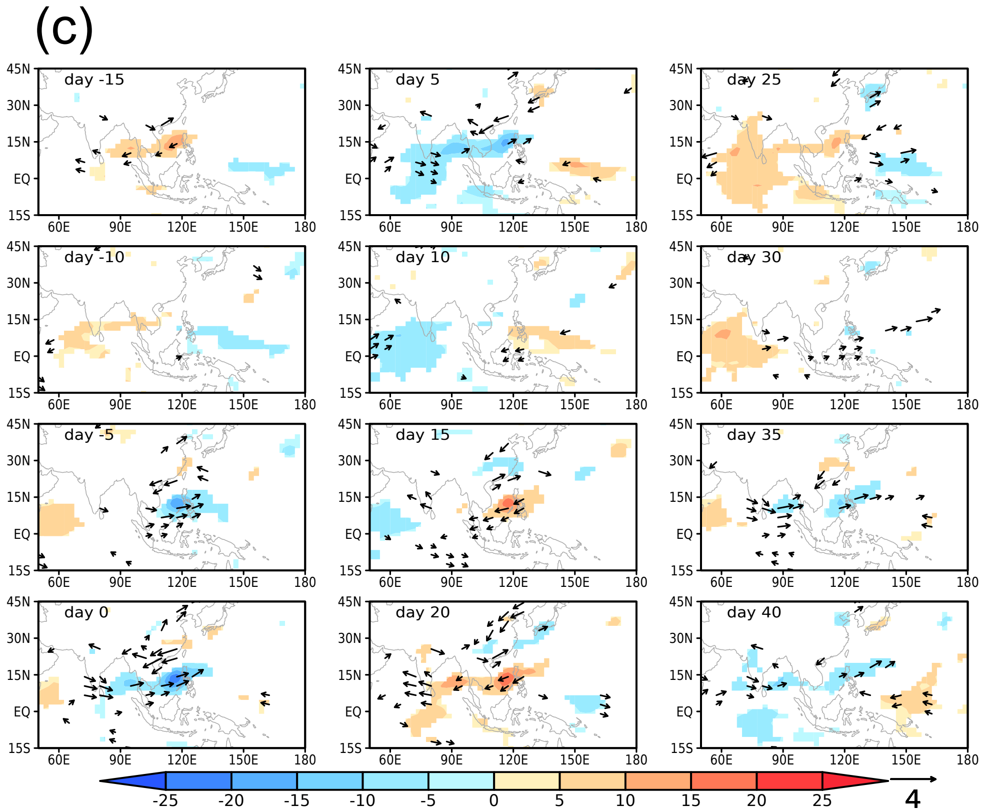

Figure 3.11: The composite of OLR (shading, unit: Wm^{-2}) and 850-hPa wind (vectors, unit: ms^{-1}) of the 12 ISO EASM phases: (a) Observation, (b) SP-CCSM4 and (c) CCSM4. Only areas above the 95% significance level are plotted.

season over Southeast China (day +20 in the observations and +15 in the models), easterly wind shear prevails to the south of the convection center (Fig. 3.14a-c). This easterly wind shear is accompanied by barotropic vorticity to the north of convection (Fig. 3.14d-f), which is consistent with the vertical shear mechanism.

The patterns of circulation and convection (Fig. 3.15b and c) simulated by the model are similar to observations (Fig. 3.15a). The cyclonic (anti-cyclonic) vorticity leads the convection (suppressed convection), staying to the north of convection (suppressed convection) and favoring the northward propagation of the convective activity. However, in

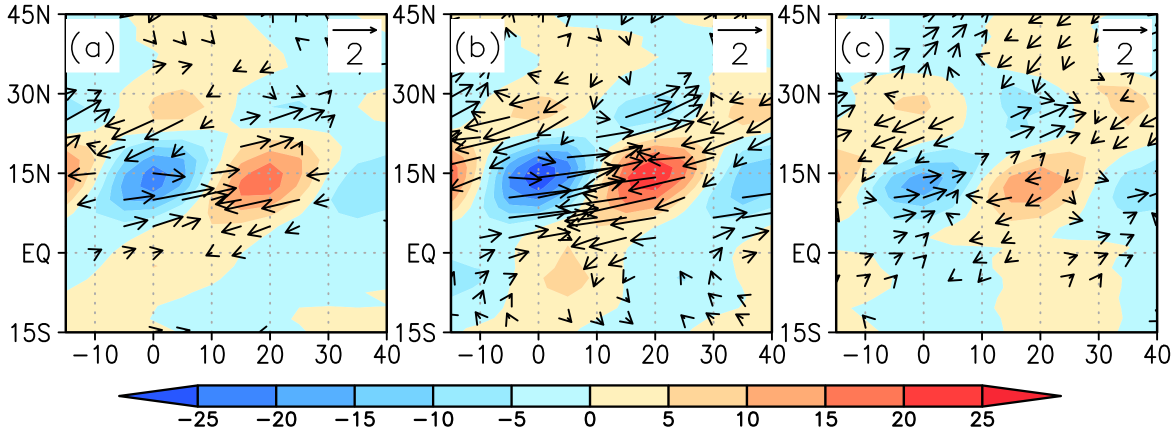

Figure 3.12: The zonally averaged (110°E-120°E) 12 phases of the ISO EASM in OLR (shading, unit: Wm^{-2}) and 850-hPa wind (vectors, unit: ms^{-1}) for (a) observations, (b) SP-CCSM4, and (c) CCSM4.The wind magnitude smaller than 0.1 ms^{-1} is not plotted.

SP-CCSM4, both the cyclonic and anti-cyclonic vorticity are more intense than in observations (Fig. 3.15a), while, in CCSM4 (Fig. 3.15c), the vorticity anomalies are relatively weaker than in observations. In both models (Fig. 3.15b and c), the anti-cyclonic vorticity before day +10 propagates faster than that in observations (Fig. 3.15a), creating conditions for the northward movement of the cyclonic vorticity.

The composite of the zonally averaged low-level moisture convergence (Fig. 3.15d-f) shows a similar pattern to the vorticity field. SP-CCSM4 (Fig. 3.15e) simulates a stronger moisture convergence (divergence) compared to the observations (Fig. 3.15d), whereas in CCSM4 (Fig. 3.15f), the magnitude of moisture convergence is comparable to observations. Meanwhile, the moisture convergence (divergence) is located slightly to the north of convective (suppressed convection) center, which is similar to observation. The cyclonic vorticity and moisture convergence to the north of the convection also tend to destabilize the atmospheric boundary layer, thus driving the convection moving northward.

(a)

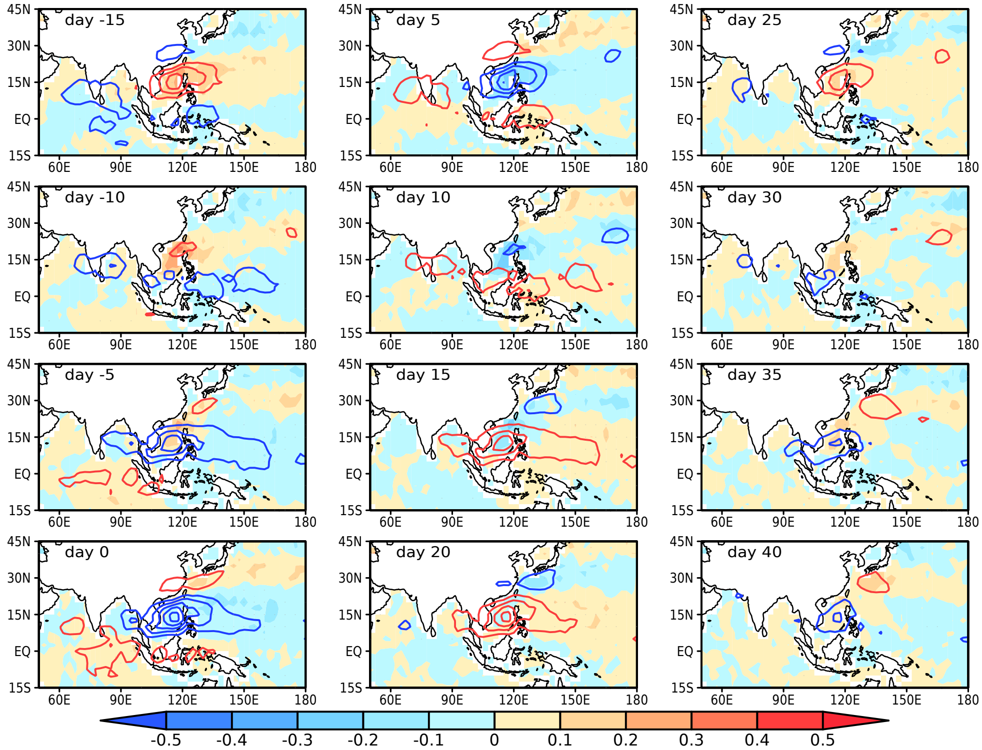
day -15
day -10
day -5
day 0
day 5
day 10
day 15
day 20
day 25
day 30
day 35
day 40
45N
30N
15N
EQ
15S
60E
90E
120E
150E
180
-0.5
-0.4
-0.3
-0.2
-0.1
0
0.1
0.2
0.3
0.4
0.5

(b)

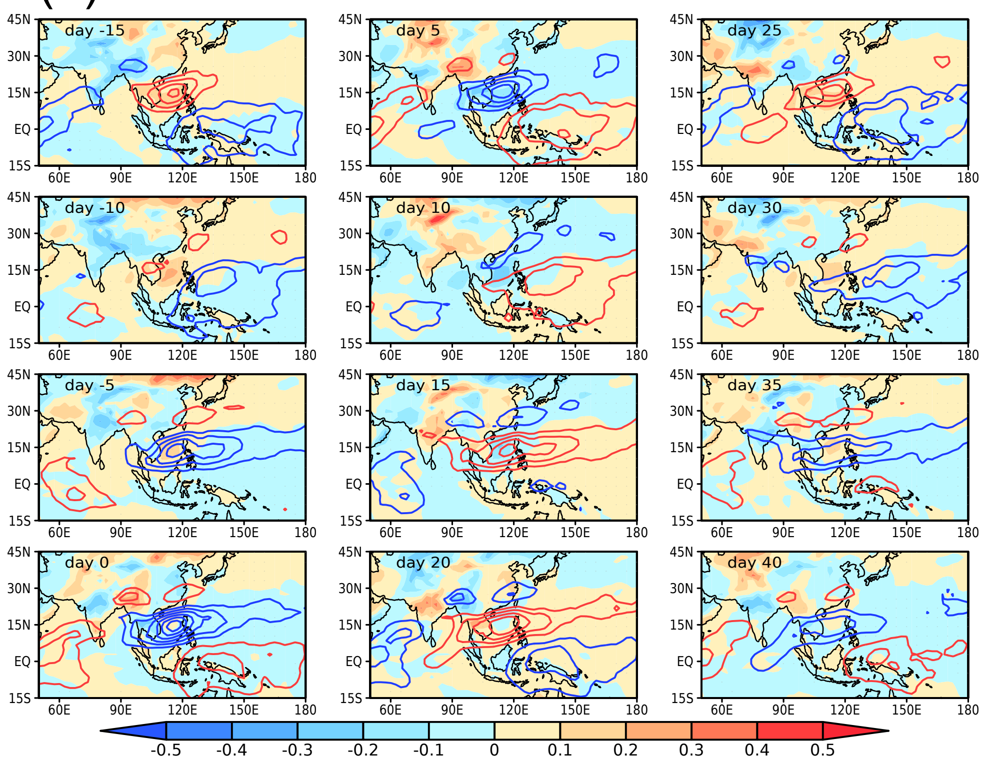
day -15
day -10
day -5
day 0
day 5
day 10
day 15
day 20
day 25
day 30
day 35
day 40
45N
30N
15N
EQ
15S
60E
90E
120E
150E
180
-0.5
-0.4
-0.3
-0.2
-0.1
0
0.1
0.2
0.3
0.4
0.5

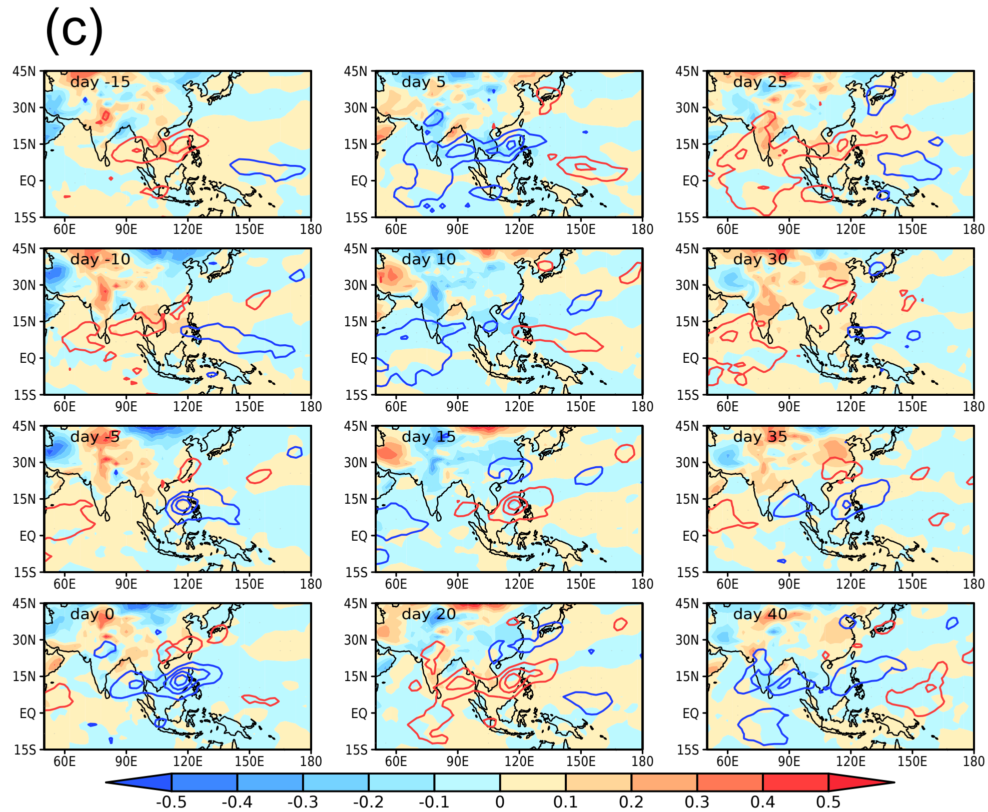

Figure 3.13: Same as Fig. 3.11, but for the composite of surface temperature (shading, unit: K) and OLR (contours, unit: Wm^{-2}). The blue contours denote convective anomalies, and the red contours represent suppressed convective anomalies. The contour interval is 5 Wm^{-2}, and minimum (maximum) value for convective (suppressed convective) anomalies is 5 (-5) Wm^{-2}. The gray dots indicate the areas where the composite SST is above 95% significance level.

3.2 Dry and Wet WPWP cases

In Subsection 3.1.3, it was mentioned that the most prominent difference in intraseasonal variability of the EASM between observations and SP-CCSM4 is related to the suppressed convection anomaly over WPWP. In SP-CCSM4, this suppressed convection could result in the earlier onset of the Mei-yu season and in the faster northward propagation. This hypothesis will be verified using observational data.

The dry and wet WPWP cases are defined based on the OLR anomaly over WPWP at

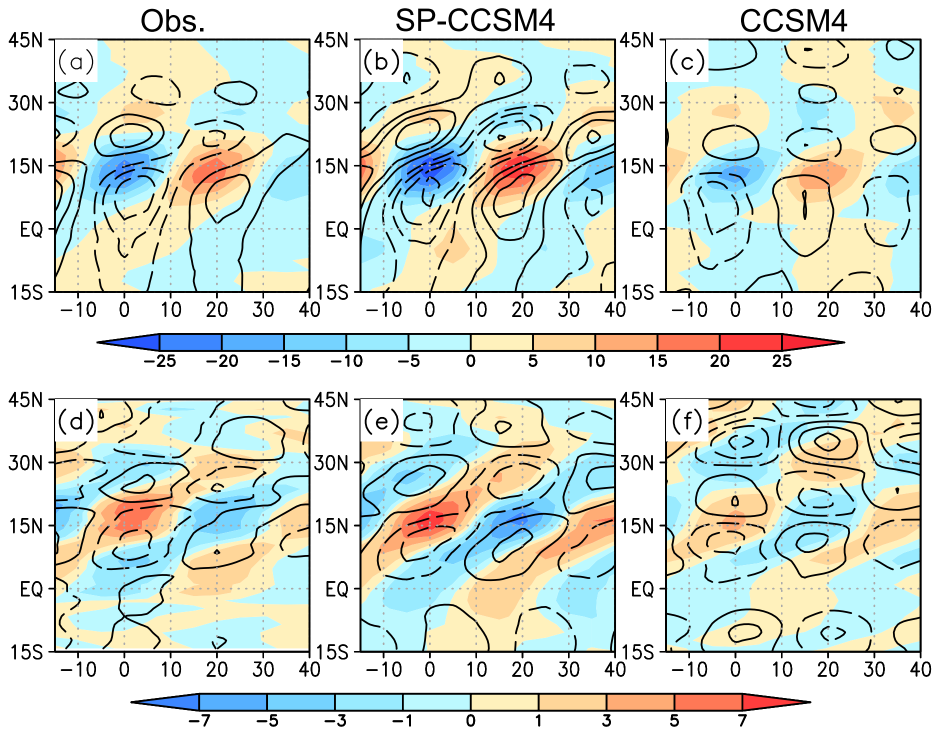

Figure 3.14: (a)-(c) The zonally averaged (110°E -120°E) OLR (shading, unit: Wm^{-2}) and vertical wind shear based on the difference between the zonal wind at 200 hPa and 850 hPa (contours, unit: ms^{-1}), (d)-(f) The zonally averaged 850-hPa vorticity (shading, unit: $10^{-6}\mathrm{s}^{-1}$) and 200-hPa vorticity (contours, unit: $10^{-6}\mathrm{s}^{-1}$). (a) and (d): Observations. (b) and (e): SP-CCSM4. (c) and (f): CCSM4. In (a)-(c) the solid contours denote westerly wind shear, and the dashed contours denote easterly wind shear. The contour interval is 1 ms^{-1}. In (d)-(f) the solid contours denote the cyclonic vorticity at 200 hPa, and the dashed contours denote the anti-cyclonic vorticity at 200 hPa. The contour interval is $2\times10^{-6}\mathrm{s}^{-1}$.

day 0. When there is a positive OLR anomaly over equatorial WP to the east of 120°E it is defined as dry WPWP case. Otherwise, it is wet WPWP case. In observation, during MJJ from 1983 to 2012, there are 11 dry WPWP cases and 10 wet WPWP cases. Figure 3.16 shows examples of dry and wet WPWP cases. For the dry WPWP case on 7 July 2002, the positive OLR anomaly is mainly located to the east of 120°E and extends to 180°E. Whereas in the wet WPWP case on 22 June 2006, the center of the maximum negative OLR anomaly is located to the east of 140°E.

The composite of the ISO life cycle is constructed for the dry and wet WPWP cases.

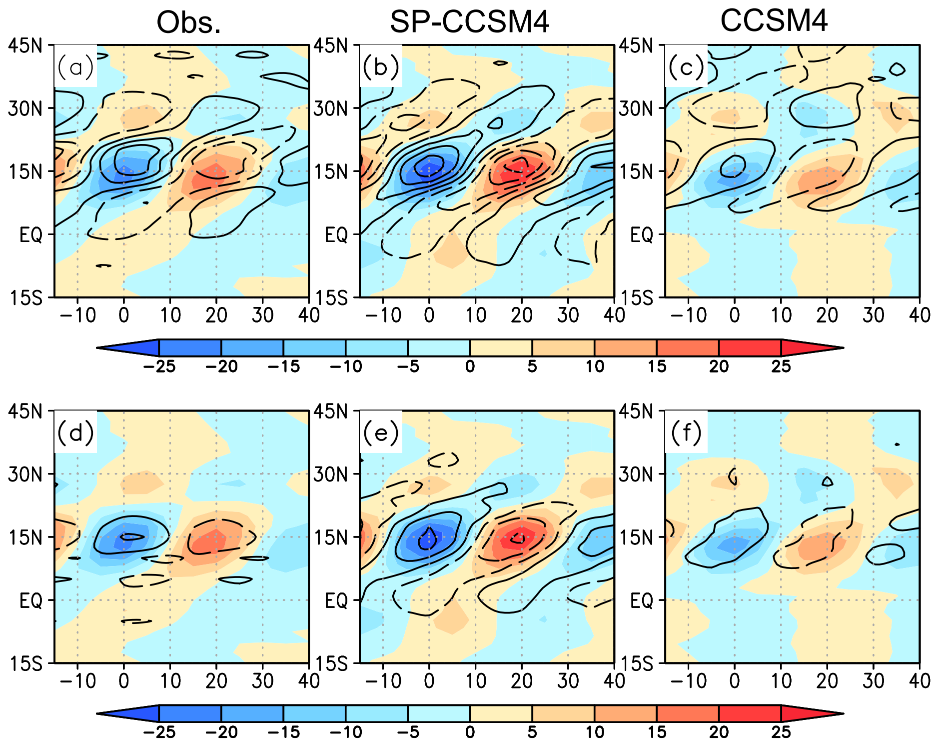

Figure 3.15: Same as Fig. 3.14, but (a)-(c) are the zonally averaged (110°E-120°E) OLR (shading, unit: Wm^{-2}) and 850-hPa vorticity (contours, unit: $10^{-6}s^{-1}$), (d)-(f) are the zonally averaged OLR (shading, unit: Wm^{-2}) and 1000-hPa moisture convergence (contours, unit: $10^{-8}s^{-1}$). (a) and (d): Observations. (b) and (e): SP-CCSM4. (c) and (f): CCSM4. In (a)-(c) the solid contours denote cyclonic vorticity, and the dashed contours denote anticyclonic vorticity. The contour interval is $2\times10^{-6}s^{-1}$. In (d)-(f) the solid contours denote moisture convergence, and the dashed contours denote moisture divergence. The contour interval is $2\times10^{-8}s^{-1}$.

Figure 3.17 shows the life cycle of the 30-60-day band filtered OLR and 850-hPa wind for the dry and wet WPWP cases, respectively.

Before day 0, both the dry and wet WPWP cases show the dissipation of the suppressed convection (positive OLR anomaly) over SCS from day −15 to day −10, and the subsequent development of the enhanced convection (negative OLR anomaly) from day −15 to day 0. The difference between the dry and wet WPWP cases before day 0 lies in the convective activity over IO and tropical WP. Before day 0, in the dry WPWP case (Fig. 3.17a), there is a suppressed convection over eastern IO at day −15. It develops and covers almost the

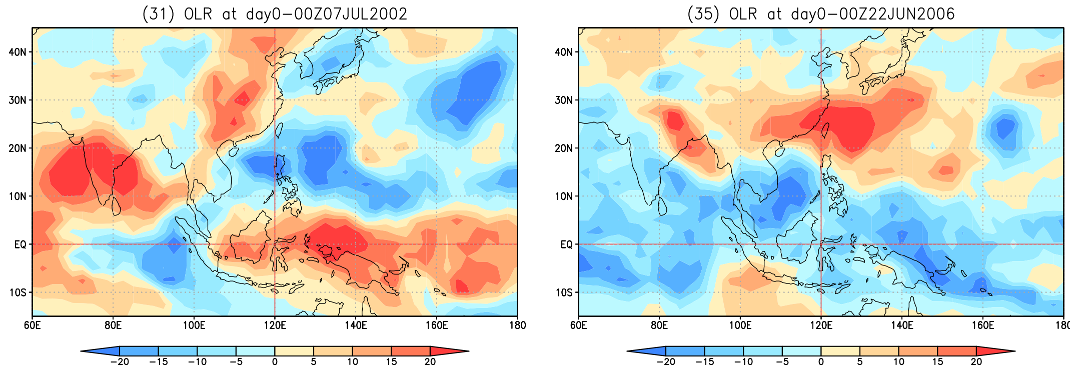

Figure 3.16: Examples of dry (left) and wet (right) WPWP cases at Day 0.

entire IO at day −5. In addition, the enhanced convection over tropical WP amplifies and moves westward into SCS. In the wet WPWP case (Fig. 3.17b), the IO is covered by the enhanced convection at day −15. The enhanced convection propagates eastward, and at day 0 the suppressed convection dominates the IO. Meanwhile, the suppressed convection over tropical WP dissipates from day −15 to day −5.

At day 0, the convection reaches the maximum over SCS in both dry and wet WPWP cases. As mentioned above, over WPWP, there is suppressed convection in the dry WPWP cases, and enhanced convection in the west WPWP cases.

Later on, in the dry WPWP case (Fig. 3.17a), the suppressed convection over the WPWP expands and propagates northward from day 5 to day 10. Then it moves quickly from WNP to SCS at day 15, and reaches the peak at day 20. In the wet WPWP case (Fig. 3.17b) the suppressed convection over IO develops and propagates eastward. It reaches the Maritime Continent at day 10. Then it moves northward into SCS at day 15 and reaches the maximum at day 20.

The suppressed convection over SCS starts dissipating after day 20 in both dry and wet WPWP cases. In the dry WPWP case (Fig. 3.17a), the suppressed convection over SCS disappears at day 30, and meanwhile, the enhanced convection over WPWP migrates northwestward into SCS. In the wet WPWP case (Fig. 3.17b), the suppressed convection over SCS disappears at day 35, and the enhanced convection over SCS is not as strong as that in the dry WPWP case.

The northward propagation of the active and suppressed convection over East China can be seen more clearly from the zonally averaged OLR and 850-hPa wind between 110°E and 120°E (Fig. 3.18). In the dry WPWP case, the convective activity and wind is more intense than that in the wet WPWP case. In the dry WPWP case (Fig. 3.18a), the suppressed convection over tropics propagates northward, pushing the active convection over SCS to move. Meanwhile, the suppressed convection at around 30°N dissipates quickly, which also favors the convection to move northward. At day 15, the convection and the southwesterly flow reaches Southeast China, initiating the Mei-yu season which lasts around day 25. At day 30, another active convection appears over SCS. In the wet WPWP case (Fig. 3.18b) the northward propagation of OLR anomaly is not as prominent as that in the dry WPWP case (Fig. 3.18a). The suppressed convection at 30°N prevents the convection moving northward, and the Mei-yu onset is not clear. At day 35, the second convection appears over SCS. Therefore, the cycle of the ISO in the dry WPWP case is about 5 days shorter than in the wet WPWP case.

The northward propagation of ISO is also analyzed over WP by making the zonal average between 120°E and 140°E (Fig. 3.19). The difference between the dry and wet WPWP cases is prominent. In the dry WPWP case (Fig. 3.19a), the tropical suppressed convection advances northward, favoring the northward propagation of the convection to its north. In the wet WPWP case (Fig. 3.19b), the northward propagation is not clear before day 5, but after day 5, the active and suppressed convection moves northward. However, the magnitude of the convection is smaller than that in the dry WPWP case.

In addition to the northward propagation of the ISO, the zonal migration is also analyzed by taking meridional average between 10°S and 10°N, and between 10°N and 20°N (Fig. 3.20 and Fig. 3.21, respectively). The former one aims to track the zonal propagation in the equatorial region, while the latter one intends to find out where the convection over SCS comes from.

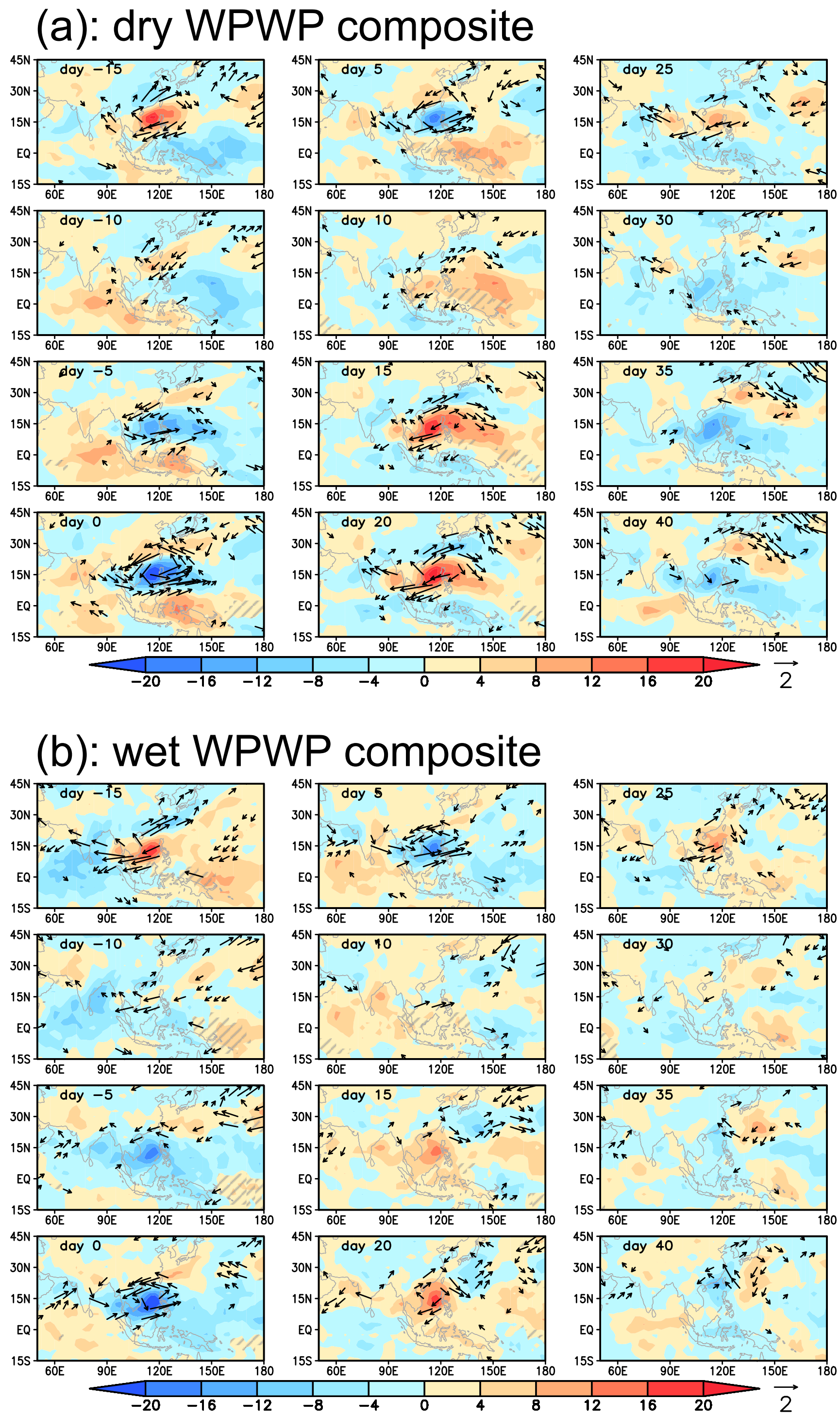

Figure 3.17: he composite of OLR (shading, unit: Wm^{-2}) and 850-hPa wind (vectors, unit: ms^{-1}) of the 12 ISO EASM phases: (a): dry WPWP case. (b): wet WPWP case. The areas above the 95% significance level are highlighted by grey slashes.

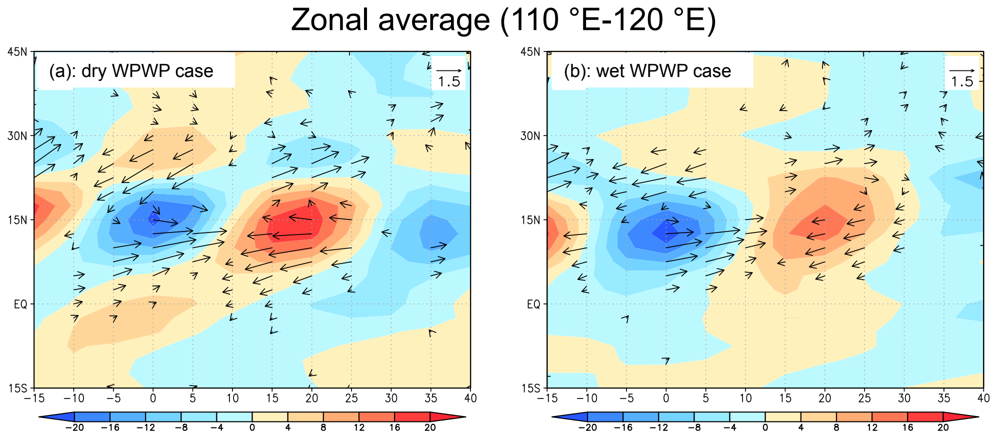

Figure 3.18: The zonally averaged (110°E-120°E) 12 phases of the ISO EASM in OLR (shading, unit: Wm^{-2}) and 850-hPa wind (vectors, unit: ms^{-1}) for (a) dry WPWP case, (b) wet WPWP case. The wind smaller than 0.1 ms^{-1} is masked out.

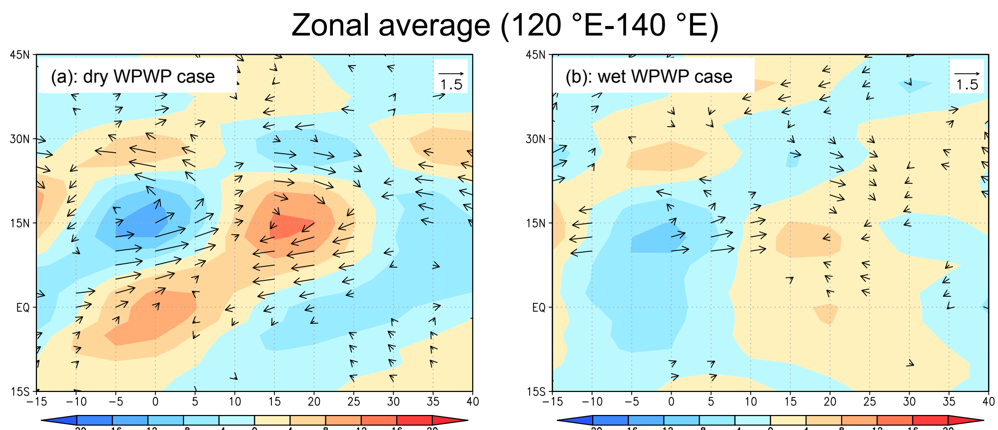

Figure 3.19: Same as Fig. 3.18, except the zonal average is computed between 120°E and 140°E.

In the dry WPWP case (Fig. 3.20a), the suppressed convection over tropical WP shows eastward propagation, while the zonal movement over IO is not obvious. Over 10°N-20°N, there is westward propagation of the ISO (Fig. 3.21a). The convective activity over SCS is related to the westward propagation of active/suppressed convection over WNP.

In the wet WPWP case (Fig. 3.20b and Fig. 3.21b), the active and suppressed convection

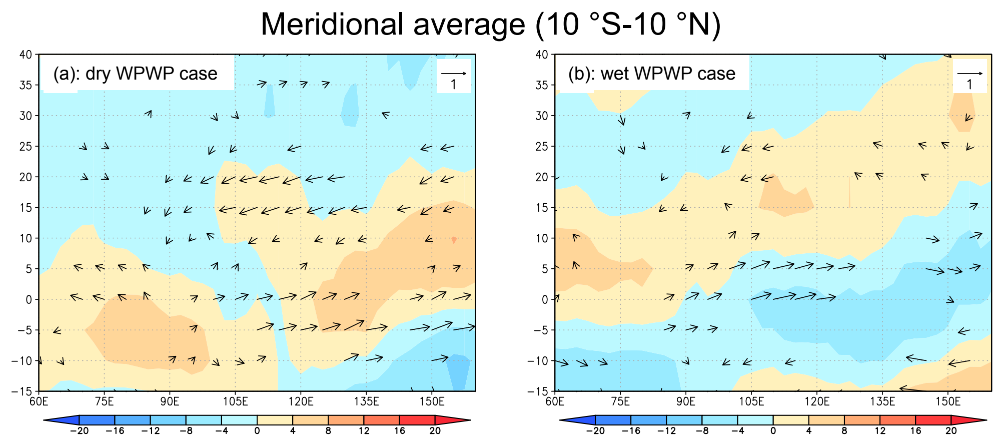

Figure 3.20: The meridionally averaged (10°S-10°N) 12 phases of the ISO EASM in OLR (shading, unit: Wm^{-2}) and 850-hPa wind (vectors, unit: ms^{-1}) for (a) dry WPWP case, (b) wet WPWP case. The wind smaller than 0.1 ms^{-1} is masked out.

show eastward propagation. Over the equatorial region, the convective activity moves eastward from IO to WP (Fig. 3.20b), while over the region 10°N-20°N (Fig. 3.21b), the eastward propagation cannot exceed SCS.

To summarize, in the dry WPWP case, the ISO of the EASM shows northward and westward propagation, whereas in the wet WPWP case, the ISO is dominated by the eastward propagation.

3.3 Summary and Discussion

The ability of SP-CCSM4 to simulate the observed features of EASM was evaluated by comparing the model output with observations and CCSM4, including the seasonal mean state, the annual cycle, and the ISO associated with the EASM variability. The model captures the main features of the EASM observed climatology and the mechanisms related to its northward propagation.

The MJJA mean state of EASM is better simulated by SP-CCSM4 than by CCSM4. However, both models underestimate the amount of precipitation over the EASM area. In SP-CCSM4, the rainfall deficiency results from a combination of factors including a

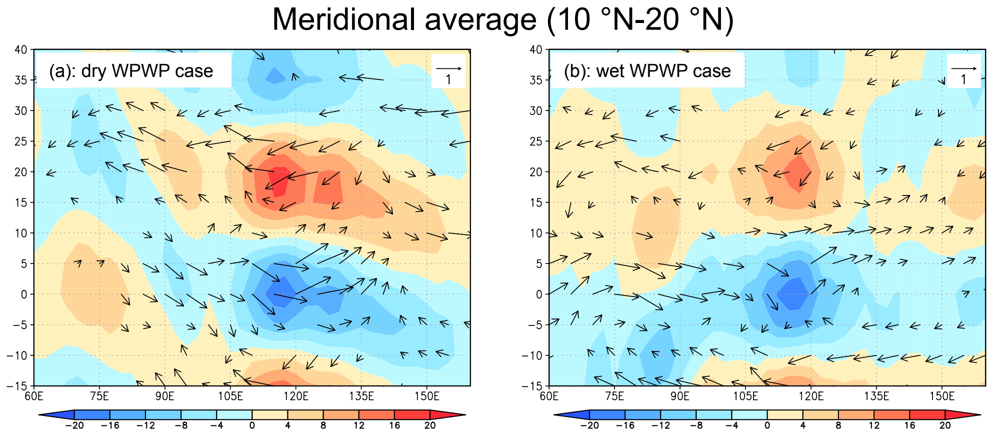

Figure 3.21: Same as Fig. 3.20, except the meridional average is computed between 10°N and 20°N.

northward-displaced WNPSH and less moisture transport over the EASM region. In CCSM4, the WNPSH extends westward, leading to a moist intrusion to central and northeastern China as well as northern Japan.

The SP-CCSM4 also captures many aspects of the stepwise northward propagation of the precipitation belt in the EASM region. The shortcomings of the model in simulating the seasonal march are the early onset and shorter duration of the Mei-yu season and the more extreme northernmost position of the subtropical rain belt. The northward expansion of the edge of the subtropical rain belt is related to the northward migration of the WNPSH ridge line simulated by the model. However, in CCSM4, the EASM onset at mid-May is not reproduced, plus the whole rain band over subtropics is displaced northward.

The underestimation of the EASM precipitation is a common problem among the current generation of climate models (Chen et al., 2010; Sperber et al., 2013; Zhou and Li, 2002). The rainfall deficiency in models is largely related to the flaws in the WNPSH simulation. In SP-CCSM4, there is a weaker low level southerly flow over SCS and cyclonic circulation anomalies over WNP (Fig. 3.4a-c), which is similar to the multi-model mean of CMIP5 and CMIP3 (Sperber et al., 2013, Fig. 2). The annual cycle of EASM is better simulated by SP-CCSM4 than some other models. The SP-CCSM4 reproduces the northward propagation of the subtropical rain belt with a reasonable EASM onset, except for the bias in the Mei-yu episode and the northernmost position of the rain belt. The super-parameterization shows significant improvements over CAM3.5 with different convection schemes, where the whole subtropical rain belt is displaced northward and the monsoonal precipitation lasts longer (Chen et al., 2010).

The SP-CCSM4 captures the mechanisms related to the northward propagation of the EASM ISO. In boreal summer, the ISO-related convective heating over the Maritime Continent and SCS induces a low-level cyclonic anomaly to the northwestern side of the convective region. The induced northeasterly anomaly reduces the prevailing southwesterly flow. The change in the low-level wind reduces the latent heat flux, leading to a warmer SST to the north of convection. This warmer SST tends to destabilize the atmospheric boundary layer, thus favoring the northward propagation of convection. Meanwhile, the presence of the easterly vertical shear and the barotropic vorticity to the north of the convective activity also contributes to the northward propagation of ISO. The difference between the model and observation is that the northwestward propagation starting from WNP occurs earlier and moves faster in the model. In addition, the Mei-yu season begins earlier and does not last as long as that in the observation.

The analysis of mechanisms responsible for the northward propagation does not indicate large discrepancies between their representation in SP-CCSM4 and observations. The largest difference between SP-CCSM4 and observations is a region of suppressed convection over WPWP, which is present only in SP-CCSM4 (Fig. 3.11). This suggests that the earlier onset of the Mei-yu season and the faster northward propagation could be attributed to the suppressed convection over this region.

To further investigate this hypothesis, a composite analysis was applied to the observational data. The ISO cases are divided into dry WPWP case and wet WPWP case based on the convective activity over WPWP when the convection reaches the peak over SCS. The result reveals that, in the dry WPWP case, the ISO shows faster northward propagation over East China and WNP, which is related to the earlier onset of the Mei-yu season.

Also, the development of the convection over SCS is due to the northward and westward propagation of ISO. While in the wet WPWP case the northward propagation occurs over WNP, and it is not obvious over East China. The Mei-yu onset is not as clear as that in the dry WPWP case. Additionally, the ISO movement is dominated by the eastward propagation. However, there are not enough cases in the observations (11 dry WPWP cases and 10 wet WPWP cases). If a statistically significant result is to be obtained, a longer record of observations or a longer model simulation is required.

Chapter 4: EASM simulation in SP-CCSM4 under Future Climate Condition

In this chapter the EASM simulations by SP-CCSM4 under global warming scenario are analyzed, including its mean state, annual cycle, and intraseasonal variability. The global warming scenario is simulated by quadrupling atmospheric CO_2 concentration in SP-CCSM4. In addition the EASM responses to various global warming conditions are further investigated. Based on the analysis a hypothesis is proposed to explain the changes of the EASM under the global warming scenario. According to this hypothesis, the warming of surface boundary plays a more important role in the changes of EASM mean state than the atmospheric warming due to external forcing. Meanwhile, the EASM mean state is affected by the local air-sea interaction over SCS and nearby WP. The local air-sea interactions over SCS and WP modulate the convective activity in the region via surface evaporation. The occurrence of convection then prevents the WNPSH from extending westward.

4.1 Model Simulations

In this section, four model simulations are used to study the changes of the EASM under various global warming scenarios, including two coupled runs and two AMIP-type runs. The initial conditions for all the four model simulations were taken from the CCSM4 twentieth-century runs. They were initialized in January 2006. Two coupled simulations were run for 150 years, and two AMIP-type simulations were run for 35 years. All the four model simulations have the same resolution with 1.9° (latitude) × 2.5° (longitude).

A brief summary of these four model simulations is listed in Table 4.1. The coupled runs are: coupled present-day control with atmospheric CO_2 concentration of 368.9 ppmv

Table 4.1: Brief information of four model simulations.

Model Simulation	Atmospheric CO_2 (ppmv)	Initial Condition	Boundary Condition
pdControl	368.9	CCM4 20^{th} century	ocean model generated SST
cpl_4×CO_2	1475.0		
amip_4×CO_2	1475.0		observed SST
amip_4K	368.9		observed SST + 4K

(pdControl), and the coupled warming scenario with the abrupt quadrupling of CO_2 concentration used in the pdControl run (cpl_4×CO_2). The first AMIP run uses boundary conditions derived from observed climatology and the same atmospheric CO_2 concentration as in cpl_4×CO_2 (amip_4×CO_2). In the second AMIP run (amip_4K), the observed boundary conditions are perturbed by a uniform 4K SST increase and the atmospheric CO_2 concentration is the same as in the pdControl run. In the coupled runs, the atmosphere and ocean are fully coupled. The heat, momentum, and moist are exchanged at the air-sea interface. In the uncoupled runs, the air-sea interaction is cut off and the ocean cannot respond to the atmospheric forcing. Thus, the amip_4×CO_2 run shows only the impact of quadrupling the CO_2 level on the atmosphere, whereas the amip_4K run shows the direct effect of SST warming on the atmosphere. The complete description of these runs is given by Bretherton et al. (2014). Firstly, the EASM response to global warming will be analyzed by comparing the EASM simulation in pdControl and cpl_4×CO_2, including the seasonal mean, annual cycle, and ISV.

4.2 EASM Response to Global Warming

4.2.1 Seasonal Mean State

The climatological MJJA mean precipitation and 850-hPa GPH are illustrated in Fig. 4.1 for pdControl, cpl_4×CO_2, along with their differences. The most prominent difference in precipitation between them is that the Intertropical Convergence Zone (ITCZ) moves equatorward in cpl_4×CO_2. The precipitation over SCS and WP is significantly reduced in cpl_4×CO_2 compared to pdControl run between 10°-20°N, while it is intensified over the EASM region to the north of 20°N and near the equator.

In pdControl run, maximum precipitation occurs over SCS and adjacent WP. There is also large amount of rainfall over the area from South China to southern Japan. In cpl_4×CO_2 the precipitation is decreased significantly over part of the tropics, and increased over East Asia area. The WNPSH also changes in response to the global warming conditions. In the pdControl run, the western edge of the 1540-m isoline reaches 160°E. It is located along 30°N and tilts northward when it approaches the East Asian continent. In the cpl_4×CO_2 run, the WNPSH intensifies and extends westward: the isoline of 1540-m reaches 140°E and the western portion of the WNPSH tilts southward. Because precipitation tends to form to the northwestern flank of WNPSH, the magnitude of precipitation over the EASM area is larger in the cpl_4×CO_2 run.

The climatological MJJA mean state can be seen more clearly by zooming over the EASM area (Fig. 4.2). In the warmer climate, the tropical monsoon trough is weakened while the subtropical monsoon trough is strengthened (Fig. 4.2c). The precipitation is also increased over northern China and Korean Peninsula. The intensification of monsoonal precipitation in the warming climate scenario is related to the enhanced southwesterlies and associated moisture transport to the EASM area (Fig. 4.2d-i). The changes in the low-level wind and moisture transport is associated with the spatial distribution of the WNPSH (Fig. 4.1). In boreal summer, the low-level wind prevailing over East Asia consists of two branches. The westerly wind over SCS turns into southerly wind when it flows

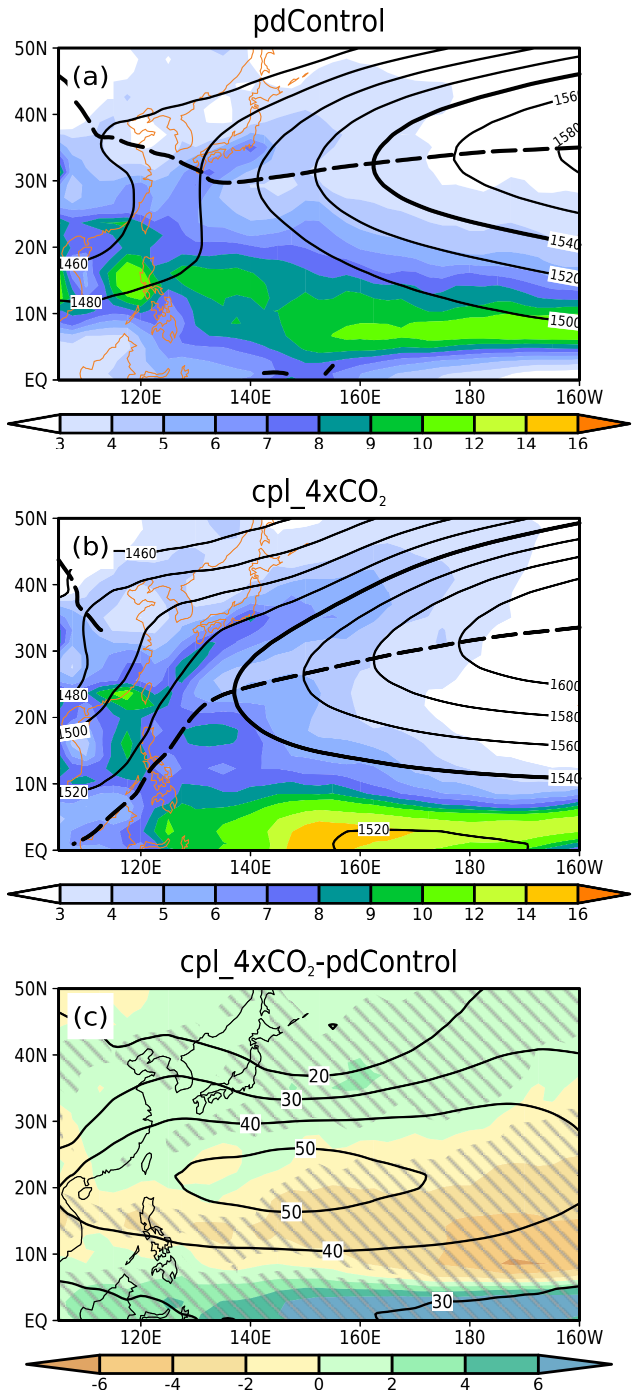

Figure 4.1: MJJA mean precipitation rate (shadings, unit: mm/day) and geopotential height at 850 hPa (contours, unit: m) in (a) pdControl, (b) cpl_4×CO_2, and (c) the difference between cpl_4×CO_2 and pdControl. The dashed line in (a) and (b) denotes the subtropical ridge. The grey slashes in (c) denote the regions where the precipitation exceeds the 95% significance level.

into East Asia area, and the southeasterlies on the southern side of the WNPSH turn into southerlies/southwesterlies on the western/northwestern side of the WNPSH. In the pdControl run, most of the East Asian area is covered by southerly flow (Fig. 4.2d). Because the subtropical ridge is located around 30°N, most part of the East Asian region between 20°N and 40°N is covered by southerlies because this region is located on the western side of WNPSH. In the cpl_4×CO_2 run, the East Asian area is dominated by southwesterlies (Fig. 4.2e) because the westward extension of WNPSH puts the region to the northwest flank of WNPSH.

The moisture transport over East Asia has a similar structure as the low-level wind. The westerly flow brings moisture from IO and SCS, and the southeasterly flow transports moisture from WNP. These two branches of moisture converge over East Asia and contribute to the precipitation formation there. In the pdControl run, the moisture flows northward over most part of the EASM area (Fig. 4.2g) whereas, in the cpl_4×CO_2 run, the moisture flows northeastward and the magnitude of the moisture transport is largely amplified, especially over northern China, Korean peninsula, and Japan (Fig. 4.2h-i).

Xiang et al. (2013) showed that WNPSH is influenced by a convection-wind-evaporation-SST feedback occurring over the WNP, and Li et al. (2012) pointed out that the changes of WNPSH in a warming climate is affected by the land-sea thermal contrast. The vertically integrated diabatic heating (Fig. 4.3) shows that global warming induces the increase of convective activity in the equatorial Pacific and suppression of convection in the WNP between 10°N-20°N. In pdControl run, there is large diabatic warming over ITCZ, which is located at 5°N-10°N over Pacific Ocean and at 10°N-20°N over SCS. In cpl_4×CO_2 run, the diabatic warming band moves to equatorial region, corresponding to the equatorward displacement of the ITCZ (Fig. 4.1b). The southward movement of the ITCZ leads to a diabatic cooling over tropical Pacific Ocean (10°N-20°N) and the resultant amplification of the WNPSH, consistent with the findings of Xiang et al. (2013).

Figure 4.4 depicts the MJJA mean meridional circulation averaged between 110°E and 120°E in pdControl, cpl_4×CO_2, and their difference. In pdControl run, there are two

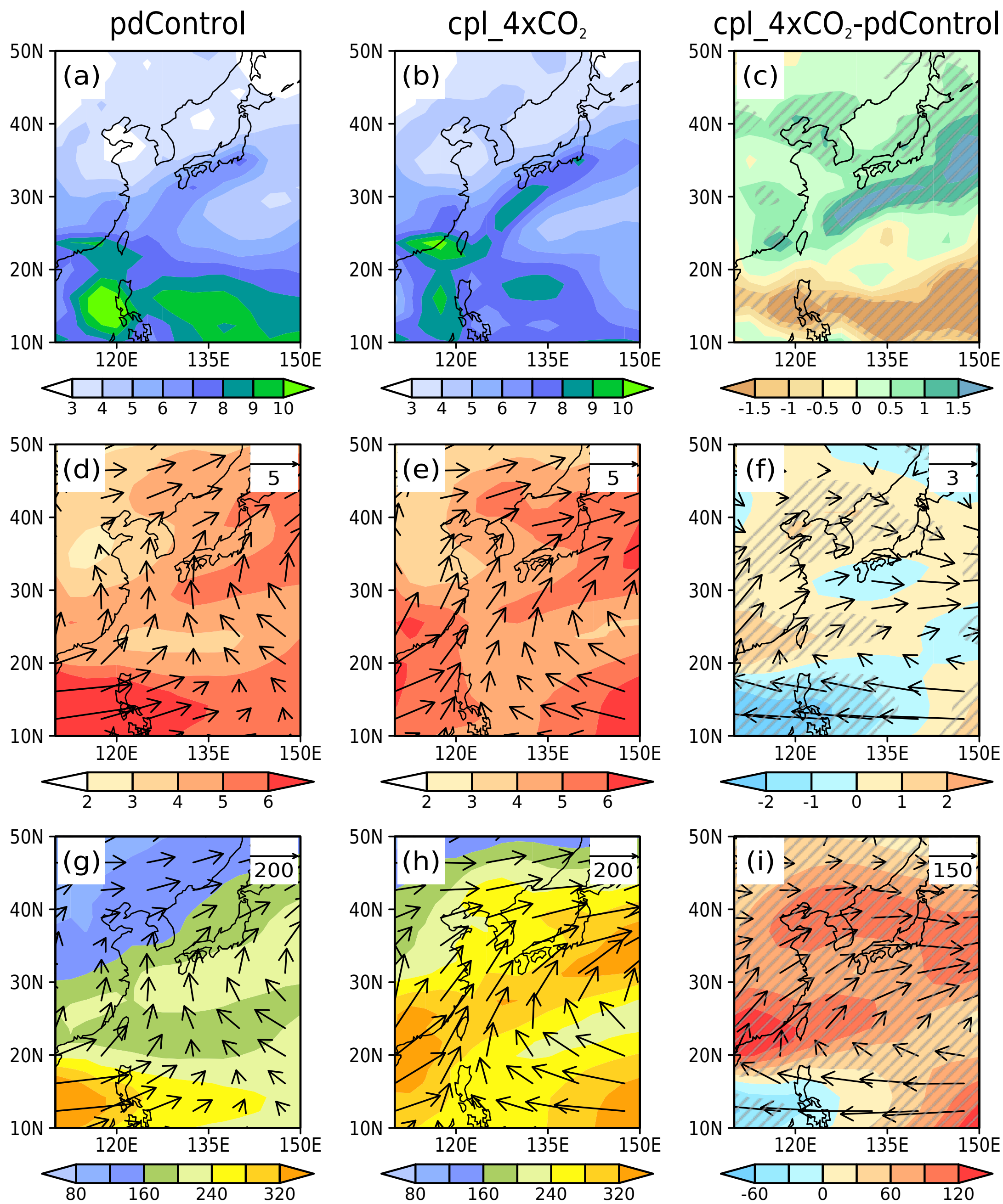

Figure 4.2: MJJA mean state over East Asia in pdControl, cpl_4$\times CO_2$, and their difference. (a-c): precipitation rate (unit: mm/day), (d-f): magnitude and direction of wind at 850 hPa (unit: m/s), (g-i): magnitude and direction of the vertically integrated moisture transport (unit: $\mathrm{Kgm^{-1}s^{-1}}$). The grey slashes in (c),(f), and (i) denote the regions exceeding the 95% significance level.

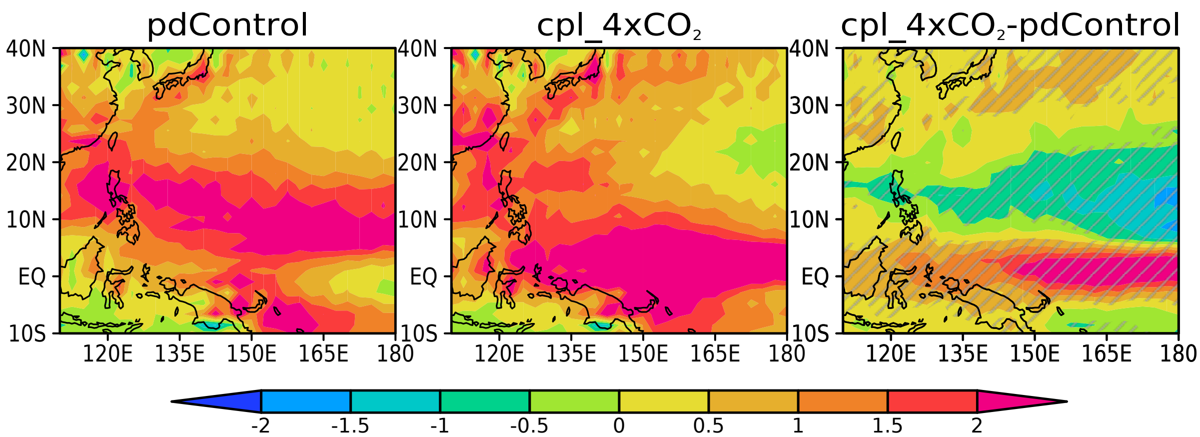

Figure 4.3: MJJA mean vertically averaged diabatic heating (unit: K/day). (a): pdControl, (b): cpl_4$\times$CO$_2$, (c): the difference between cpl_4$\times$CO$_2$ and pdControl. The grey slashes in (c) denote the regions where the diabatic heating exceeds the 95% significance level.

ascending branches: one is located over a broad area from equator to 30°N, and the other one is located around 40°N. The center of maximum meridional moisture transport is located between 10°N and 20°N. In cpl_4$\times$CO$_2$ run, the upward motion is enhanced near equatorial region and midlatitudes, while it is reduced from 10°N to 20°N. Additionally, the meridional moisture transport is amplified between 20°N and 30°N (Fig. 4.4b-c). The changes in meridional circulation and moisture transport is consistent with the changes in precipitation (Fig. 4.2c), i.e., the rainfall is reduced over SCS and enhanced over East China.

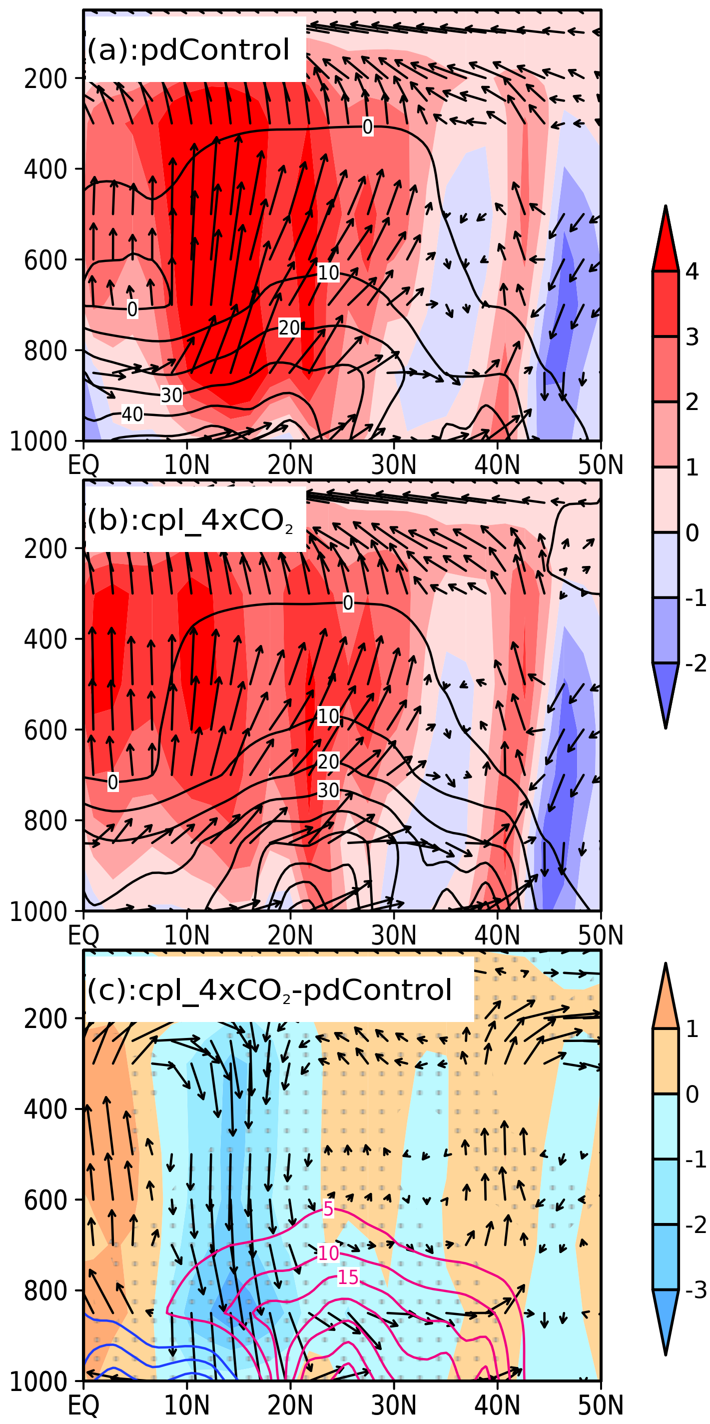

Figure 4.4: MJJA mean zonally averaged (110-120°E) meridional circulation and meridional moisture transport (contours, unit: g/kg×m/s). (a): pdControl, (b): cpl_4×CO_2, (c) the difference between cpl_4×CO_2 and pdControl. Shadings denote the ascending/descending motions. The grey dots in (c) denote the regions where the vertical motion exceeds the 95% significance level.

Therefore, in a future warmer climate, the seasonal mean state of the EASM is enhanced. The warming up of SST results in a diabatic cooling band over the tropical Pacific Ocean (10°N-20°N), and a diabatic warming region over the equatorial Pacific Ocean which is related to the equatorward displaced ITCZ. The change of the diabatic heating in the warming climate leads to a high pressure anomaly and thus an amplified WNPSH. The southwestward extension of the WNPSH enhances the southwesterly flow as well as the moisture transport over East Asia, increasing the monsoonal precipitation. While the diabatic cooling over the tropical WP is consistent with Xiang et al. (2013), the cause of the cooling is different from their study. Xiang et al. (2013) suggest that a cold SST anomaly in the western North Pacific favors the development of descending Rossby waves. The descending waves suppress the development of convection and enhance the wind divergence at the surface, which will continue to suppress the convective activity. In the global warming scenario, the SST is warmer than in the present day conditions in both the equatorial Pacific and the WNP. The WNPSH intensification due to diabatic cooling over tropical WP is also consistent with the findings by Li et al. (2012). However, in their study, they did not show the spatial distribution of the diabatic heating changes in the warming climate.

4.2.2 EASM Interannual Variability

The multivariate EOF analysis (MV-EOF), which is discussed by Wang et al. (2008), is applied to study the variability of the EASM. The domain for the MV-EOF (105°E-140°E, 10°N-50°N) includes both tropical and subtropical East Asia area. The three variables used in MV-EOF are precipitation, zonal and meridional wind at 850 hPa in MJJA (method described in Section 2.3.6).

The first two modes of MV-EOF for pdControl and cpl_4$\times CO_2$ are illustrated in Fig. 4.5. For the pdControl run (Fig. 4.5a), the first mode accounts for 19.45% of the total variance, and the second mode accounts for 10.92% of the total variance. The spatial pattern of the first MV-EOF mode shows a tri-pole structure with a wet anomaly from South China to Japan and two dry anomalies to its south (SCS and subtropical WP) and north (North

China). At 850 hPa, there is an anomalous anti-cyclonic circulation over the area to the south of 35°N, with its center at around (135°E, 25°N). This anti-cyclonic anomaly brings an abnormal southwesterly flow over the region from South China to Japan. The spatial pattern of the second MV-EOF mode shows another tri-pole structure, with enhanced precipitation over the area from 25°N to 40°N, and diminished precipitation to its south and north. At 850 hPa, there are three anomalous circulation systems: a cyclonic anomaly over subtropical East Asia (25°N-40°N), and anti-cyclonic anomalies over SCS and nearby WP, and northern part of EASM domain.

In cpl_4$\times CO_2$ run (Fig. 4.5b), the first mode explains 26.15% of the total variance, and the second mode explains 12.48% of the total variance. The first two modes explain 38.63% of the total variance, which is higher than in pdControl run (30.38% of the total variance). The spatial pattern of the first MV-EOF mode shows a dipole structure, with intensified precipitation over most portion of the East Asia continent, and reduced precipitation over WP. At 850 hPa, there is an anomalous anti-cyclonic circulation over the EASM domain, with southwesterly anomalies prevailing over most part of China, Korean peninsula, and Sea of Japan. The center of this anti-cyclonic anomaly is located at around (128°E, 25°N), which is displaced westward compared to pdControl run. The spatial pattern of the second MV-EOF mode shows a different di-pole structure: positive rainfall anomalies between 25°N and 40°N, and to the north of 45°N; negative rainfall anomalies over South China, SCS, and adjacent WP. At 850 hPa, there are two abnormal circulation structures: cyclonic anomaly between 25°N and 45°N, and anti-cyclonic anomaly to its south.

The PCs of the first two MV-EOF modes for pdControl and cpl_4$\times CO_2$ are also plotted. The comparison of PCs between pdControl and cpl_4$\times CO_2$ indicates that in a warmer climate condition there is larger year-to-year variation in these two modes.

Therefore, in the future warmer climate, there is larger interannual variability of the EASM. The rainfall shows larger variation over the northern part of East Asia due to the changes in the low-level circulation.

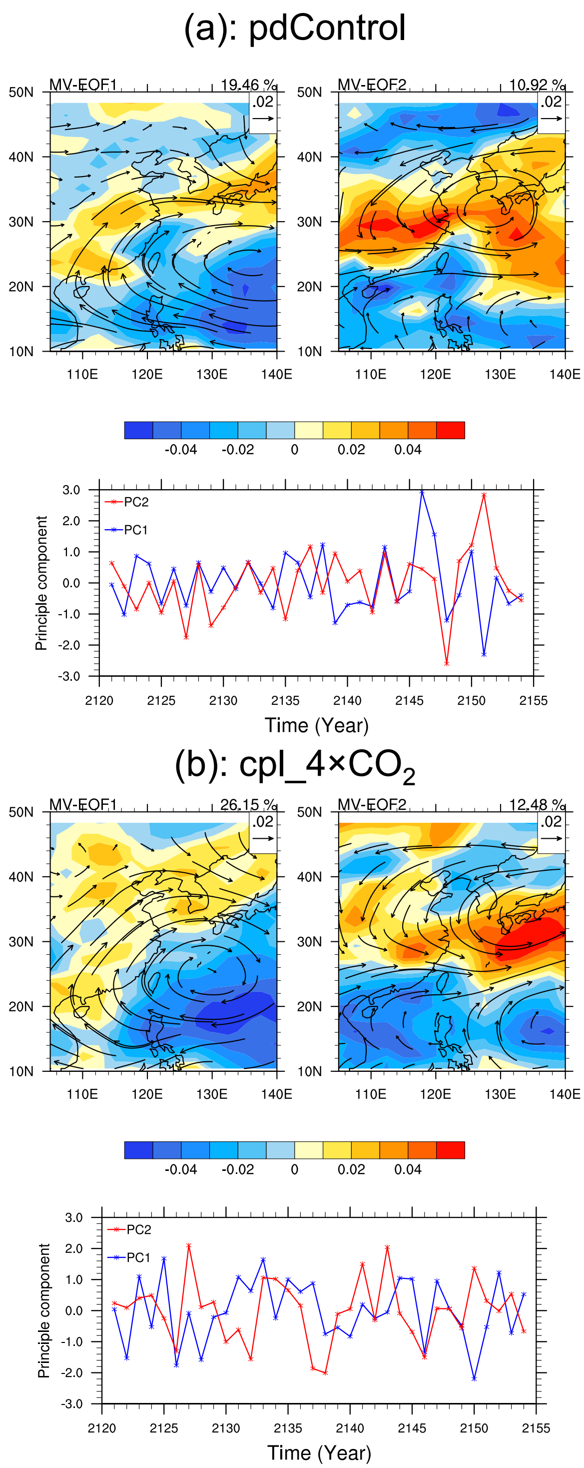

Figure 4.5: Spatial patterns and Principle Components (PC) of multivariate EOF on a set of three variables in MJJA, including precipitation (shadings) and 850-hPa zonal and meridional wind component (vectors). (a): pdControl, (b): cpl_4$\times CO_2$. All the three variables have been normalized before doing the EOF analysis. PCs are also standardized.

4.2.3 Annual Cycle

The annual cycle of the monsoonal precipitation is compared between pdControl and cpl_4×CO_2 runs. It is firstly calculated over the whole EASM domain (Fig. 4.6). In East Asia, the precipitation rate is around 2 mm/day and remains stable from January to March. The precipitation starts to increase from April, and keeps increasing during the following four months. It reaches the peak in July or August, and the maximum value is around 8 mm/day. Afterwards, the precipitation decreases and reaches around 3 mm/day in December. The difference between cpl_4×CO_2 and pdControl during May to August shows that the peak precipitation occurs at different time periods. The peak rainfall in cpl_4×CO_2 occurs in mid-July, while in pdControl the maximum precipitation happens in early August. The magnitude of the peak precipitation in cpl_4×CO_2 is larger than that in pdControl run. The peak precipitation is around 8.5 mm/day in cpl_4×CO_2, and is around 7.5 mm/day in pdControl. Also there is more variability in precipitation in cpl_4×CO_2 run.

The spatial pattern of the annual cycle is computed by zonally averaging precipitation between 110°E and 120°E, and between 120°E and 140°E, respectively. The former shows the meridional propagation of the rainband over SCS and East China, while the latter shows the movement of the rain belt over the subtropical WP, Korean peninsular, and Japan.

In the pdControl run, between 110°E and 120°E (Fig. 4.7a), the large amount of precipitation jumps northward to about 25°N around mid-May, initiating the first standing stage of the EASM. Then the rain belt moves northward in early June and stays between 28°-32°N until mid-June. Afterwards, it jumps northward again and reaches the northernmost position (around 45°N) in mid-July. In the cpl_4×CO_2 simulation (Fig. 4.7b), the mergence of tropical and subtropical rain belts is about 5 days later, and the precipitation is largely enhanced between 20°N and 30°N. The Mei-yu onset is not as clear as in the pdControl run. Additionally, the precipitation at 30°N lasts until early July, which means that the Mei-yu season lasts longer in a warmer climate. In the beginning of July, the rain belt advances northward again. The precipitation keeps staying around 37°N-43°N and lasts from July to the end of August. This longer duration of the enhanced precipitation over northern China

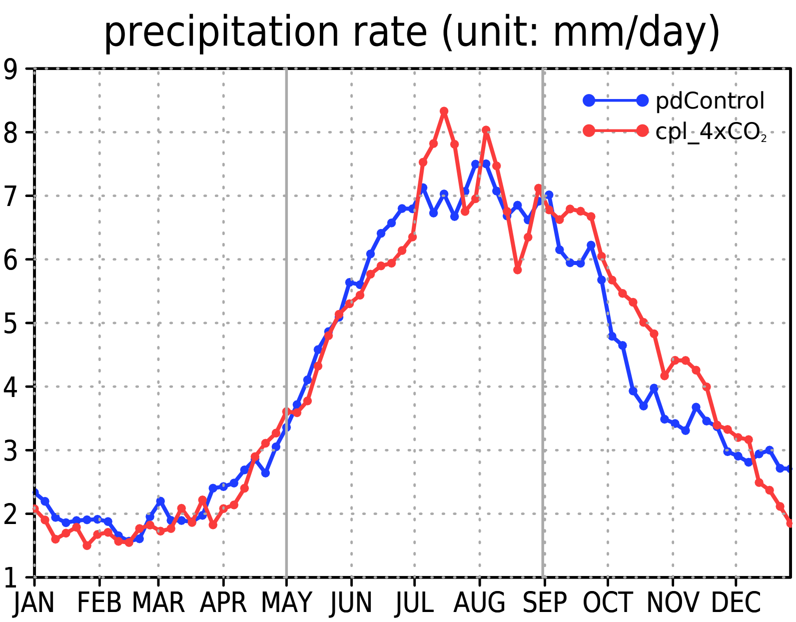

Figure 4.6: the area average of precipitation over the EASM area (105-140°E, 10-45°N) using climatological pentad mean data. Blue line denotes the precipitation rate of pdControl, red line denotes the precipitation rate of cpl_4×CO_2. They grey lines denotes the time period May to August.

is clearly illustrated in the difference between cpl_4×CO_2 and pdControl (Fig. 4.7c).

The difference in the annual cycle of the precipitation shows the similar pattern over the region 120°E-140°E (Fig. 4.7d-f). In the pdControl run (Fig. 4.7d), the subtropical rain band shows the first northward jump (from 30° to 32°N-38°N) at the beginning of June, and lasts until around 20 June. Afterwards, it jumps northward again. In the cpl_4×CO_2, the precipitation is enhanced along the northward movement of the rain belt (Fig. 4.7e-f). The precipitation is intensified over 25°N-30°N during May to mid-June. The first northward jump of the rain belt in June is delayed. It jumps northward around mid-June, and stays over 30°N-40°N until the beginning of July. This rainy episode (Baiu in Japan and Changma in Korean) persists longer in the global warming scenario, plus the precipitation is largely intensified (Fig. 4.7f). Then the rain belt moves northward around 10 July, but cannot reach as high a latitude as in the pdControl run.

The annual cycle of the WNPSH index (description in Section. 2.3.3) is also plotted in Fig. 4.7. Generally, it indicates the meridional migration of subtropical ridge. In the pdControl run (Fig. 4.7a), the annual cycle of the WNPSH shows the first northward jump in late May and the second northward movement in late June. It persists between 38°N and 42°N during July and August. In the cpl_4×CO_2 run (Fig. 4.7b), the ridge line remains at around 28°N until late June when it shows the first northward jump. Then it jumps again around 10 July. However, it cannot reach as high a latitude as in the pdControl run. Compared with the pdControl run, the WNPSH is displaced southward throughout the whole summer, especially from June to August (Fig. 4.7c). This southward shift of the WNPSH favors the enhanced and longer persistence of Mei-yu (Baiu and Changma) rainfall as well as the precipitation over northern East Asia.

The WNPSH index in Fig. 4.7 only shows the movement of the WNPSH in the meridional direction. The zonal shift of the WNPSH, which is also important in determining the moisture transport to East Asia, is masked by the above WNPSH index. Therefore, it is necessary to use a parameter to express the trajectory of the WNPSH in both zonal and meridional directions. The calculation of the WNPSH trajectory is described in detail

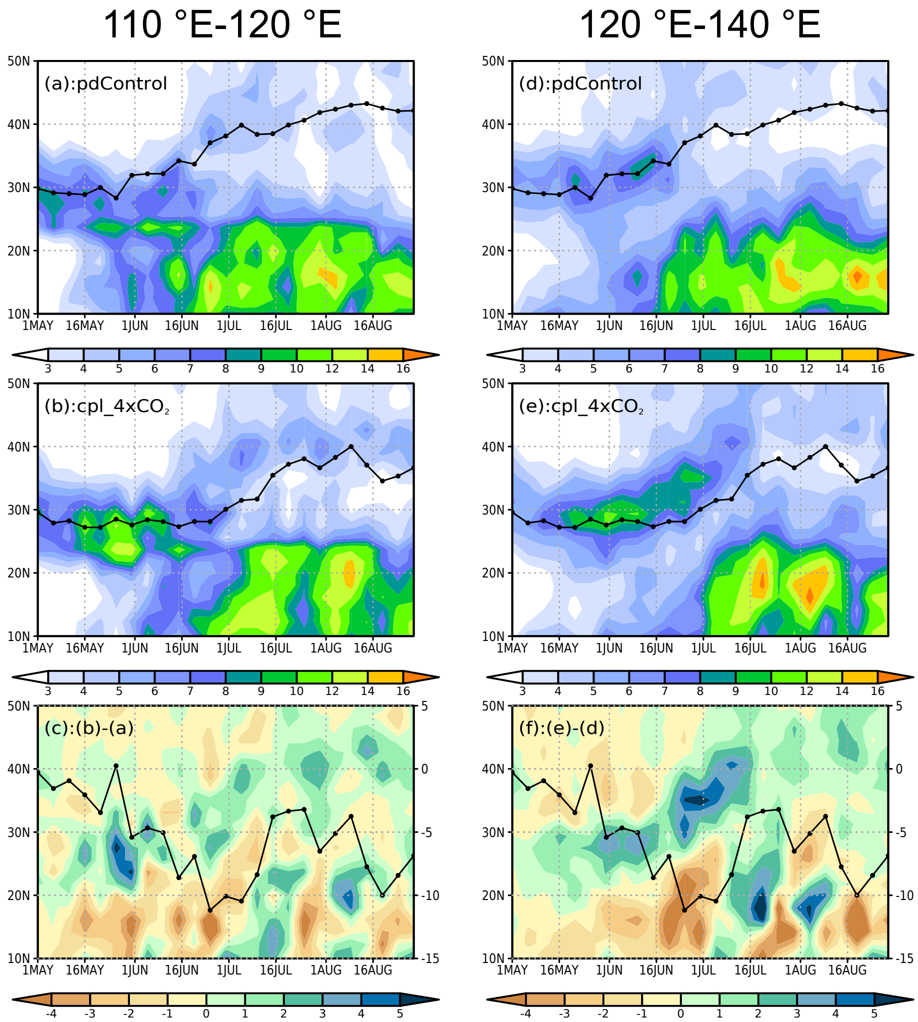

Figure 4.7: Zonal mean of precipitation rate (shadings) and WNPSH index (black line) in the coupled runs. (a)-(c) zonal mean between 110-120°E, (d)-(f) zonal mean between 120-140°E. (a) and (d) pdControl, (b) and (e) cpl_4×CO_2, (c) and (f) difference between coupled runs, cpl_4×CO_2 minus pdControl. The y axis on the right side in (c) and (f) denotes the difference of the WNPSH index.

in subsection 2.3.4. Generally, it is the position of the intersection point of subtropical ridge and 1540-m isoline. The trajectories of the WNPSH in pdControl and cpl_4×CO_2 are shown in Fig. 4.8. The most prominent difference between these two simulations is that, in cpl_4×CO_2, the WNPSH is displaced southwestward, which is also shown in MJJA mean state (Fig. 4.1). Moreover, the WNPSH spans a different range in zonal and meridional directions. In the pdControl run, the WNPSH moves from 25°N in early May to 40°N in late August, spaning 15 degrees in latitude. However, in cpl_4×CO_2, the WNPSH moves from 19°N to around 31°N, the northernmost position, spanning around 12 degrees in latitude. Additionally, the WNPSH in cpl_4×CO_2 spans a broader range in zonal direction. It spreads 37 degrees in cpl_4×CO_2, while 18 degrees in pdControl.

One can also see the difference in the WNPSH advancement between pdControl and cpl_4×CO_2. In May, the WNPSH in pdControl shows an obvious northward as well as eastward movement, while, in cpl_4×CO_2, the WNPSH shifts in the zonal direction but does not have a big jump in the meridional direction. In June, the WNPSH in both pdControl and cpl_4×CO_2 shows a northward jump, and keeps moving northward in July. However, along with the northward propagation, in pdControl, the WNPSH shifts eastward in June and westward in July. However, in cpl_4×CO_2, the WNPSH moves westward in June and eastward in July. In August, the WNPSH remains at the same latitude in pdControl, while it moves southward and westward in cpl_4×CO_2.

Therefore, the annual cycle of the EASM is changed in the global warming scenario. There is a longer persistence of the Mei-yu season in East China, as well as the Baiu in Japan, and Changma in Korean (Fig. 4.7). This result is consistent with the conclusion in previous studies (e.g., Kitoh and Uchiyama, 2006; Kusunoki and Arakawa, 2012). In addition, the precipitation is intensified along the northward movement of the subtropical rain belt. The changes in the annual cycle of the precipitation are related to the changes in the WNPSH migration. In the warmer climate, the WNPSH is displaced southward throughout the whole summer (Fig. 4.7c and f). The longer persistence of the subtropical ridge at a lower latitude during May and June influences the Mei-yu/Baiu/Changma rainy

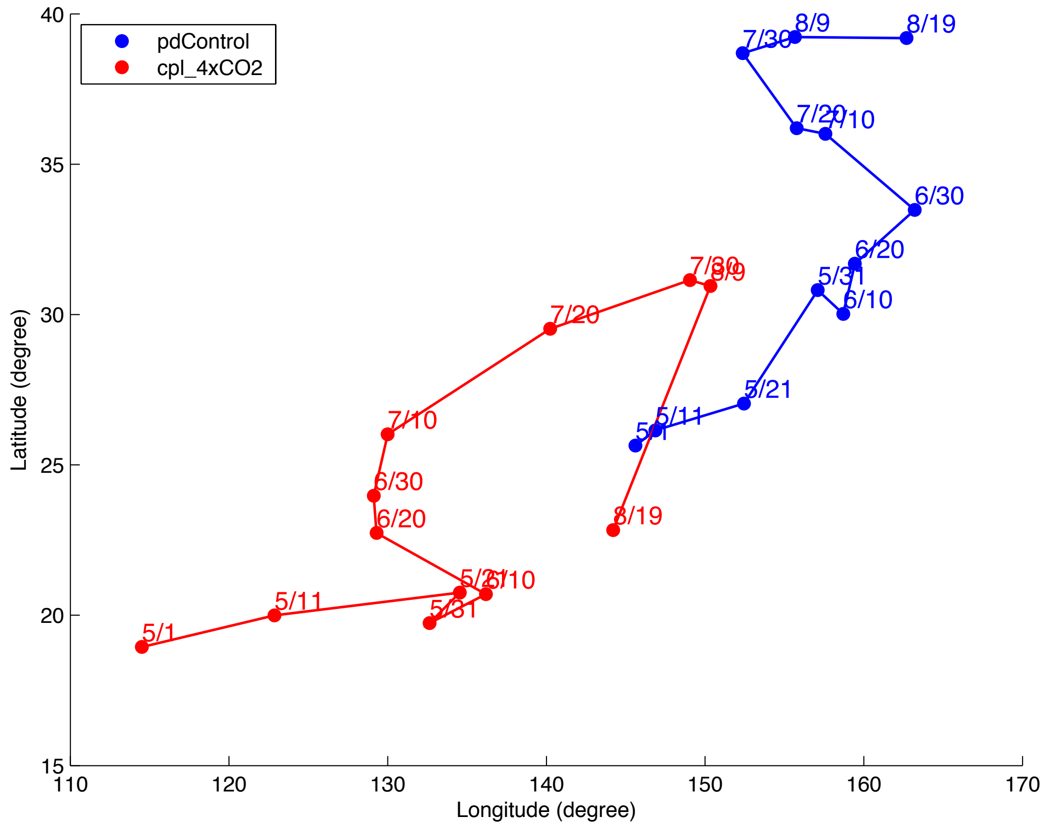

Figure 4.8: Trajectory of WNPSH position. The WNPSH position is based on the intersection point of subtropical ridge and 1540m isoline. Blue line denotes pdControl run. Red dot line denotes cpl_4$\times$$CO_2$ run. The text above each dot represents the date.

season, including the magnitude of the precipitation, the onset and time period. The southward displacement of the WNPSH in July and August favors the formation of enhanced precipitation over northern East Asia. In the warmer climate, the movement of the WNPSH shows difference behaviors in both meridional and longitudinal directions (Fig. 4.8).

4.2.4 ISV

The ISV of the EASM in a warmer climate is analyzed using the same method as in Chapter 3 (method described in Section 2.3.5). Both the 30-60-day mode and 10-20-day mode are computed for pdControl and cpl_4×CO_2 simulations.

4.2.4.1 30-60-day Mode

The variance of 30-60-day band filtered OLR during MJJ is shown in Fig. 4.9. In the pdControl run, the OLR reaches maximum over SCS and adjacent WNP, with magnitude around 450 W^2/m^4 (Fig. 4.9a). In cpl_4×CO_2, the maximum OLR variance is still located at SCS and nearby WNP, but its magnitude is decreased to around 350 W^2/m^4 (Fig. 4.9b). The composite of 30-60-day oscillation is based on an OLR index, which is the area average of the 30-60-day band filtered OLR over the black box (112.5°E-130°E, 12°N-22.5°N). This area is kept the same in the OLR index calculation for pdControl and cpl_4×CO_2. Day 0 of the cycle is centered on the day when the OLR index during MJJ is less than minus one standard deviation (-15.43 W/m^2 in pdControl) over SCS. The life cycle of an EASM event consists of 12 phases starting from 15 days before and proceeding 40 days after Day 0. In pdControl we identified 43 events from 2125 to 2154, whereas in cpl_4×CO_2 there are 38 events during the same time period. The statistical significance of the composite is assessed using the Student's t test.

Figure 4.10 shows the life cycle of 30-60-day oscillation in OLR and 850-hPa wind in pdControl and cpl_4×CO_2. The life cycle in pdControl has been described in detail in Chapter 3. Compared with the pdControl run, the 30-60-day oscillation in cpl_4×CO_2 becomes weaker (Fig. 4.10b), which can be seen from the smaller magnitude of OLR and wind

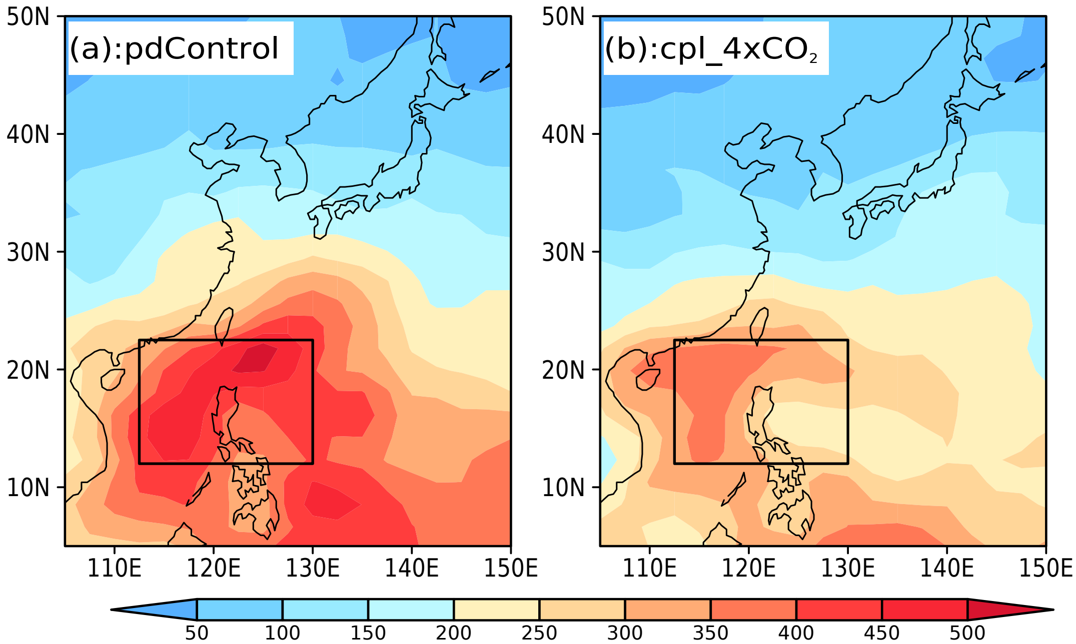

Figure 4.9: The variance of 30-60-day bandfiltered OLR daily anomaly during MJJ (unit: W^2m^{-4}). (a) pdControl. (b) cpl_4×CO_2. The black box (112.5-130°E, 12-22.5°N) is the region where the OLR variance reaches maximum in the observations.

anomalies. Generally the pattern of the life cycle does not show much difference between pdControl cpl_4×CO_2. Both simulations show the northwestward propagation of the active and suppressed convection, and the corresponding circulation system to the northwest of the convection center, i.e., a cyclonic (anti-cyclonic) anomaly to the northwestern side of the active (suppressed) convection center.

From day −15 to day −5, both simulations show that the suppressed convection over SCS dissipates, and the active convection from WPWP propagates northwestward into SCS. The convective activity in cpl_4×CO_2 is relatively weaker than that in pdControl, along with a weaker cyclonic anomaly to its northwest (e.g. at day −10). Also, the convection does not extend as far eastward as in the pdControl.

At day 0 when the convection reaches the peak over SCS, there are dry regions to its south (over WPWP) and north (East Asia). Both the suppressed convections in cpl_4×CO_2

are not as strong as in the pdControl run. Afterwards, the suppressed convection over WPWP develops and moves northwestward. In the pdControl run, at day 15, the convection over SCS moves northward into Southeast China. In the meantime, the northeasterly anomaly at 30°N turns into southwesterly anomaly, initiating the Mei-yu season. The Mei-yu season lasts until about day 25, and from day 30 the suppressed convection moves from WPWP into Southeast China. In cpl_4×CO_2, the Mei-yu season starts around day 20 when there is active convection and southwesterly anomaly over Southeast China. The active convection over Southeast China lasts until day 35. However, the wind anomaly is weaker and below the significance level after day 30.

The northward propagation of the active and break precipitation phases of the EASM can be seen more clearly from the zonally averaged OLR and 850-hPa wind between 110°E-120°E (Fig. 4.11). In the cpl_4×CO_2 run, the suppressed convection around 30°N prevents the convection moving northward, while, in the pdControl run, the suppressed convection dissipates quickly and favors the convection over SCS moving into East China. In addition, in cpl_4×CO_2, the convection over East China lasts until day 35, while, in pdControl, it disappears after day 25.

The zonal propagation of the 30-60-day oscillation is also compared between cpl_4×CO_2 and pdControl by computing the meridional averaged OLR and 850-hPa wind between 5°N and 20°N (Fig. 4.12). In the pdControl there is an eastward propagation to the west of 90°E and to the east of 150°E, and a westward propagation between 130°E and 150°E, while, in cpl_4×CO_2, these zonal propagations are weaker. In both simulations, the zonal propagation is not obvious for the 30-60-day oscillation over the region between 90°E and 130°E.

Therefore, over the EASM area, the 30-60-day mode is dominated by the northward and westward propagation. Generally the 30-60-day mode does not show a big difference in a future warmer climate, except a longer duration of the Mei-yu season over Southeast China.

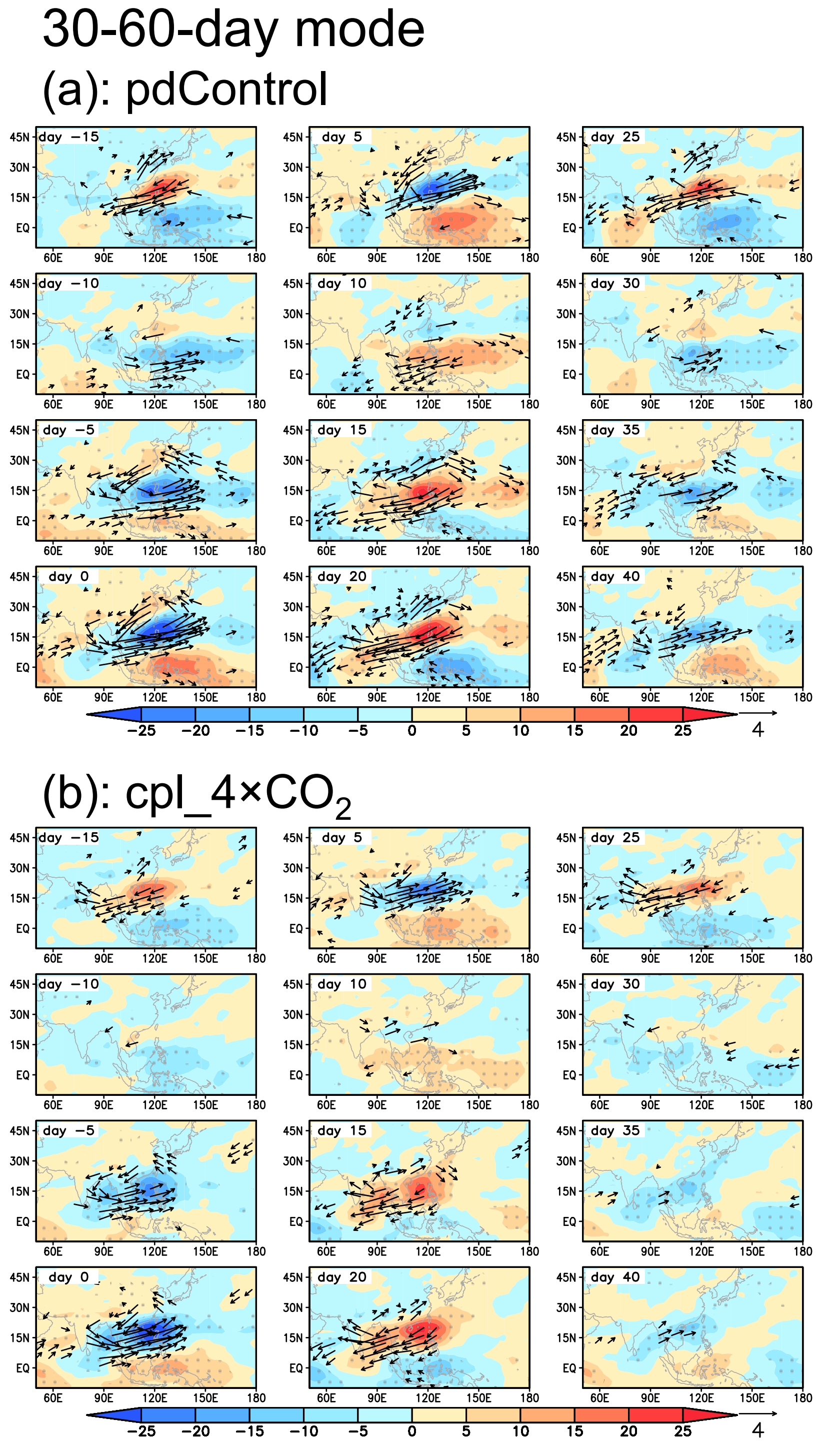

Figure 4.10: The 30-60-day mode composite of OLR (shading, unit: Wm^{-2}) and 850-hPa wind (vectors, unit: ms^{-1}) of the 12 ISO EASM phases: (a) pdControl. (b) cpl_4$\times CO_2$. The areas above the 95% significance level are highlighted by grey dots.

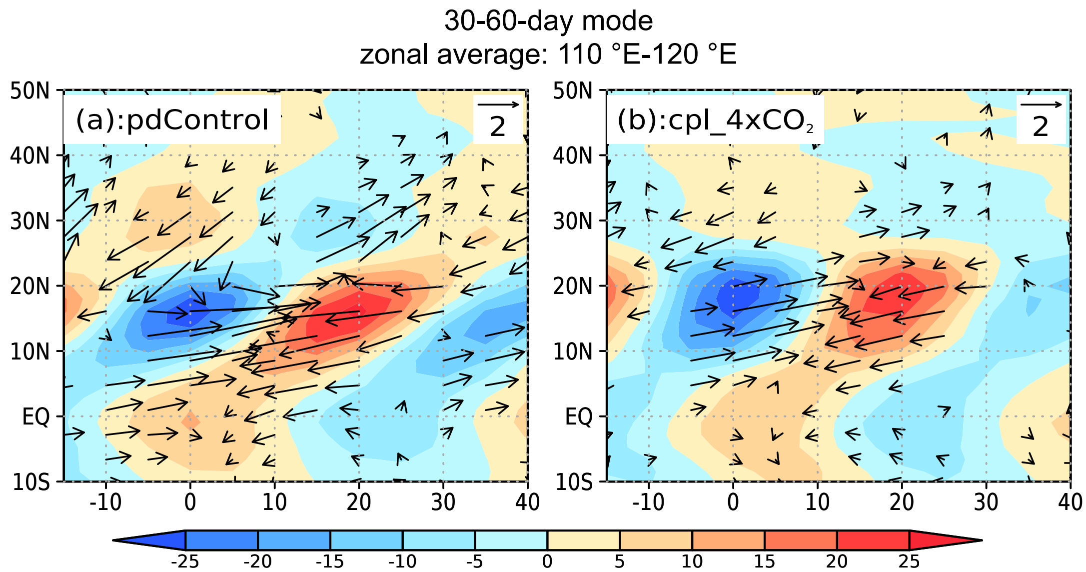

Figure 4.11: The zonally averaged (110°E-120°E) 12 phases of the 30-60-day ISO EASM in OLR (shading, unit: Wm^{-2}) and 850-hPa wind (vectors, unit: ms^{-1}) for (a) pdControl, (b) cpl_4×CO_2. The wind which is smaller than $0.1ms^{-1}$ is masked out.

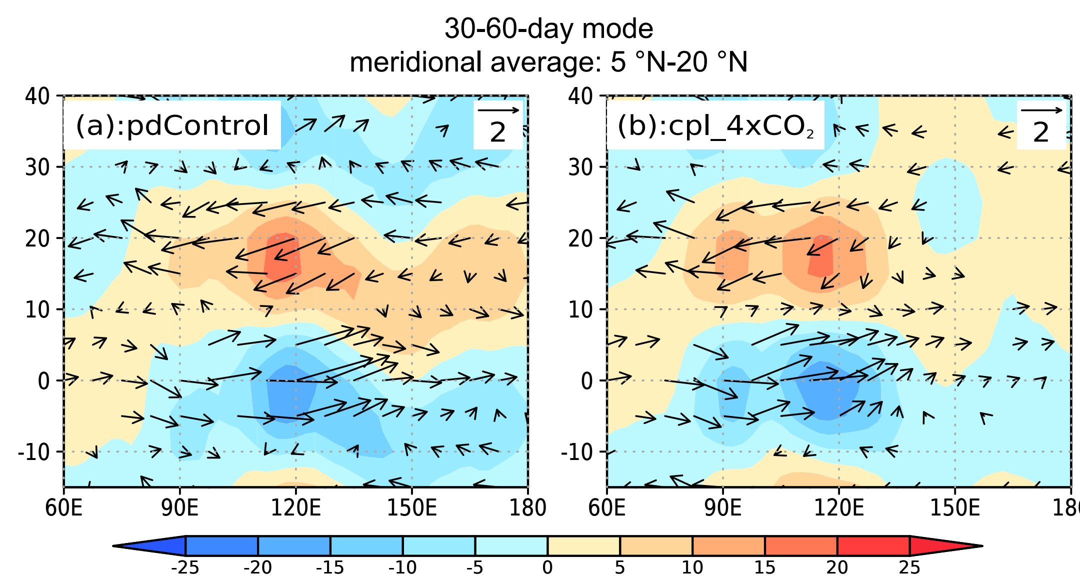

Figure 4.12: The meridionally averaged (5°N-20°N) 12 phases of the 30-60-day ISO EASM in OLR (shading, unit: Wm^{-2}) and 850-hPa wind (vectors, unit: ms^{-1}) for (a) dry pdControl, (b) cpl_4×CO_2. The wind which is smaller than $0.1ms^{-1}$ is masked out.

4.2.4.2 10-20-day Mode

The intraseasonal oscillation on the 10-20-day time scale is analyzed for pdControl and cpl_4×CO_2. The variance of the 10-20-day band filtered OLR during MJJ is computed (Fig. 4.13). In the pdControl run, the OLR reaches maximum over SCS and adjacent WNP, with magnitude around 600 W^2/m^4 (Fig. 4.13a). In cpl_4×CO_2, the maximum OLR variance is located over SCS with a smaller magnitude (Fig. 4.13b). The black box (110°E-140°E, 10°N-25°N) encloses the area in which the OLR index for the 10-20-day mode is calculated. Day 0 of the cycle is centered on the day when the OLR index during MJJ is less than minus one and a half standard deviation (-14.14 W/m^2 in pdControl) over SCS. The life cycle of an EASM event consists of 12 phases starting from 10 days before and proceeding 12 days after Day 0. In pdControl, we identified 62 events from 2125 to 2154, whereas in cpl_4×CO_2 there are 71 events during the same time period. The statistical significance of the composite is assessed using the Student's t test.

The life cycle of the 10-20-day mode is similar in pdControl and cpl_4×CO_2 (Fig. 4.14). From day -10 to day -4, the suppressed convection moves from tropical WP into SCS. Meanwhile, an active convection starts developing to the south of this suppressed convection. The active convection strengthens at day -2. It moves to SCS and nearby WNP, and reaches the maximum at day 0. At day 0, the active convection starts dissipating and another suppressed convection starts developing to its south. Afterwards, it repeats almost the same cycle during day -4 to day -2.

To make the meridional propagation more clear, zonal average (110°E-120°E) of the 10-20-day mode is computed (Fig. 4.15). Rather than the obvious northward propagation shown in the 30-60-day mode (Fig. 4.11), the 10-20-day mode shows a southward propagation of the convective activity over East China. The zonal migration of the 10-20-day model is compared by calculating the meridional average between 5°N and 20°N (Fig. 4.16). In both pdControl and cpl_4×CO_2 the 10-20-day mode shows a westward migration of active/suppressed convection. In cpl_4×CO_2, the magnitude of the convection and wind is

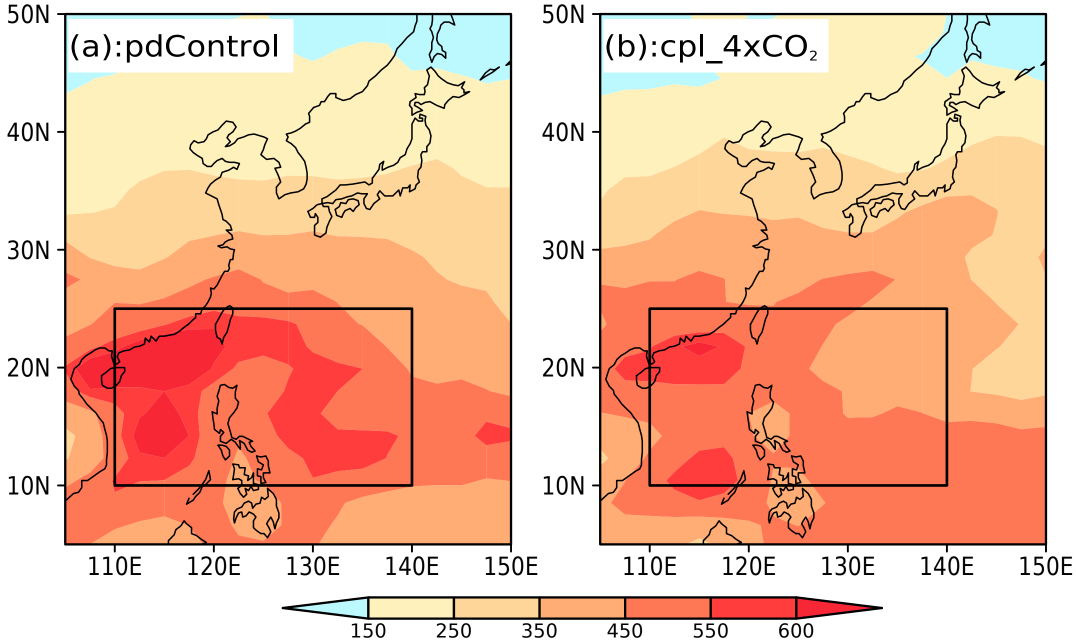

Figure 4.13: The variance of 10-20-day bandfiltered OLR daily anomaly during MJJ (unit: W^2m^{-4}). (a) pdControl. (b) cpl_4×CO_2. The black box (110-140°E, 10-25°N) is the region where the OLR variance reaches maximum in the observations.

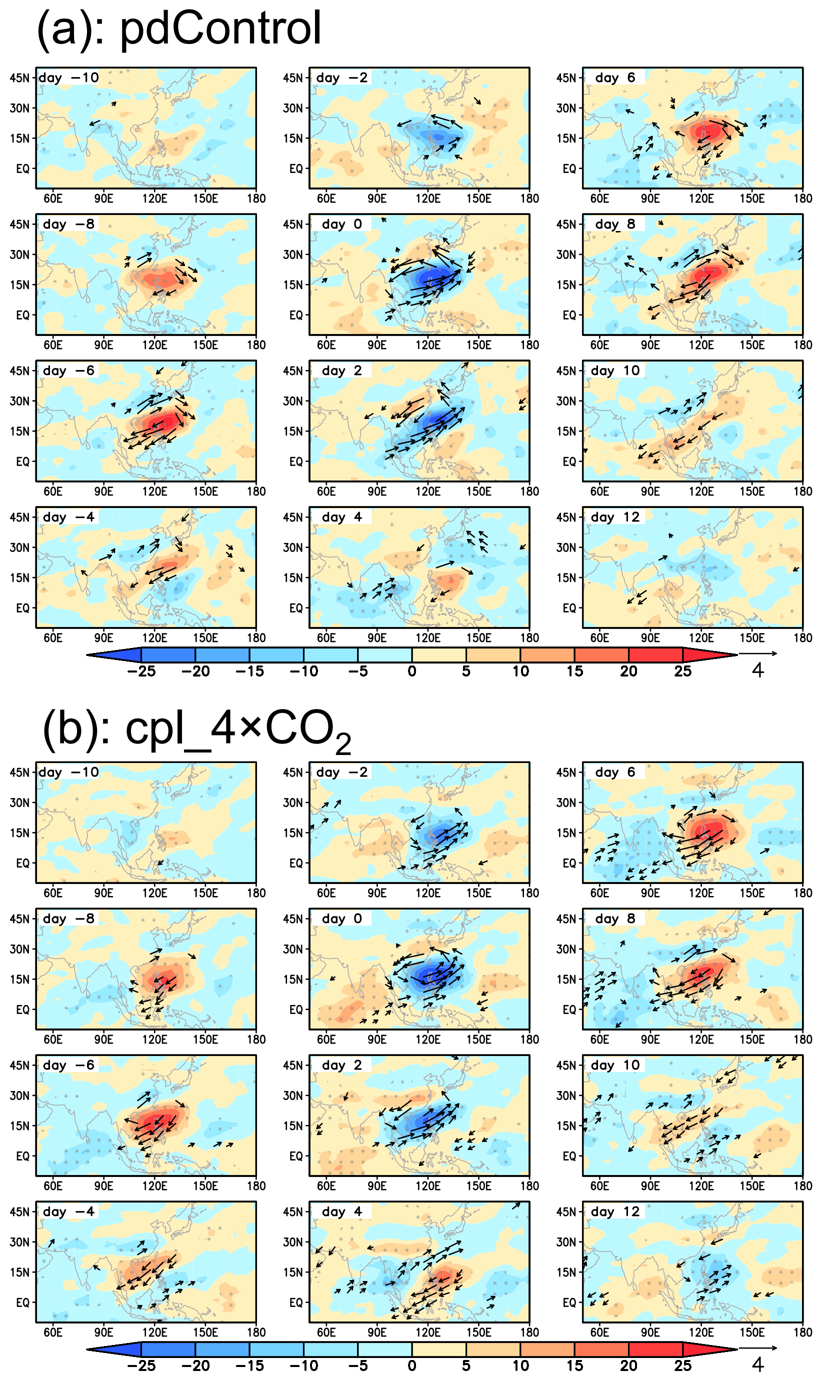

Figure 4.14: Same as Fig. 4.10, except for the 10-20-day mode. The life cycle is from day -10 to day 12.

slightly intensified compared to pdControl.

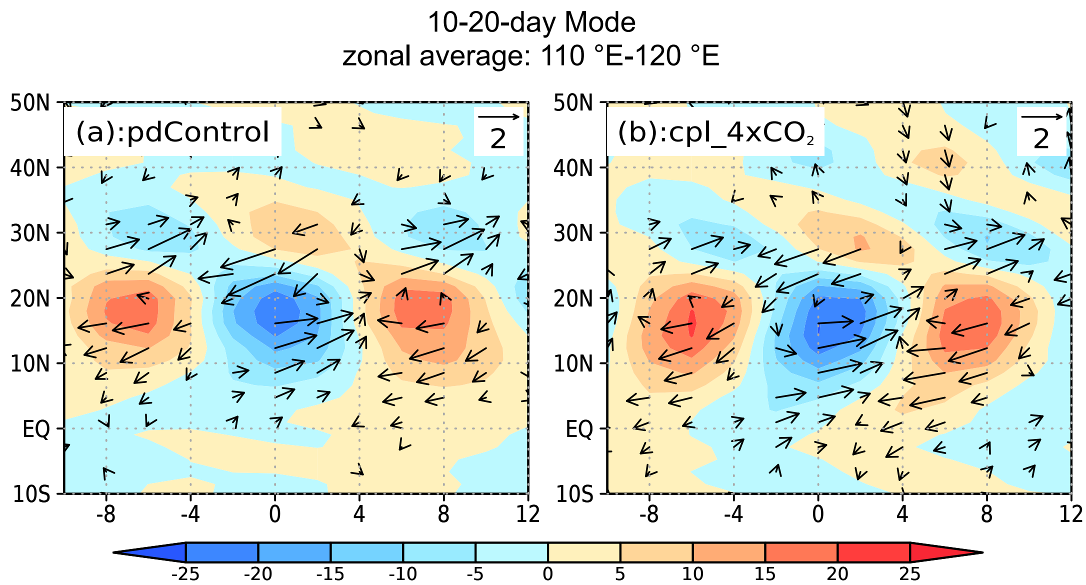

Figure 4.15: Same as Fig. 4.11, except for the 10-20-day mode.

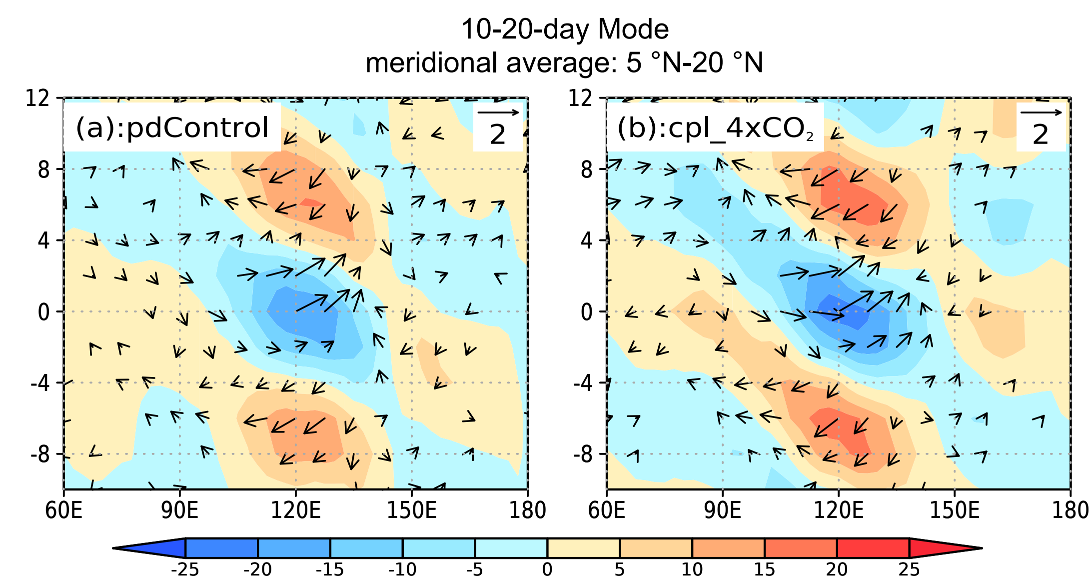

Figure 4.16: Same as Fig. 4.12, except for the 10-20-day mode.

The 10-20-day mode contains eastward propagation over subtropics and southward propagation over East China. In a warmer climate, the 10-20-day mode is intensified. However, the pattern of the life cycle does not change much.

4.3 A Proposed Mechanism

According to above analysis, the changes of EASM under the global warming scenario indicate that the mean state of the EASM is intensified, including an increased precipitation and stronger monsoon circulation. This result is consistent with other numerical studies (Kripalani et al., 2007; Lee and Wang, 2014; Seo et al., 2013). In addition, the annual cycle of the EASM shows that the precipitation over northern part of EASM domain persists longer. The variations in the seasonal mean state of the EASM are related to a strengthening and westward extension of the WNPSH. In this section, a mechanism is proposed to address why the EASM shows such changes under the global warming scenario.

As presented in Chapter 1, the mechanisms associated with EASM can be associated with the internal dynamics of the atmosphere and with atmospheric changes forced by surface processes. The response of the climate system to an external forcing can also be divided into a rapid response, in which the atmospheric processes respond to the forcing, and a longer time scale response due to ocean-atmosphere feedbacks (Bretherton et al., 2014). To understand the response of EASM to global warming, it is useful to examine the EASM changes with respect to the rapid warming of the atmosphere and to the SST warming. Therefore, EASM will be analyzed in the numerical simulations described in Section 4.1.

As pointed out by previous studies (e.g., Lu and Dong, 2001; Mao et al., 2010; Zhang et al., 2009), the position and strength of the WNPSH has a large impact on the EASM, and thus the mechanisms responsible for the WNPSH changes in the warming climate are crucial to understand the variations in the EASM. The MJJA means of precipitation and 850-hPa GPH are computed for three simulations: cpl_4$\times$$CO_2$, amip_4$\times$$CO_2$, and amip_4K (Fig. 4.17). In the two AMIP-type runs (Fig. 4.17b and c), the air-sea interaction is cut off. Only the atmosphere can respond to ocean. Both amip_4$\times$$CO_2$ and amip_4K runs exhibit

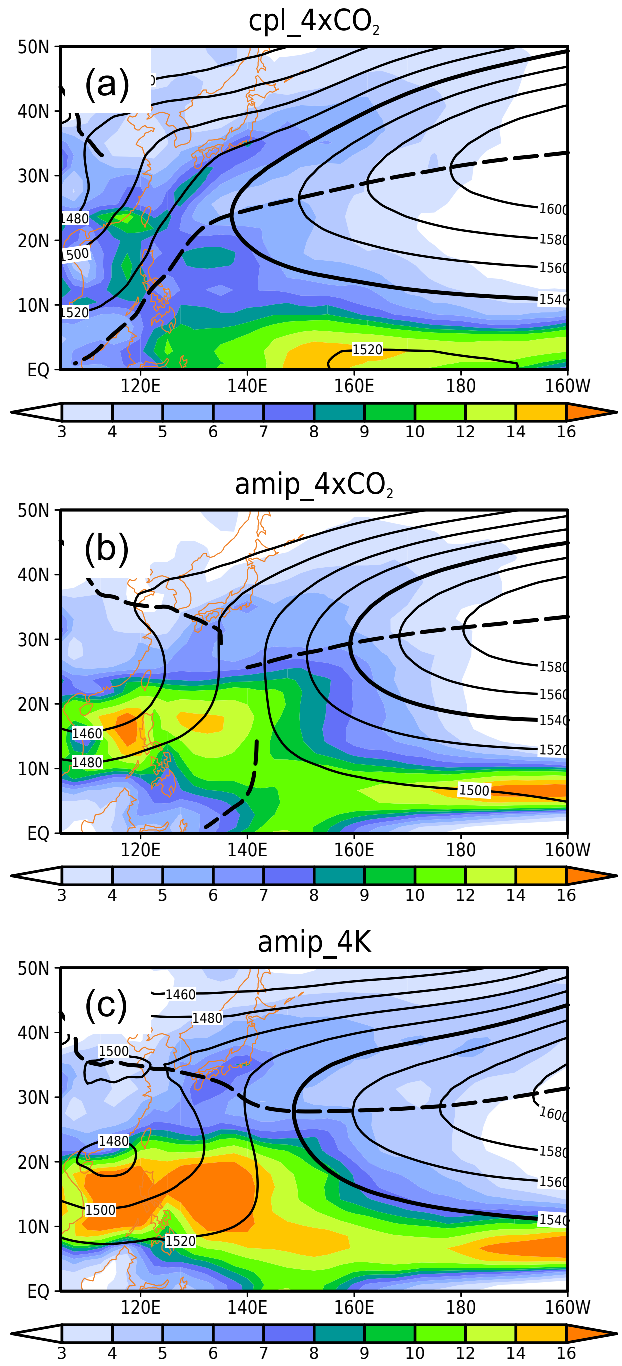

Figure 4.17: The MJJA mean precipitation (shadings, unit: mm/day) and 850-hPa GPH (contours, unit: m). The thick contours denote the isoline of 1540m, and the dashed lines denotes the subtropical ridge. (a): cpl_4×CO_2, (b): amip_4×CO_2, (c): amip_4K

the enhanced precipitation extending from SCS to WNP (Fig. 4.17b and c), which is related to the lack of air-sea interaction in these two simulations. In amip_4$\times$$CO_2$ (Fig. 4.17b), which shows the response of EASM to the rapid atmospheric warming, the WNPSH is displaced eastward compared with that in the cpl_4$\times$$CO_2$ (Fig. 4.17a). In amip_4$\times$$CO_2$ (Fig. 4.17b), the western edge of the 1540-m isoline is located around 160°E, whereas, in cpl_4$\times$$CO_2$ (Fig. 4.17a), the western edge of the 1540-m isoline reaches 140°E. This implies that the enhanced precipitation over SCS and nearby WP due to the lack of air-sea interaction prevents the WNPSH from extending westward. The amip_4K (Fig. 4.17c) shows the EASM response to the SST warming, and the precipitation over SCS and nearby WP in this simulation is more intense than that in the amip_4$\times$$CO_2$. However, the WNPSH does retreat eastward as expected. The western edge of the 1540-m isoline extends to around 150°E, which is displaced 10 degrees westward compared to amip_4$\times$$CO_2$ (Fig. 4.17b). This indicates that the warming of boundary conditions plays a more important role in the changes of EASM mean state under the warming scenario than the atmospheric warming due to external forcing

Therefore, the changes of the WNPSH in the warming climate is influenced by two factors, warming of boundary conditions, and the convection over SCS and adjacent WP due to the lack of air-sea interaction. The warming of boundary conditions favors the intensification and the resultant westward expansion of the WNPSH, whereas the convection over SCS and WP prevents the WNPSH from extending westward. The EASM response to these two factors are tested by numerical experiments, which will be discussed in Chapter 5.

4.4 Conclusion

In conclusion, the mean state of the EASM is intensified under the global warming scenario. The precipitation is enhanced and the monsoon circulation is amplified. The annual cycle of the EASM is also changed in the warming climate. For instance, the monsoon onset is delayed for about 5 days, the Mei-yu/Baiu/Changma lasts longer, as well as the rainy episode over the northern East Asian. The changes of the EASM in a warmer climate simulated by SP-CCSM4 is in agreement with other model simulations (e.g., Kitoh and Uchiyama, 2006; Kripalani et al., 2007; Lee and Wang, 2014; Sun and Ding, 2010). In addition, the interannual variability of the EASM varies in the warming climate. There is more precipitation in the northern part of East Asia, and the year-to-year variability is amplified. However, the intraseasonal variability of the EASM does not show a big difference in the warming climate.

The variations in the mean state and annual cycle of the EASM are related to the changes in WNPSH. The warming up of SST leads to a diabatic cooling area over tropical Pacific Ocean and diabatic warming band along the equator. The pattern of the changes in the diabatic heating leads to a high pressure anomaly over the WNP, which intensifies the WNPSH. The amplification and the southwestward extension of the WNPSH enhances the southwesterly flow and the resultant moisture transport over East Asia, increasing the EASM precipitation.

A hypothesis is proposed to explain the future changes of the EASM based on the analysis of its mean state under various global warming scenarios. Since the EASM precipitation is tightly associated with the WNPSH, the mechanism responsible for the changes in the WNPSH explains the EASM variation in the warmer climate. The changes of the WNPSH are affected by two factors, one is the warming SST and the other is the convection over tropical SCS and nearby WP. The warming SST favors the amplification of the WNPSH, whereas the strong convection due to the lack of air-sea interaction prevents the WNPSH from extending westward.

Chapter 5: Sensitivity Experiments to Test Air–Sea Interaction Mechanism

In Chapter 4, the changes in the EASM under various global warming scenarios were analyzed using SP-CCM4. Then a local air-sea interaction mechanism was proposed to explain such changes. This chapter aims to test the proposed mechanism by designing two numerical experiments. The first experiment tests how the ocean mean state influences the atmosphere. The second one intends to prove that the suppressed convective activity over SCS and adjacent WP favors the westward extension of the WNPSH. In this chapter, we will describe how these two model experiments are designed, and analyze the results of two experiments.

5.1 Model Experiments

The changes in the WNPSH under the global warming scenario are affected by two factors: the warming of the boundary conditions, and the enhanced convective activity over tropical SCS and nearby WP due to the lack of air-sea interaction. The former favors the amplification of the WNPSH, whereas the latter prevents the WNPSH from extending westward.

This hypothesis can be tested by an intervention in the numerical model designed to alter the air-sea interaction only over the region of interest. Because the mean SST used to construct the boundary conditions of the amip_4K experiment is not consistent with the mean state of the coupled run, the experiment was done in two steps: 1) The SSTs from the cpl_4$\times$$CO_2$ simulation are used as boundary conditions in an AMIP-type experiment, amip_4$\times$$CO_2$sst run, in which the atmospheric CO_2 concentration is the same as in the pdControl simulation. The SST is taken from the last 30 years of the cpl_4$\times$$CO_2$ when the atmospheric warming in the coupled model is mostly in response to the surface warming. 2) The amip_4×CO_2_lhflx simulation which uses the same configuration as the amip_4×CO_2sst run, except that the surface evaporation is altered over a small region over SCS and WP to restore the surface evaporation to the levels of the cpl_4×CO_2 simulation.

The first experiment (amip_4×CO_2sst) tests how the ocean mean state influences the atmosphere. Because in the amip_4K run the SST is from observations, which cannot be compared to the the coupled runs (SST is generated by ocean model). In the amip_4×CO_2sst, the SST is that of the cpl_4×CO_2 run and the atmospheric CO_2 concentration is the same as in the pdControl run. In this experiment, the atmosphere can respond to the ocean while the SST is prescribed. If the atmospheric CO_2 is quadrupled the atmospheric response should be the same as in cpl_4×CO_2.

The second experiment (amip_4×CO_2sst_lhflx) is a sensitivity-type experiment, in which the surface latent heat flux is changed over SCS and nearby WP. It has the same SST and CO_2 level as the amip_4×CO_2sst, except that the latent heat flux (LHFLX) is reduced by 10W/m^2 over the region (105°E-140°E, 5°S-12.5°N) (details below). This experiment aims to prove that the convective activity over tropical SCS and adjacent WP affects the westward extension of the WNPSH. The SST difference among ocean basins is not artificially enlarged by adding or subtracting SST anomalies over a particular ocean domain as in previous studies (Wang et al., 2013; Xiang et al., 2013; Zhou et al., 2009). Therefore, the difference of the WNPSH between these two experiments is due to the convection variation over SCS and WP, and the resultant changes of general circulation.

The magnitude and the domain of the LHFLX changes in amip_4×CO_2sst_lhflx is based on the difference between amip_4×CO_2sst and cpl_4×CO_2. Figure 5.1a shows the variance of the MJJA mean precipitation difference between cpl_4×CO_2 and amip_4×CO_2sst. The maximum variance appears over tropical SCS and WP. Then an index of precipitation is defined as an area average of the rainfall difference between cpl_4×CO_2 and amip_4×CO_2sst over the area (115°E-135°E, 12.5°N-20°N). In order to determine the region where LHFLX should be changed in amip_4×CO_2sst_lhflx, the correlation between the rainfall index and

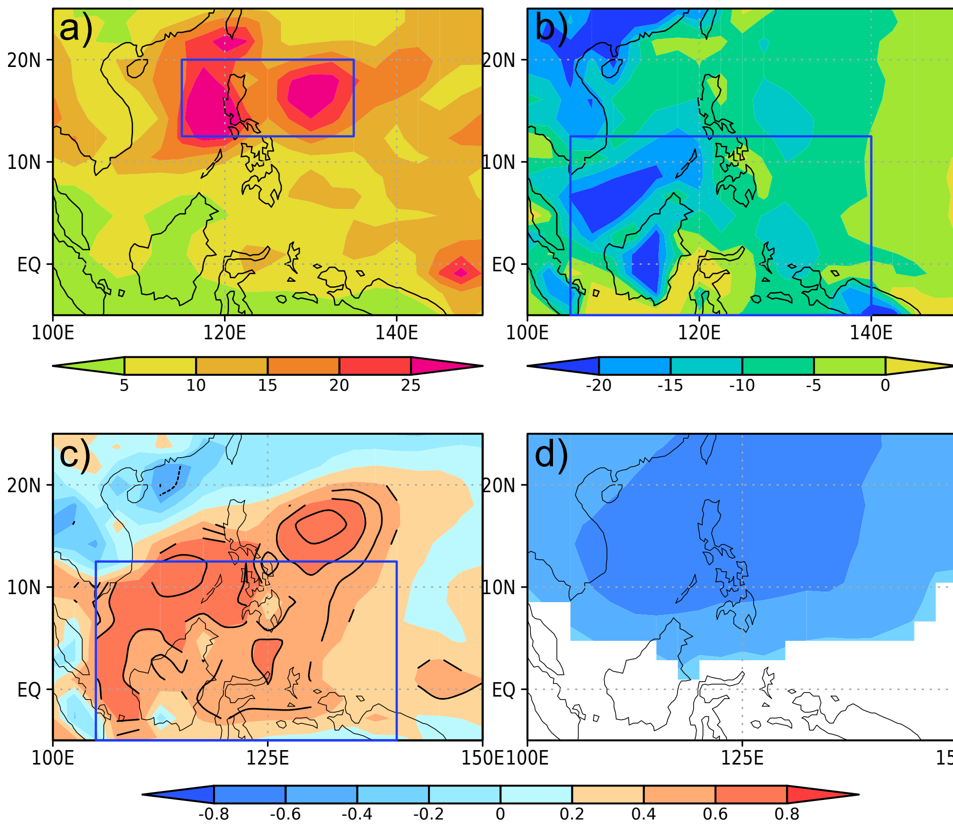

Figure 5.1: (a) variance of the MJJA mean precipitation difference between cpl_4×CO_2 and amip_4×CO_2sst. (b) difference of MJJA mean LHFLX between cpl_4×CO_2 and amip_-4×CO_2sst. (c) point correlation coefficient between precipitation difference index (area averaged precipitation difference over the blue box in (a)) and the LHFLX difference between cpl_4×CO_2 and amip_4×CO_2sst. (d) point correlation coefficient between LHFLX difference index (area averaged LHFLX difference over the blue box in (c)) and 850-hPa GPH difference between cpl_4×CO_2 and amip_4×CO_2sst. In (a) the region enclosed by the blue box is (115°E-140°E, 12.5°N-20°N). In (b) and (c) the region in the blue boxes is (105°E-140°E, 5°S-12.5°N).

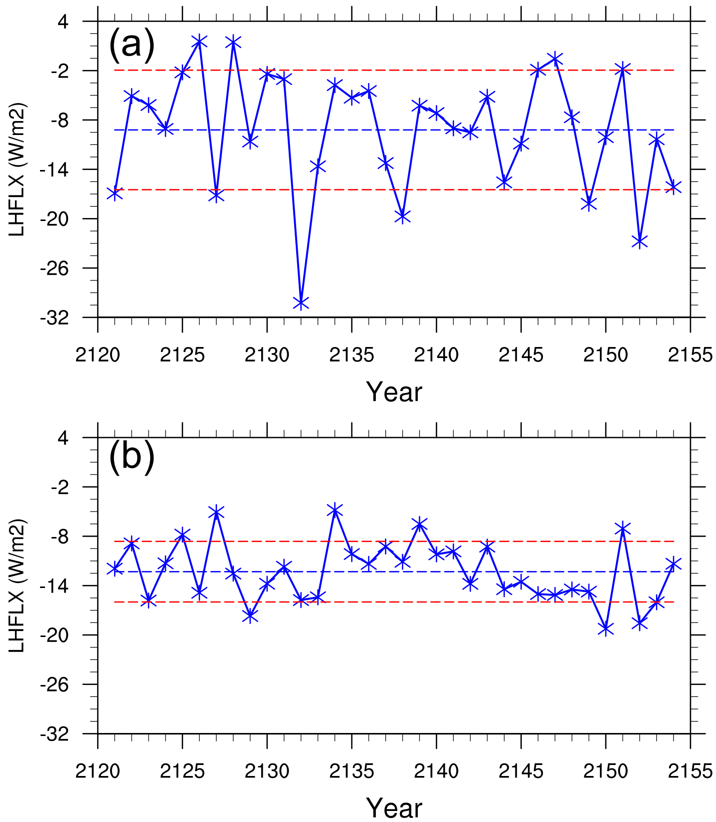

Figure 5.2: Difference of MJJA mean area averaged LHFLX (105°E-140°E, 5°S-12.5°N). (a) difference between cpl_4×CO_2 and amip_4×CO_2sst. (b) difference between amip_4×CO_2sst_lhflx and amip_4×CO_2sst. The blue dashed lines denote the mean of the difference. The red dashed lines denote the one standard deviation.

the LHFLX difference between cpl_4×CO_2 and amip_4×CO_2sst is calculated (Fig.5.5c). The black contours enclosed the region where the correlation coefficient exceeds the 95% significance level. The result shows that the maximum correlation is over the equatorial WP, which means that the changes of precipitation over northern SCS and adjacent WP are highly related to the changes of LHFLX over the tropics.

To confirm that the tropical LHFLX affects WNPSH, a similar correlation was computed between the LHFLX index (area average of LHFLX difference over the blue box, 105°E-140°E, 5°S-12.5°N) and the 850-hPa GPH difference between cpl_4×CO_2 and amip_4×CO_2sst (Fig.5.1d). It indicates that the high LHFLX over tropical WP is related to the weaker 850-hPa GPH over the subtropics, i.e., the strong (weak) convective activity over tropical WP is related to the eastward (westward) displacement of WNPSH. The distribution of the MJJA mean LHFLX difference between cpl_4×CO_2 and amip_4×CO_2sst shows that, over tropical WP, the LHFLX in cpl_4×CO_2 is around 10W/m^2 lower than that in amip_4×CO_2sst (Fig.5.1b).

The LHFLX deficiency over tropical WP was mimicked in amip_4×CO_2sst_lhflx run. Figure 5.2a shows the area average (105°E-140°E, 5°S-12.5°N) of MJJA mean LHFLX difference between cpl_4×CO_2 and amip_4×CO_2sst from 2121 to 2154. The average of the LHFLX difference is around −10 W/m^2. This difference is added to the amip_4×CO_2sst_-lhflx run during MJJA in each year, thus reducing the latent heat flux in that run. The area average of LHFLX difference between amip_4×CO_2sst and amip_4×CO_2sst_lhflx is depicted in Fig.5.2b, which is around −12 W/m^2.

5.2 Results

5.2.1 The amip_4×CO_2sst experiment

The climatological MJJA mean precipitation is compared among pdControl, amip_4×CO_2sst, and cpl_4×CO_2 (Fig. 5.3). The comparison to pdControl gives an estimation of the EASM response to global warming whereas the comparison to cpl_4×CO_2 is intended to estimate the effects of the air-sea feedbacks. The response of the EASM precipitation to the surface warming in the amip_4×CO_2sst experiment shows a large amount of precipitation over SCS and adjacent WP, southern China, and south of Japan. The difference of precipitation between amip_4×CO_2sst and cpl_4×CO_2 (Fig.5.3e) shows that the lack of coupling induces a stronger precipitation over SCS and WP, as well as the region to the north of 30°N in response to the global warming.

Because the EASM precipitation is affected by the position of WNPSH and its associated moisture transport, their response to global warming in the uncoupled simulation is also compared to the coupled response (Fig. 5.4). In amip_4×CO_2sst, the WNPSH is relatively

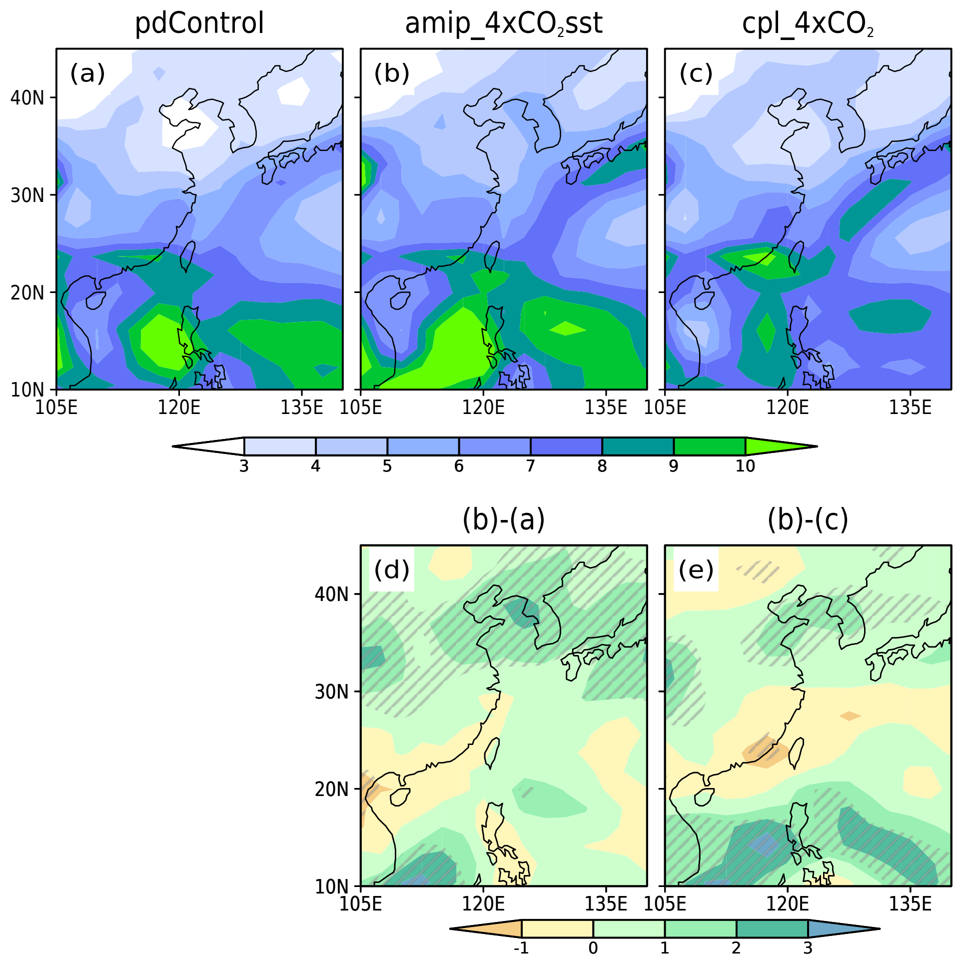

Figure 5.3: (a)-(c) MJJA mean precipitation rate for pdControl, amip_4×CO_2sst, and cpl_4×CO_2, respectively (unit: mm/day), (d) difference between amip_4×CO_2sst and pdControl, and (e) difference between amip_4×CO_2sst and cpl_4×CO_2.

weaker and displaced eastward compared with that in cpl_4×CO_2. This indicates that the warming up of the boundary conditions is favorable for the intensification and the westward extension of the WNPSH. However, the lack of the air-sea feedback in amip_4×CO_2sst inhibits the WNPSH from extending as far westward as in cpl_4×CO_2

The westward extension of the WNPSH changes the low-level circulation and the moisture transport. In pdControl, the moisture from SCS flows northward into East Asia, emerging with the northward moisture transport from WNP (Fig. 5.5a). In amip_4×CO_2sst run,

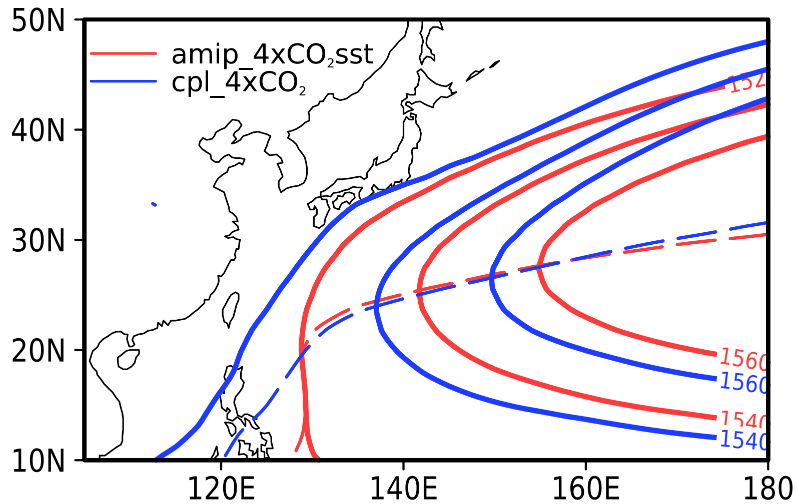

Figure 5.4: MJJA mean GPH at 850-hPa in amip_4×CO_2sst (red), and cpl_4×CO_2 (blue). The dashed lines denote subtropical ridge.

the enhanced moisture is transported by southwesterly flow over East Asia (Fig.5.5b). This northeastward moving moisture transport is further amplified in cpl_4×CO_2, which leads to a maximum moisture band from northern SCS to southern Japan (Fig. 5.5c). In addition, compared with cpl_4×CO_2, the moisture transport in amip_4×CO_2sst is reduced over the subtropical monsoon trough (South China to southern Japan), and is increased over eastern SCS and adjacent WNP. The difference in the moisture transport between amip_4×CO_2sst and cpl_4×CO_2 is related to the shape of the WNPSH. For instance, the isoline of 1520-m in amip_4×CO_2sst is almost parallel to the 130°E longitude, while in cpl_4×CO_2, the 1520-m isoline tilts northeastward and is located closer to the East Asia continent (Fig. 5.4). Therefore, in amip_4×CO_2sst the moisture transport over South China to southern Japan is weaker than in cpl_4×CO_2.

5.2.2 amip_4×CO_2sst v.s. amip_4×CO_2sst_lhflx

In this section, the EASM simulated by amip_4×CO_2sst and amip_4×CO_2sst_lhflx will be analyzed, including the seasonal mean state, interannual variability, and annual cycle. The difference between these two experiments implies the influence of the convection over tropical

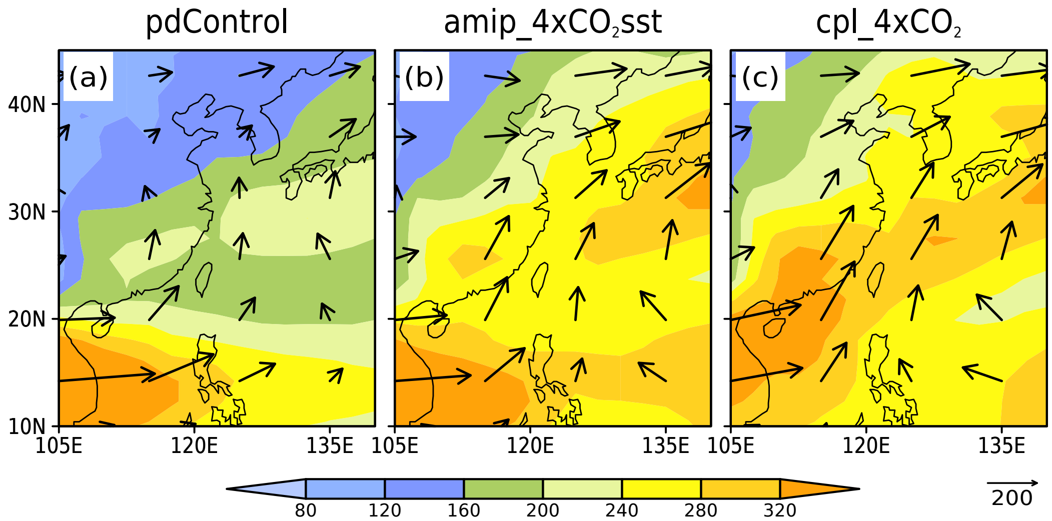

Figure 5.5: MJJA mean vertically integrated moisture transport (unit: Kg $m^{-1}s^{-1}$). Shadings denote the magnitude, and the vectors denote the direction.

SCS and adjacent WP on the EASM. Since amip_4×CO_2sst_lhflx mimicks cpl_4×CO_2, the results of cpl_4×CO_2 are also compared with the above two model experiments.

5.2.2.1 Mean state

Figure 5.6 shows the westernmost and the easternmost contours of the 1540-m GPH isoline in cpl_4×CO_2, amip_4×CO_2sst, and amip_4×CO_2sst_lhflx. This indicates the movement range of the MJJA mean GPH at 850 hPa. In cpl_4×CO_2, the 1540-m isoline moves within the range between around 120°E and 150°E (red contours), whereas, in amip_4×CO_2sst, the 1540-m isoline migrates from 128°E to 155°E (green contours). In amip_4×CO_2sst_lhflx, it moves between 120°E and 152°E (blue contours), which is closer to the range of the GPH position in cpl_4×CO_2. This implies that the lack of convective activity in SCS and nearby WP favors the westward movement of the WNPSH.

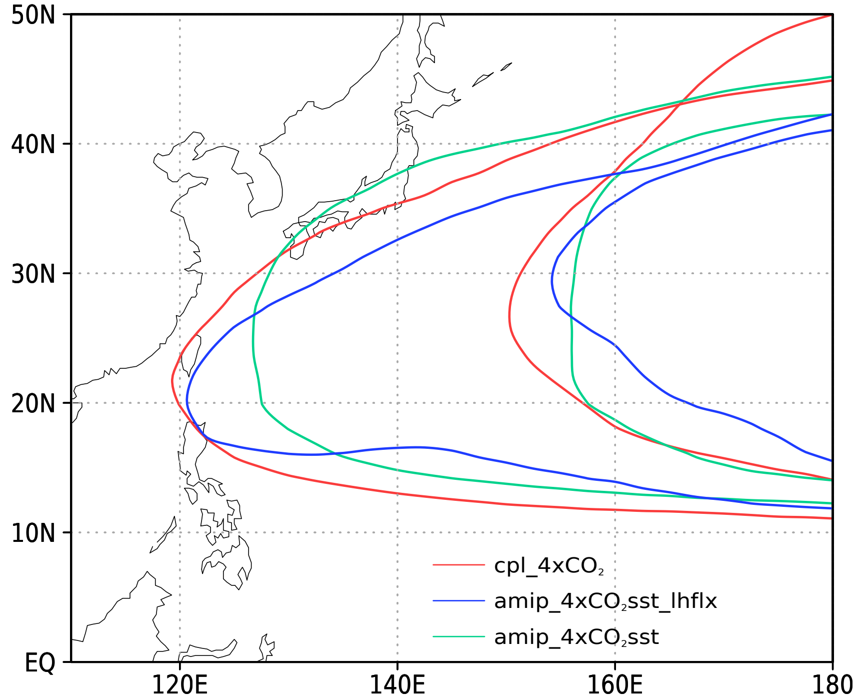

Figure 5.6: The westernmost and the easternmost contours of the MJJA mean 1540-m GPH isoline in cpl_4×CO_2 (red), amip_4×CO_2sst (green), and amip_4×CO_2sst_lhflx (blue).

5.2.2.2 EASM Interannual Variability

Canonical Correlation Analysis (CCA) was used to investigate the linkage between WNPSH and precipitation (description in Section 2.3.7). It is applied to the MJJA mean precipitation and 850-hPa GPH. It describes the simultaneous response of the MJJA precipitation over East Asia to the WNPSH anomalies. The domain for the precipitation is (110°E-135°E, 10°N-50°N), and the domain for the 850-hPa GPH is (110°E-180°E, 10°N-50°N). The time mean of precipitation and GPH has been subtracted from each dataset, separately. The CCA is carried out for five different datasets: observation, pdControl, cpl_4×CO_2, amip_4×CO_2sst, and amip_4×CO_2sst_lhflx. In observation, cpl_4×CO_2, and amip_4×CO_2sst_lhflx, 2 PCs of precipitation and 3 PCs of 850-hPa GPH are selected. In pdControl the

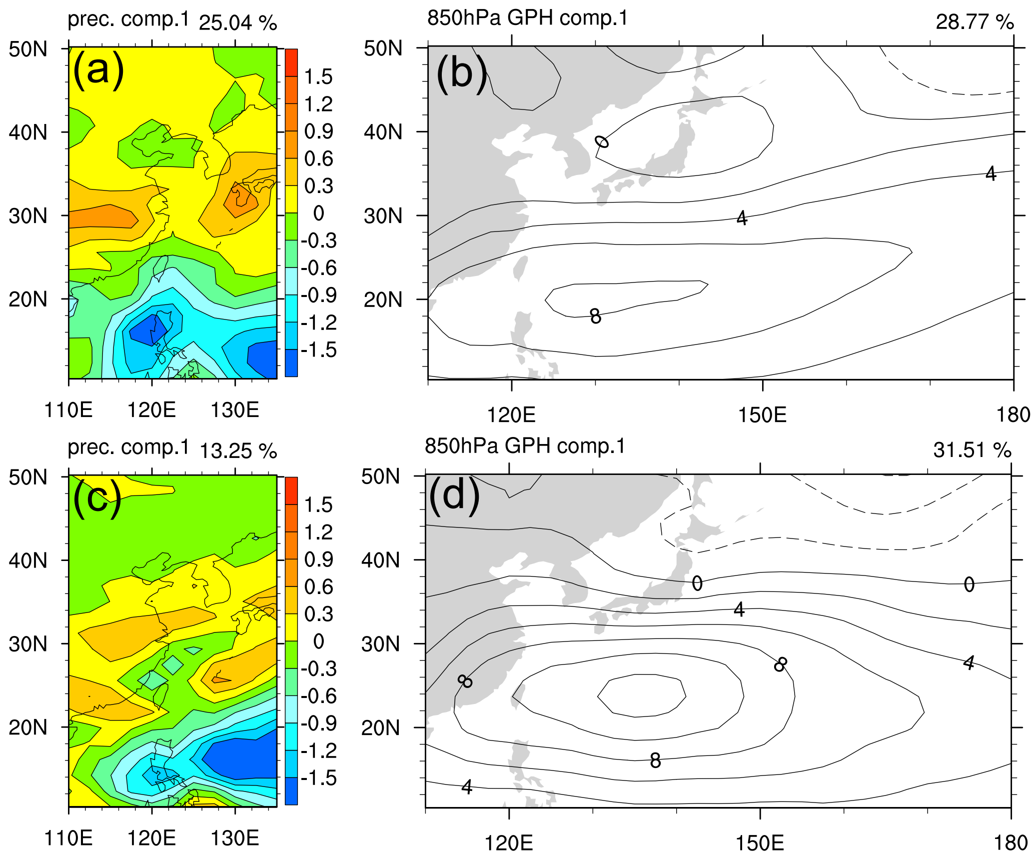

Figure 5.7: First pattern of CCA of precipitation and 850-hPa GPH. (a)-(b) observation. (c)-(d) pdControl.

data is truncated to 3 PCs of precipitation and 3 PCs of GPH. In amip_4×CO_2sst 2 PCs of precipitation and 4 PCs of GPH are selected. The canonical correlations based on the above truncations exceed the 99% significance level.

Firstly, the result of pdControl was compared with observations to validate the models performance. The first CCA pair in observation (Fig.5.7a and Fig.5.7b) accounts for 25.04% of the total MJJA precipitation variance over East Asia and 28.77% of WNPSH variability. The correlation between the precipitation and 850-hPa GPH coefficient time series of the first CCA pair is 0.91 (Figure not shown). In pdControl, the first pair of CCA (Fig.5.7c and Fig.5.7d) explains 13.25% of the total precipitation variance and 31.51% of the 850-hPa GPH. It exhibits a correlation coefficient between the precipitation and 850-hPa GPH time series of 0.72 (Figure not shown).

SP-CCSM4 captures the relationship between the EASM precipitation and WNPSH. Both the observation and the pdControl show that the amplification of the WNPSH (around 20°N) is related to insufficient precipitation over tropical SCS and WP and excessive precipitation over Southeast China and southern Japan. The difference between the observation and pdControl lies in the magnitude and the position of the GPH anomaly. In observation, the maximum GPH anomaly is around 8 m, and its center is located around (130°E, 20°N). In pdControl, the center of the maximum GPH anomaly is displaced northward, and the magnitude of the maximum GPH anomaly is around 12m. Accordingly, the precipitation anomalies over East Asia tilt northward.

The same method is applied to the other three experiments: cpl_4×CO_2, amip_4×CO_2sst, and amip_4×CO_2sst_lhflx (Fig. 5.8). The variance explained by the first CCA pair is comparable in three experiments, except that the variance explained by precipitation is higher in amip_4×CO_2sst_lhflx (Fig. 5.8e). For precipitation (850-hPa GPH), the first CCA pair accounts for 29.83% (26.1%), 25.71% (25.91%), and 36.3% (27.9%) of the total variance for amip_4×CO_2sst, cpl_4×CO_2, and amip_4×CO_2sst_lhflx, respectively. For the first CCA pattern of precipitation, all the three experiments show a dipole structure: negative anomalies over SCS and tropical WP, and positive anomalies to its north.

One can still notice the difference among the three simulations. In amip_4×CO_2sst_lhflx (Fig. 5.8e-f), the region of the negative precipitation anomaly over SCS is mostly located to the north of 10°N, which is similar to that in cpl_4×CO_2 (Fig. 5.8c-d). However, in amip_4×CO_2sst (Fig. 5.8a-b), the negative precipitation anomaly over SCS is displaced southward. In addition, compared with amip_4×CO_2sst (Fig. 5.8a-b), in amip_4×CO_2sst_lhflx (Fig. 5.8e-f), the center of the maximum GPH anomalies moves westward, and the magnitude of the GPH anomalies is enhanced. This pattern is closer to cpl_4×CO_2 (Fig. 5.8d).

The CCA reveals that the weaker convection over tropical SCS and WP is related to the westward displacement of WNPSH, and thus influences the precipitation. Moreover, it indicates that the changes of LHFLX in amip_4×CO_2sst_lhflx, although with a small

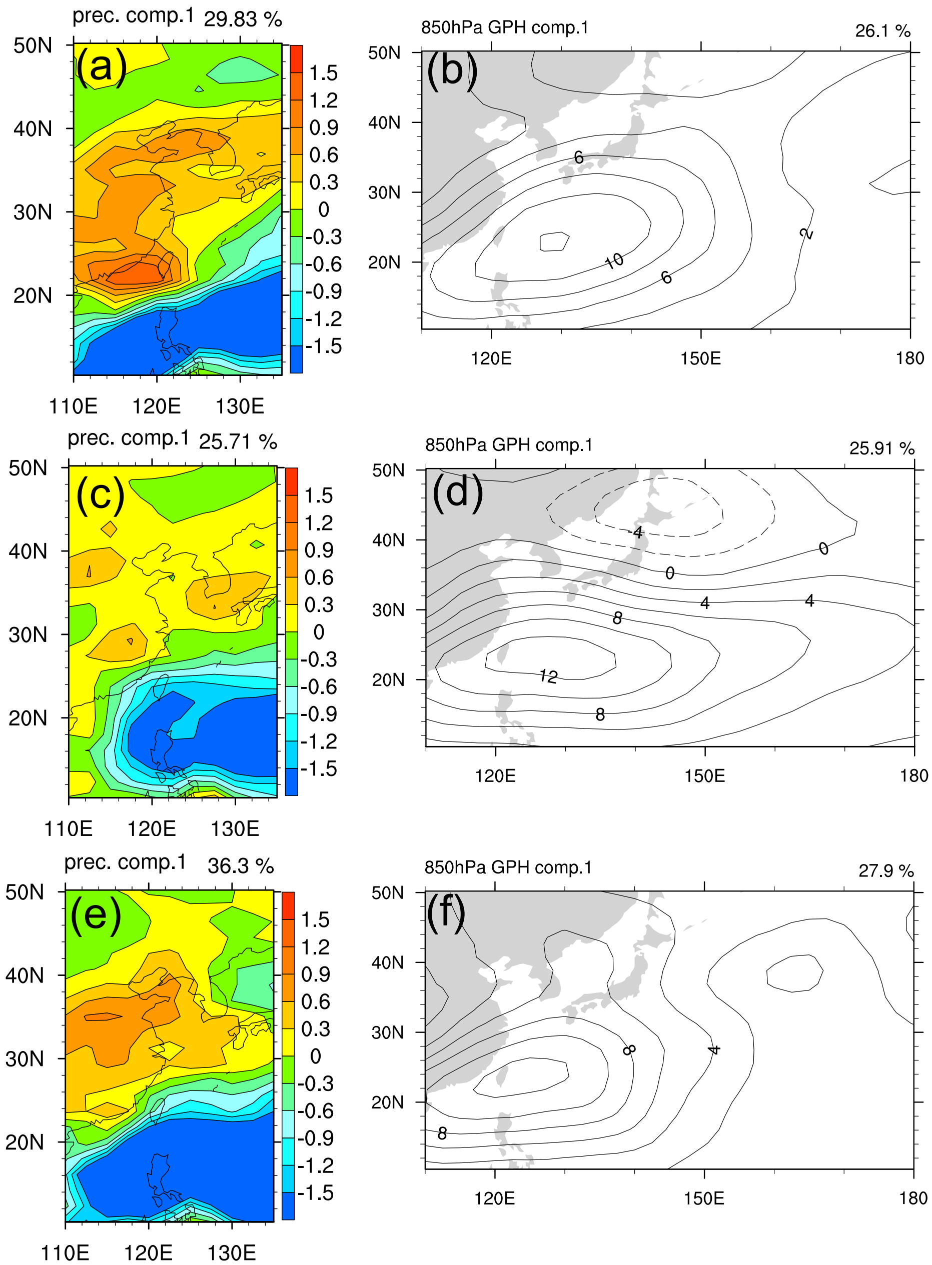

Figure 5.8: First pattern of CCA of precipitation and 850-hPa GPH. (a)-(b) amip_-$4\times CO_2$sst, (c)-(d) cpl_$4\times CO_2$, (e)-(f) amip_$4\times CO_2$sst_lhflx.

magnitude, is trying to reproduce the features in cpl_$4\times CO_2$.

5.2.2.3 Annual Cycle

The annual cycle of the EASM precipitation has been described in detail by Ding et al. (2005) and Ding and Chan (2005). Generally, the onset of the EASM occurs around the end of April or early May in the central Indochina Peninsula. Then the rain belt propagates northward and merges with the rain belt over South China, which represents the first standing stage of the EASM. Around 10 June the rain belt jumps northward to Southeast China and persists till early July. This rainy episode represents the Mei-yu season and is also referred to as the second standing stage of the EASM annual cycle. Afterwards, the rain belt advances northward again and reaches North China. This stepwise propagation of the precipitation is a unique phenomenon of EASM. The annual cycle of the EASM is usually depicted by the pentad mean precipitation averaged between 110°E-120°E (Ding and Chan, 2005).

The meridional migration of the WNPSH can be described by an index based on the GPH at 850-hPa (Zhang and Tao, 1999) (description in Section 2.3.3). Figure 5.9 shows the annual cycle of the EASM precipitation superimposed with WNPSH index from May to August for three model simulations, amip_4×CO_2sst, cpl_4×CO_2, and amip_4×CO_2sst_-lhflx. In all the three simulations, the advancement of the rain band reflects the monsoon onset as well as the stepwise northward propagation. Also, the precipitation migrates with the WNPSH ridge.

In amip_4×CO_2sst (Fig. 5.9a), the onset of the EASM occurs at around 16 May when the tropical rain band merges with the rain band at 20°N. Around 16 June, the rain belt moves northward and stays between 30°N and 34°N, indicating the Mei-yu season. It lasts until the beginning of July when the rain belt jumps again and reaches 40°N. The precipitation stays at 35°N-38°N during July and August.

In cpl_4×CO_2 (Fig. 5.9b), the three jumps of the rain belt occur at similar times as in amip_4×CO_2sst (Fig. 5.9a). However, in cpl_4×CO_2, there is excessive precipitation during the first standing stage (mid-May to early June) between 20°N-30°N. The Mei-yu onset is not obvious because there is large amount of precipitation at 30°N before mid-June. Meanwhile, the rain band reaches north of 40°N during July and August, and starts retreating southward at early August.

In amip_4×CO_2sst_lhflx (Fig. 5.9c), the onset of the EASM is around 10 days later than in the amip_4×CO_2sst (Fig. 5.9a). Moreover, there is no obvious Mei-yu onset although there are active and break phases of the precipitation at 30°N in June. At the beginning of July, the rain band jumps northward and stays between 35°N-40°N during July and August, and retreats southward after it reaches the northernmost position in late July.

The difference of precipitation and WNPSH index between cpl_4×CO_2 (amip_4×CO_2sst_lhflx) and amip_4×CO_2sst is shown in Fig. 5.9d (Fig. 5.9e).The difference in the precipitation is associated with the difference in WNPSH migration. There are some similarities in these two difference plots. For instance, there is lack of precipitation between 10°N and 20°N, especially during May and June, which is related to the weaker convection over tropical SCS and WP in these two runs. Also, the precipitation between 35°N and 40°N is reduced in cpl_4×CO_2 and amip_4×CO_2sst_lhflx, which is related to the northward displaced WNPSH in July and August.

Figure 5.10 shows the annual cycle of vertically integrated moisture transport and moisture convergence of amip_4×CO_2sst, cpl_4×CO_2, amip_4×CO_2sst_lhflx, and their difference. In all the three model experiments (Fig. 5.10a-c), there is northward propagation of moisture over East China. The moisture convergence zone keeps staying between 25°N-33°N until the beginning of July. Afterwards, the region of 30°N-40°N is dominated by moisture divergence.

The difference between cpl_4×CO_2 and amip_4×CO_2sst (Fig. 5.10d) indicates that, in cpl_4×CO_2, there is stronger northward moisture transport over the area 25°N-30°N from May to June, which is related to the excessive precipitation in Fig. 5.9d. In amip_4×CO_2sst_lhflx (Fig. 5.10e), there is stronger northeastward moisture propagation over 30°N-40°N in May, and over 20°N-30°N in June, which is consistent with the enhanced precipitation there (Fig. 5.9e).

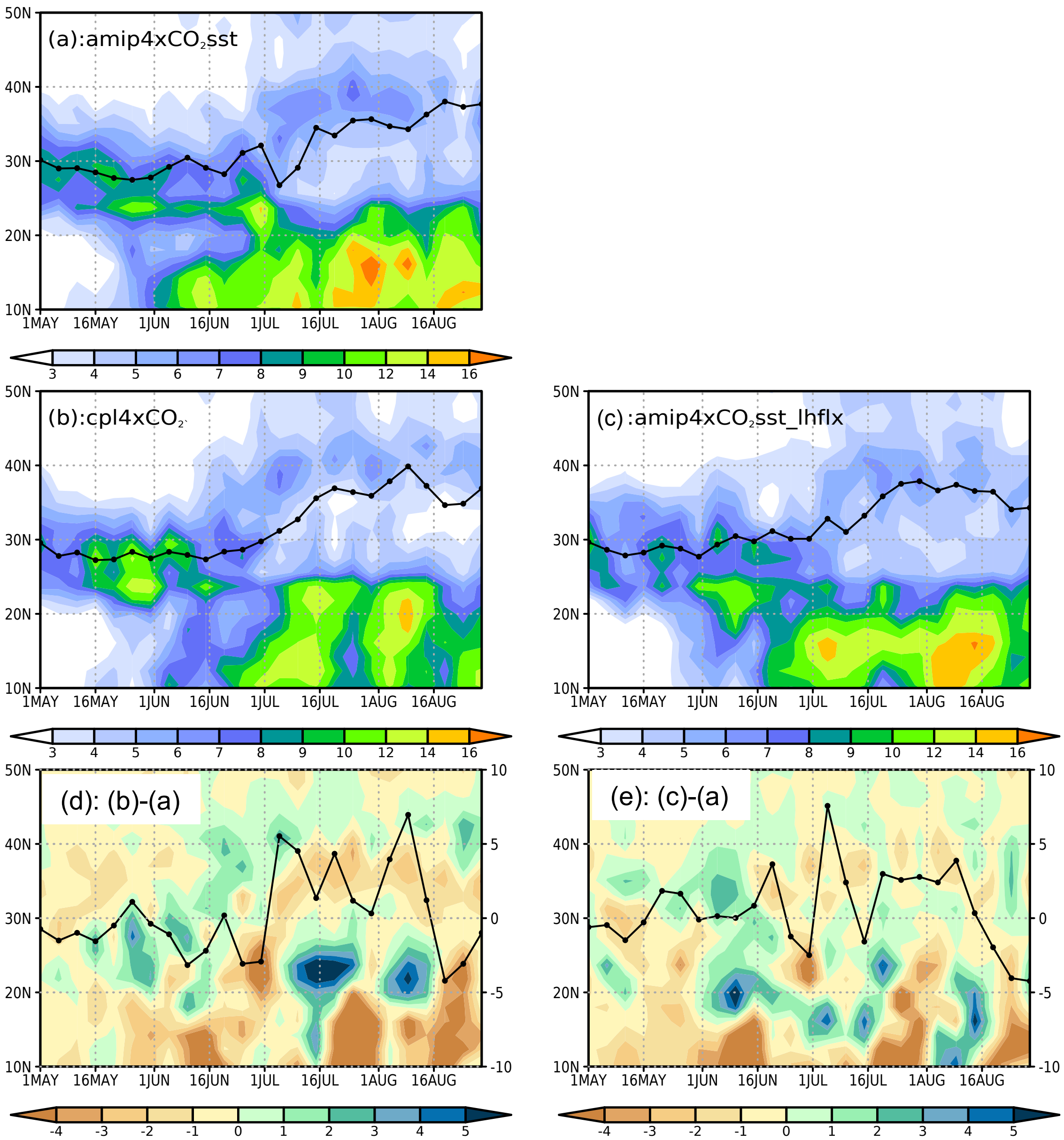

Figure 5.9: Annual cycle of precipitation and 850-hPa GPH index. (a) amip_4×CO_2sst, (b) cpl_4×CO_2, (c) amip_4×CO_2sst_lhflx, (d) difference of precipitation between cpl_4×CO_2 and amip_4×CO_2sst, and (e) difference of precipitation between amip_4×CO_2sst_lhflx and amip_4×CO_2sst. The y axis on the right side in (d) and (e) denotes the difference of the WNPSH index.

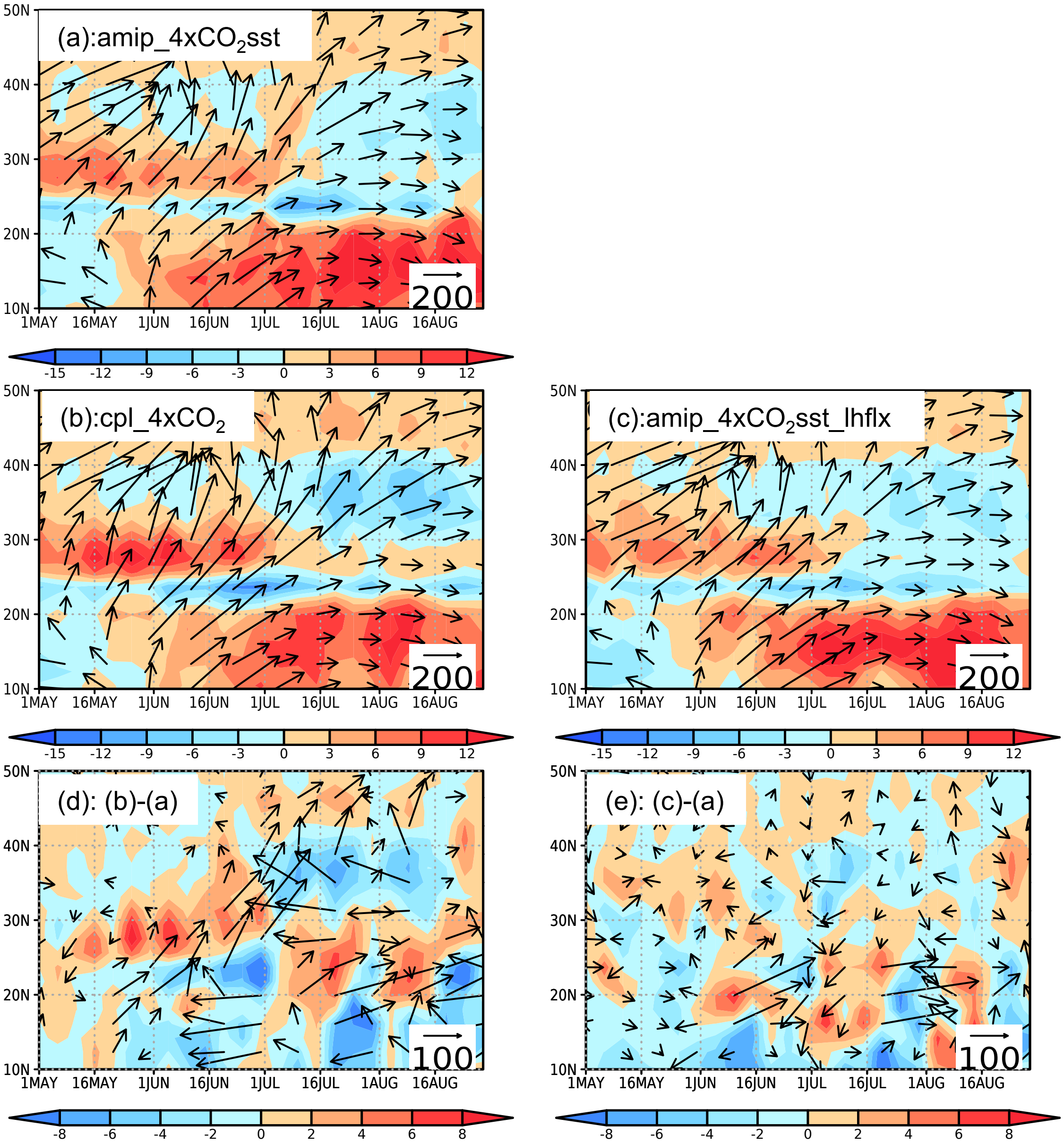

Figure 5.10: Same as Fig. 5.9, but for the vertically integrated moisture transport (vectors, unit: Kg $m^{-1}s^{-1}$) and moisture convergence (shadings, unit: Kg $m^{-2}s^{-1}$).

The changes in LHFLX over tropics result in the changes in vertical motion, and thus has an impact on the local meridional circulation. Figure 5.11 shows the zonal averaged (110°E-120°E) meridional circulation and meridional moisture transport at vertical levels in amip_4×CO_2sst (Fig. 5.11a), and its difference between cpl_4×CO_2 (Fig. 5.11b) and amip_4×CO_2sst_lhflx (Fig. 5.11c).

In amip_4×CO_2sst experiment, over EASM area, there is ascending motion over tropics and also over the area between 20°N-30°N in May. In June, there is uniform upward motion from equator to 30°N, along with another small branch at 40°N. The ascending branch around 40°N amplifies in July and becomes weaker in August. The southerly flow lasts for four months because East Asia is located to the western side of the WNPSH. The magnitude of the southerlies intensifies in June, and reaches the maximum in July. In August, it weakens. The meridional moisture transport shows the similar pattern with the meridional wind (Fig. 5.11a).

In cpl_4×CO_2 (Fig. 5.11b), the southerlies between 10°N and 20°N strengthen in May. In June, the increased southerly flow are located between 20°N-30°N. During July and August, the maximum southerly anomalies occur around 40°N. The stronger meridional wind comes with the stronger ascending motion to its north and descending motion to its south. The moisture transport anomalies move with the merdional wind anomalies. The changes of meridional circulation and meridional moisture transport between cpl_4×CO_2 and amip_4×CO_2sst are consistent with the changes in the annual cycle of the precipitation (Fig. 5.9 and Fig. 5.10).

In amip_4×CO_2sst_lhflx (Fig. 5.11c), there are descending anomalies from equator to 15°N where the LHFLX was decreased, which confirms that, in the model, the reduced LHFLX over tropical WP results in a weaker ascending motion above. The changes of meridional wind and vertical wind have similar features as in cpl_4×CO_2 in May and June. For instance, there is southerly anomaly and moisture transport at lower troposphere between 20°N-30°N. However, during July and August, the southerly anomalies are not as strong as in cpl_4×CO_2. The changes at 40°N may be related to the circulation systems at

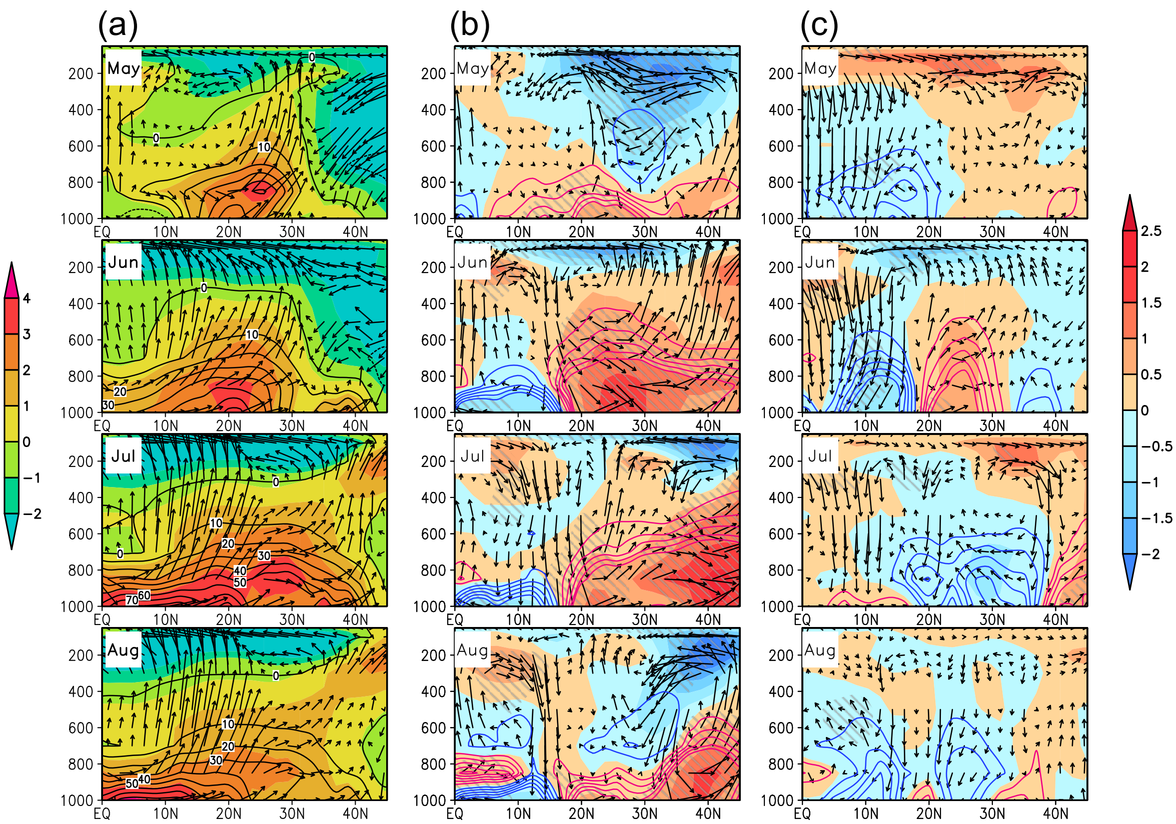

Figure 5.11: (a) Meridional circulation and moisture transport from May to August in amip_4×CO_2sst. (b) difference of meridional circulation and moisture transport between cpl_4×CO_2 and amip_4×CO_2sst, (c) difference between amip_4×CO_2sst_lhflx and amip_4×CO_2sst. Shadings denote the difference of meridional velocity. Contours denote the difference of meridional moisture transport (unit: g/kg×m/s). The contour interval is 1. The grey slashes in (b) and (c) denote the region where the difference of merdional velocity exceeds the 95% significance level.

mid-latitudes.

Therefore, in both cpl_4$\times$$CO_2$ and amip_4$\times$$CO_2$sst_lhflx experiments, the MJJA mean LHFLX at tropics is reduced compared with amip_4$\times$$CO_2$sst, and also the precipitation between 30°N-40°N is decreased in late summer (July and August). In both experiments the WNPSH reaches a higher latitude after July, which results in a divergence zone to the south of the subtropical ridge. However, there are some differences between cpl_4$\times$$CO_2$ and amip_4$\times$$CO_2$sst_lhflx. In cpl_4$\times$$CO_2$ the stronger northeastward flow transports more moisture to the north, which creates more precipitation to the north of 40°N in late summer and thus less precipitation between 30°N-40°N. In amip_4$\times$$CO_2$sst_lhflx, there is insufficient moisture and also weaker northward moisture transport during July and August, leading to decreased precipitation over 30°N-40°N.

The LHFLX changes in the tropics influences the precipitation over East Asia through WNPSH. Figure 5.12 shows the monthly mean of the low level wind and 850-hPa GPH for amip_4$\times$$CO_2$sst and its difference between cpl_4$\times$$CO_2$ (cpl_4$\times$$CO_2$ minus amip_4$\times$$CO_2$sst) and between amip_4$\times$$CO_2$sst_lhflx (amip_4$\times$$CO_2$sst_lhflx minus amip_4$\times$$CO_2$sst). From May to August, there is southwesterly flow over East Asia, which is located to the northwestern edge of the WNPSH. The southwesterly flow changes its direction and magnitude with the changes of the WNPSH. For instance, in July and August, the WNPSH moves northward, and therefore, the southwesterlies over East Asia turn into southerlies (Fig. 5.12a).

In cpl_4$\times$$CO_2$ (Fig. 5.12b), the WNPSH is strengthened from May to August. In May, the positive GPH anomalies extend from SCS to mid-latitude WP, with the center of the maximum anomalies located at around (150°E, 15°N). In June, the positive GPH anomalies are strengthened, and expand northward. Accordingly, there are anti-cyclonic anomalies over the region with positive GPH anomalies. In July and August, the anomalies of wind and GPH show a wavy structure. From SCS to mid-latitude WP, there are anti-cyclonic, cyclonic, anti-cyclonic anomalies.

In amip_4$\times$$CO_2$sst_lhflx, the WNPSH is also intensified, except in July (Fig. 5.12c). The reduced convection over tropical SCS and WP induces an anti-cyclonic anomaly over

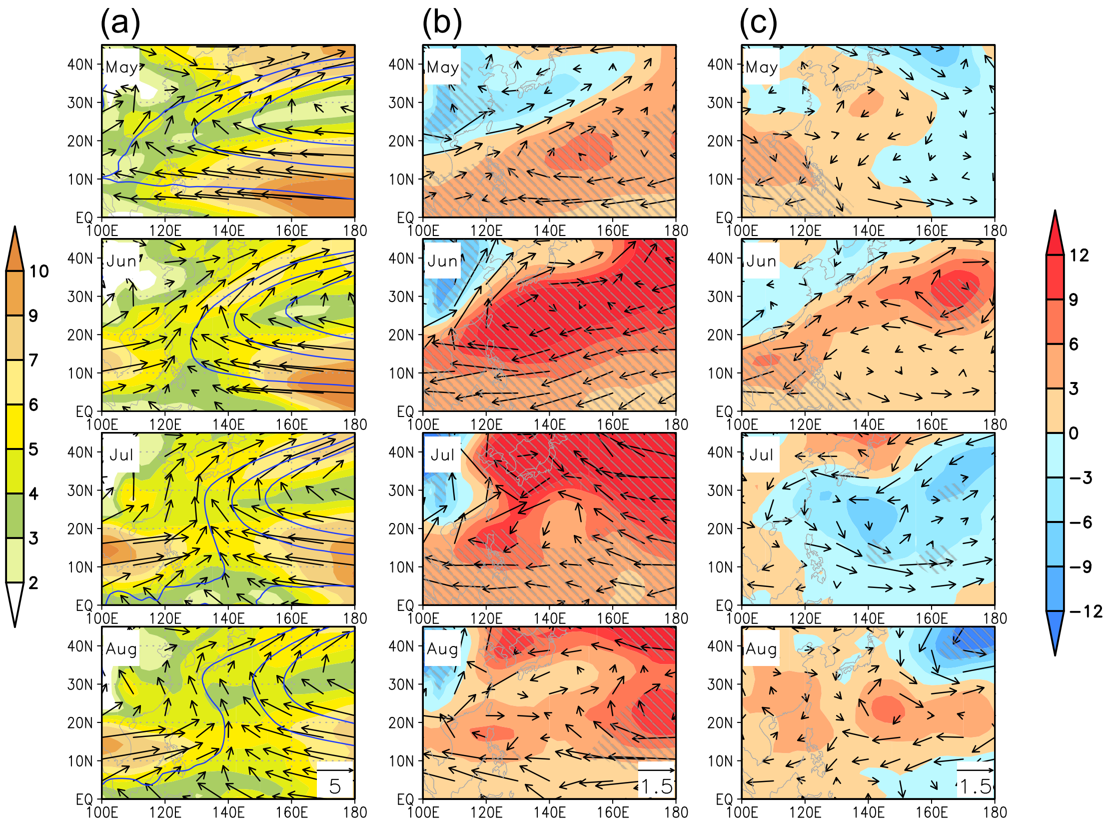

Figure 5.12: The wind and GPH at 850 hPa from May to August in amip_4×CO_2sst. (b): The difference of meridional circulation and moisture transport between cpl_4×CO_2 and amip_4×CO_2sst, (c): the difference between amip_4×CO_2sst_lhflx and amip_4×CO_2sst. In (a) shadings denote the magnitude of the wind, vectors are the directions of horizontal wind, contours are the isolines of 1520, 1540, 1560m. In (b) and (c) shadings denote the difference of 850-hPa GPH, vectors denote the difference of wind. Grey dots denote the region where the geopotential difference is above 95% significance level.

northern SCS from May to August. However, the magnitude and the location of such anomaly varies. In May, there are positive GPH anomalies over SCS and southern Japan, along with anti-cyclonic anomalies there. In June, there are three centers of positive GPH anomaly from SCS to the east of Japan. The westerlies (southwesterlies) on the northern (northwestern) flank of the GPH anomalies strengthen the southwesterly flow over northern SCS to southern Japan. In July, the anti-cyclonic anomaly over SCS is displaced westward. There are two centers of negative GPH anomaly over subtropical WP, along with cyclonic anomalies there. In August, there are anti-cyclonic anomalies over SCS and southern China. However, the northerly anomalies on the eastern side of the anti-cyclonic anomaly reduce the prevailing southerly flow.

5.3 Conclusion and Discussion

Because the amip_4×CO_2sst_lhflx experiment mimicks the MJJA mean LHFLX over tropical SCS and nearby WP in cpl_4×CO_2, one would expect that the impacts of the differences between amip_4×CO_2sst_lhflx and amip_4×CO_2sst may share similar features with the influences of the difference between cpl_4×CO_2 and amip_4×CO_2sst. The CCA reveals that the reduced LHFLX over the tropics leads to larger positive anomalies of the GPH over SCS and adjacent WNP (Fig. 5.8) during MJJA. Meanwhile, the annual cycle of the EASM shows that the precipitation is increased over South/Southeast China in June, and is decreased over North China in July and August (Fig. 5.10).

The reduced LHFLX over tropical WP will decrease the ascending motion above, thus affecting the local meridional circulation, for instance, the increased ascending motion in subtropics (Fig. 5.11). Therefore, the stronger southerly flow at surface will transport more moisture to the north. Although the LHFLX is reduced in the tropics, the moisture can still be transported further north. This can been seen in cpl_4×CO_2 (Fig. 5.11b). However, in amip_4×CO_2sst_lhflx, the northward moisture transport increase is not as strong as in cpl_4×CO_2 (Fig. 5.11c). Moreover, in cpl_4×CO_2, the ascending anomalies at 25°N merge with the one in 40°N, amplifying the northward moisture transport (Fig. 5.11b). In amip_4×CO_2sst_lhflx, the southerly and moisture transport becomes weaker after June (Fig. 5.11c). This is consistent with the low level wind changes in amip_4×CO_2sst_lhflx (Fig. 5.12c), where northerly anomalies are seen over East Asia in July and August, a configuration which is not favorable for the northward propagation of moisture.

The decreased LHFLX over SCS and adjacent WP will induce a Gill-type anti-cyclonic anomaly. Meanwhile, the changes of LHFLX over tropics result in a Rossby wave train from tropical to midlatitude Pacific Ocean. The westerly anomalies on the northern side of the anomalous anti-cyclonic circulation intensify the underlying southwesterly flow, thus leading to the amplification on the western edge of the WNPSH. However, the changes of the WNPSH depends on the position of the wind anomaly. For example, in amip_4×CO_2sst_lhflx (Fig. 5.12c), there are anti-cyclonic anomalies over SCS and eastern Japan in June, leading to an intensified southwesterly flow from southeastern China to Japan. However, in July, the anti-cyclonic anomaly is confined over southern SCS, and there is cyclonic anomaly to its north, which results in a northeasterly anomaly over East Asia.

The difference between amip_4×CO_2sst_lhflx and amip_4×CO_2sst is not as prominent as the difference between cpl_4×CO_2 and amip_4×CO_2sst. This is because the LHFLX is modified over a small region in amip_4×CO_2sst_lhflx, and the magnitude of such change is small. Plus, only the MJJA mean LHFLX difference is subtracted.

Chapter 6: Summary and Discussion

6.1 Summary

This study is focused on investigating the mechanisms explaining the EASM response to global climate change. Previous studies have shown that the changes in the mean state of the EASM is due to the changes in WNPSH (Li et al., 2012; Wang et al., 2013; Xiang et al., 2013; Zhou et al., 2009). However, these studies did not analyze the impact of the remote air-sea interaction on the WNPSH. Therefore, the main objective of this study is to investigate in the global warming scenario, how the air-sea interaction over tropical WP affects the EASM through its influence on the WNPSH.

The conclusions of this question were obtained by running numerical simulations. It reveals that there are two factors that affect the WNPSH in a warmer climate. One is the warming of boundary conditions, which is more important than the atmospheric warming, favoring the intensification and westward extension of the WNPSH. The other is the convective activity over tropical SCS and WP, which influences the movement of the WNPSH. The weak (strong) convection over tropical SCS and WP favors (inhibits) the westward extension of the WNPSH. The low level circulation system induced by the convection over tropical SCS and WP influences the prevailing southwesterlies over East Asia, and therefore affecting the WNPSH. However, the influence of the tropical convection on the WNPSH lasts from May to June. During July and August, the changes in the WNPSH are affected by the systems in mid-latitudes.

In order to analyze this question, a model which can simulate the main features of the EASM is required. In this study, SP-CCSM4 is used, which is a coupled climate model with super-parameterization as the method for the representation of cloud processes. It has shown significant improvements in the simulation of many of the components of the global monsoon systems (DeMott et al., 2011; McCrary et al., 2014). However, the ability of SP-CCSM4 in EASM simulation was unknown, and therefore, the performance of SP-CCSM4 in simulating EASM was evaluated to demonstrate the adequacy of the model. Its performance was evaluated against a conventionally-parameterized model, CCSM4, and observations.

The SP-CCSM4 model captures the main features of observed EASM climatology plus the mechanisms associated with the northward propagation of the intraseasonal oscillation. Both the SP-CCSM4 and CCSM4 underestimate the seasonal mean precipitation, which is a common problem in the current generation of climate models. The dry bias in SP-CCSM4 results from a northward-displaced WNPSH in the model, and the less moisture transport over the EASM region. Despite the dry bias of the seasonal mean state, the annual cycle of the EASM is still better simulated by SP-CCSM4 than CCSM4. In CCSM4, the EASM onset at mid-May is not reproduced, plus the whole subtropical rain band is displaced northward. The SP-CCSM4 simulates a more reasonable monsoon onset and a stepwise northward propagation. However, the northward propagation of the EASM is faster in SP-CCSM4, leading to an earlier onset and shorter duration of the Mei-yu season. The SP-CCSM4 also captures the mechanisms related to the northward propagation of the EASM ISO. The ISO related convective heating over the Maritime Continent and SCS induces a low-level cyclonic anomaly to its northwest. The northeasterly anomaly on the northern side of the abnormal cyclonic system reduces the prevailing southwesterly flow, thus decreasing the latent heat flux and leading to a warmer SST to the north of the convection center. The warmer SST tends to destabilize the atmospheric boundary layer, therefore favoring the northward propagation of convection. Meanwhile, the presence of the easterly vertical shear and the barotropic vorticity to the north of the convective activity also contributes to the northward propagation of ISO. The faster northward propagation of the ISO in SP-CCSM4 could be attributed to the suppressed convection over WPWP, which is the largest difference between SP-CCSM4 and observation. This hypothesis is tested using observational data. However, the short record of the observation limits the further investigation.

Under the global warming background, the observed changes of the EASM have been documented by several studies (e.g., Jiang and Wang, 2013; Li et al., 2010; Zhang et al., 2013; Zhang, 2015; Zuo et al., 2012). The response of the EASM to global warming scenario has also been studied using numerical models (e.g., Kripalani et al., 2007; Lee and Wang, 2014; Sun and Ding, 2010). How the EASM would change in a warmer climate in a super-parameterized model is not known, and therefore, the response of EASM to global warming is analyzed using SP-CCSM4. Under a global warming scenario, the mean state of the EASM is intensified, with an enhanced precipitation and monsoon circulation. In addition, the annual cycle of the EASM is changed. The monsoon onset is delayed for about five days, the Mei-yu/Baiu/Changma lasts longer, as well as the rainy episode over the northern East Asian. These changes are in agreement with other model simulations (e.g., Kitoh and Uchiyama, 2006; Kripalani et al., 2007; Lee and Wang, 2014; Sun and Ding, 2010). Moreover, the interannual variability of the EASM varies in the warming climate. There is more precipitation in the northern part of East Asia, and the year-to-year variability is amplified. However, the intraseasonal variability of the EASM does not show a big difference in the warming climate. The EASM changes in a warmer climate is related to the changes in WNPSH. In the mean state, the warming of ocean surface results in a diabatic cooling over subtropical WP. The diabatic cooling leads to a high GPH anomaly and resultant amplified WNPSH, which enhances the southwesterly flow and moisture transport over East Asia.

A hypothesis is proposed to explain the future changes of the EASM based on the analysis of its mean state under various global warming scenarios. Since the EASM precipitation is tightly associated with the WNPSH, the mechanism responsible for the changes in the WNPSH explains the EASM variation in the warmer climate. The changes of the WNPSH in a warmer climate are affected by two factors, one is the warming of boundary conditions, and the other is the convection over tropical SCS and nearby WP. The warming of boundary conditions plays a more important role than the atmospheric warming. It favors the amplification of the WNPSH. At meantime, the strong convection due to the lack of air-sea interaction prevents the WNPSH from extending westward. To test this hypothesis two numerical experiments were designed. The first experiment tests how the ocean mean state influences the atmosphere. The second experiment intends to prove that the suppressed convective activity due to the lack of the air-sea interaction over SCS and adjacent WP favors the westward extension of the WNPSH. The hypothesis is confirmed by analyzing the mean state and interannual variability of the EASM in these model experiments. It reveals that the reduced convection over SCS and tropical WP induces an anti-cyclonic circulation to its northwest, plus a Rossby wave train from tropical to mid-latitude Pacific Ocean. The westerly anomaly on the northern side of the anti-cyclonic circulation intensifies the mean westerly/southwesterly flow, amplifying the western edge of the WNPSH and strengthening the monsoon circulation, and thus favoring the westward extension of the WNPSH. However, the influence of the convection over tropical SCS and WP on the WNPSH can only persists from May to June. During July and August the changes in WNPSH is more due to the systems at mid-latitudes.

To summarize, the performance of the EASM simulation by SP-CCSM4 is evaluated for the first time. Compared to the model which uses conventional parameterization, SP-CCSM4 has a better skill in simulating the main characteristics of EASM, including the mean state, onset and seasonal march, and also captures the mechanisms related to the northward propagation of the intraseasonal variability. The EASM response to global warming scenario in SP-CCSM4 is also analyzed for the first time. The changes in the EASM is in agreement with previous model studies (e.g., Kripalani et al., 2007; Lee and Wang, 2014; Sun and Ding, 2010). This study further investigated the mechanisms responsible for the EASM changes in the warmer climate, and analyzed the influences of warmer boundary conditions and convective activity over tropical SCS and WP on the changes of WNPSH, which is overlooked in previous studies (e.g., Wang et al., 2013; Xiang et al., 2013; Zhou et al., 2009). It also pointed out that the impact of the tropical convection can only lasts during early summer.

6.2 Discussion

As mentioned above, SP-CCSM4 has a better skill in simulating the EASM than CCSM. However, it is not fully understood whether the outperformance is due to the CRMs used in SP-CCSM4. In addition, the variance of the 30-60-day bandfiltered OLR is largely amplified in SP-CCSM4 (Fig. 3.10). It needs further analysis to explain if it also attributed to the CRMs in SP-CCSM4. These questions may have answers by running uncoupled simulations, for instance, SP-CAM with SSTs from the coupled CCSM4 simulation, or CAM4 with SSTs from coupled SP-CCSM4 simulation.

It is proposed that, the faster northward propagation of the intraseasonal oscillation is attributed to the dry condition over WPWP simulated by SP-CCSM4. However, this hypothesis was not analyzed due to the short record of the observational data. It worths further investigation in future to study the difference in the intraseasonal oscillation of the EASM due to the thermal conditions over WPWP.

Regarding the mechanisms responsible for the EASM changes in the warmer climate, one of the shortcomings in the model experiment is the method of LHFLX modification. In order to mimic the air-sea interaction over tropical SCS and WP in cpl_4×CO_2, the LHFLX in amip_4×CO_2sst_lhflx over these regions was modified by adding the climatological MJJA mean LHFLX difference between cpl_4×CO_2 and amip_4×CO_2sst from May to August in each year. In this method, the decrease of the seasonal mean LHFLX in amip_4×CO_2sst_lhflx is reasonably reproduced, however, it may mask the month-by-month changes of the LHFLX over tropics. Moreover, only the LHFLX during May to August was changed over tropical area, whether the changes of LHFLX in other seasons has an impact on the WNPSH was not investigated.

Bibliography

Barnett, T. P. and R. Preisendorfer, 1987: Origins and Levels of Monthly and Seasonal Forecast Skill for United States Surface Air Temperatures Determined by Canonical Correlation Analysis. *Mon. Wea. Rev.*, **115 (9)**, 1825–1850, doi:10.1175/1520-0493(1987)115⟨1825:OALOMA⟩2.0.CO;2.

Bretherton, C. S., P. N. Blossey, and C. Stan, 2014: Cloud feedbacks on greenhouse warming in the superparameterized climate model SP-CCSM4. *J. Adv. Model. Earth Syst.*, **6 (4)**, 1185–1204, doi:10.1002/2014MS000355, URL `http://dx.doi.org/10.1002/2014MS000355`.

Chai, T. and R. R. Draxler, 2014: Root mean square error (RMSE) or mean absolute error (MAE)? Arguments against avoiding RMSE in the literature. *Geosci. Model Dev.*, **7 (3)**, 1247–1250, doi:10.5194/gmd-7-1247-2014, URL `http://www.geosci-model-dev.net/7/1247/2014/`.

Chan, J. C., W. Ai, and J. Xu, 2002: Mechanisms Responsible for the Maintenance of the 1998 South China Sea Summer Monsoon. *J. Meteor. Soc. Japan*, **80 (5)**, 1103–1113, doi:10.2151/jmsj.80.1103.

Chan, S. C. and S. Nigam, 2009: Residual Diagnosis of Diabatic Heating from ERA-40 and NCEP Reanalyses: Intercomparisons with TRMM. *J. Climate*, **22 (2)**, 414–428, doi:10.1175/2008JCLI2417.1, URL `http://dx.doi.org/10.1175/2008JCLI2417.1`.

Chen, H., T. Zhou, R. B. Neale, X. Wu, and G. Zhang, 2010: Performance of the New NCAR

CAM3.5 in East Asian Summer Monsoon Simulations: Sensitivity to Modifications of the Convection Scheme. *J. Climate*, **23**, 3657–3675, doi:10.1175/2010JCLI3022.1.

Chen, T.-C. and J.-M. Chen, 1995: An Observational Study of the South China Sea Monsoon during the 1979 Summer: Onset and Life Cycle. *Mon. Wea. Rev.*, **123 (8)**, 2295–2318, doi:10.1175/1520-0493(1995)123⟨2295:AOSOTS⟩2.0.CO;2, URL `http://dx.doi.org/10.1175/1520-0493(1995)123<2295:AOSOTS>2.0.CO;2`.

Dee, D. P., et al., 2011: The ERA-Interim reanalysis: configuration and performance of the data assimilation system. *Quart. J. Roy. Meteor. Soc.*, **137 (656)**, 553–597, doi:10.1002/qj.828, URL `http://dx.doi.org/10.1002/qj.828http://onlinelibrary.wiley.com/store/10.1002/qj.828/asset/828_ftp.pdf?v=1&t=ij1q7zy4&s=025bd165ac35e6a646ab54d437d1ba7e8d1b5715`.

DeMott, C., C. Stan, and D. A. Randall, 2013: Northward Propagation Mechanisms of the Boreal Summer Intraseasonal Oscillation in the ERA-Interim and SP-CCSM. *J. Climate*, **26**, 1973–1992, doi:10.1175/JCLI-D-12-00191.1.

DeMott, C. A., C. Stan, D. A. Randall, J. L. Kinter III, and M. Khairoutdinov, 2011: The Asian Monsoon in the Superparameterized CCSM and Its Relationship to Tropical Wave Activity. *J. Climate*, **24 (19)**, 5134–5156, doi:10.1175/2011JCLI4202.1, URL `http://dx.doi.org/10.1175/2011JCLI4202.1`, `http://dx.doi.org/10.1175/2011JCLI4202.1`.

Ding, Y., 1992: Summer Monsoon Rainfalls in China. *J. Meteor. Soc. Japan*, **70**, 373–396.

Ding, Y. and J. C. Chan, 2005: The East Asian summer monsoon: an overview. *Meteor. Atmos. Phys.*, **89**, 117–142, doi:10.1007/s00703-005-0125-z.

Ding, Y., H. Wang, and B. Wang, 2005: East Asian Monsoon: East Aisa. *International Committee of the Third International Workshop on Monsoons (IWM-III)*, C.-P. Chang, B. Wang, and N.-C. G. Lau, Eds., 95–114.

Drbohlav, H.-K. L. and B. Wang, 2005: Mechanism of the Northward–Propagating Intraseasonal Oscillation: Insights from a Zonally Symmetric Model. *J. Climate*, **18**, 952–972, doi:10.1175/JCLI3306.1.

Gill, A., 1980: Some simple solutions for heat-induced tropical circulation. *Quart. J. Roy. Meteor. Soc.*, **106**, 447–462.

Grabowski, W. W., 2001: Coupling Cloud Processes with the Large-Scale Dynamics Using the Cloud-Resolving Convection Parameterization (CRCP). *J. Atmos. Sci.*, **58 (9)**, 978–997, doi:10.1175/1520-0469(2001)058⟨0978:CCPWTL⟩2.0.CO;2.

Grabowski, W. W., 2002: Large-scale organization of moist convection in idealized aqua-planet simulations. *Int. J. Numer. Meth. Fluids*, **39 (9)**, 843–853.

Guo, Q.-Y., 1983: The summer monsoon intensity index in East Asia and its variation. *Acta Geographica Sinica*, **38 (3)**, 207–217, in Chinese.

He, C. and T. Zhou, 2014: The two interannual variability modes of the Western North Pacific Subtropical High simulated by 28 CMIP5–AMIP models. *Climate Dyn.*, **43 (9)**, 2455–2469, doi:10.1007/s00382-014-2068-x, URL `http://dx.doi.org/10.1007/s00382-014-2068-x`.

He, J., 2009: A review of the Asian-Pacific Monsoon. *Atmos. and Ocn. Sci. Lett*, **2 (2)**, 91–96.

He, J., J. Ju, Z. Wen, L. Junmei, and Q. Jin, 2007: A Review of Recent Advances in Research on Asian Monsoon in China. *Adv. Atmos. Sci*, **24 (6)**, 972–992.

He, J., B. Zhou, M. Wen, and F. Li, 2001: Vertical Circulation Structure, Interannual Variation Features and Variation Mechanism of Western Pacific Subtropical High. *Adv. Atmos. Sci*, **18 (4)**, 497–510, doi:10.1007/s00376-001-0040-2.

Hsu, H.-H. and C.-H. Weng, 2001: Northwestward Propagation of the Intraseasonal Oscillation in the Western North Pacific during the Boreal Summer: Structure and Mechanism. *J. Climate*, **14**, 3834–3850, doi:10.1175/1520-0442(2001)014⟨3834:NPOTIO⟩2.0.CO;2.

Hu, Z.-Z., S. Yang, and R. Wu, 2003: Long-term climate variations in China and global warming signals. *J. Geophys. Res.: Atmospheres*, **108 (D19)**.

Huang, R. and F. Sun, 1992: Impacts of the Tropical Western Pacific on the East Asian Summer Monsoon. *J. Meteor. Soc. Japan*, **70 (1B)**, 243–256.

Huang, R., L. Zhou, and W. Chen, 2003: The Progresses of Recent Studies on the Variabilities of the East Asian Monsoon and Their Causes. *Adv. Atmos. Sci*, **20 (1)**, 55–69, doi:10.1007/BF03342050.

Huffman, G. J., et al., 1997: The Global Precipitation Climatology Project (GPCP) Combined Precipitation Dataset. *Bull. Amer. Meteor. Soc*, **78 (1)**, 5–20, doi:10.1175/1520-0477(1997)078⟨0005:TGPCPG⟩2.0.CO;2.

Jiang, D. and H. Wang, 2013: Natural interdecadal weakening of East Asian summer monsoon in the late 20th century. *Chinese Science Bulletin*, **50 (17)**, 1923–1929, doi:10.1360/982005-36, URL `http://dx.doi.org/10.1360/982005-36`.

Jiang, X., T. Li, and B. Wang, 2004: Structures and Mechanisms of the Northward Propagating Boreal Summer Intraseasonal Oscillation. *J. Climate*, **17**, 1022–1039, doi:10.1175/1520-0442(2004)017⟨1022:SAMOTN⟩2.0.CO;2.

Jin, Y. and C. Stan, 2016: Simulation of East Asian Summer Monsoon (EASM) in SP-CCSM4: Part I–Seasonal mean state and intraseasonal variability. *J. Geophys.Res. Atmos.*, **121**, doi:0.1002/2015JD024035.

Ju, J.-h., C. Qian, and J. Cao, 2005: The intraseasonal oscillation of East Asian summer monsoon. *Chinese J. Atmos. Sci*, **29 (2)**, 187–194, in Chinese.

Kalnay, E., et al., 1996: The NCEP/NCAR 40-year Reanalysis Project. *Bull. Amer. Meteor. Soc*, **77 (3)**, 437–471, doi:10.1175/1520-0477(1996)077⟨0437:TNYRP⟩2.0.CO;2.

Kemball-Cook, S. and B. Wang, 2001: Equatorial Waves and Air–Sea Interaction in the Boreal Summer Intraseasonal Oscillation. *J. Climate*, **14**, 2923–2942, doi:10.1175/1520-0442(2001)014⟨2923:EWAASI⟩2.0.CO;2.

Khairoutdinov, M. F. and D. A. Randall, 2001: A cloud resolving model as a cloud parameterization in the NCAR Community Climate System Model: Preliminary Results. *Geophys. Res. Lett.*, **28**, 3617–3620, doi:10.1029/2001GL013552.

Kitoh, A. and T. Uchiyama, 2006: Changes in Onset and Withdrawal of the East Asian Summer Rainy Season by Multi-Model Global Warming Experiments. *J. Meteor. Soc. Japan*, **84 (2)**, 247–258, doi:10.2151/jmsj.84.247, URL `https://www.jstage.jst.go.jp/article/jmsj/84/2/84_2_247/_pdf`.

Kripalani, R. H., J. H. Oh, and H. S. Chaudhari, 2007: Response of the East Asian summer monsoon to doubled atmospheric CO2: Coupled climate model simulations and projections under IPCC AR4. *Theor. Appl. Climatol.*, **87**, 1–28, doi:10.1007/s00704-006-0238-4.

Krishnamurthy, V., C. Stan, D. A. Randall, R. P. Shukla, and J. L. Kinter III, 2014: Simulation of the South Asian Monsoon in a Coupled Model with an Embedded Cloud-Resolving Model. *J. Climate*, **27 (3)**, 1121–1142, doi:10.1175/JCLI-D-13-00257.1, URL `http://dx.doi.org/10.1175/JCLI-D-13-00257.1`, `http://dx.doi.org/10.1175/JCLI-D-13-00257.1`.

Kusunoki, S. and O. Arakawa, 2012: Change in the precipitation intensity of the East Asian summer monsoon projected by CMIP3 models. *Clim. Dyn.*, **38**, 2055–2072, doi:10.1007/s00382-011-1234-7.

Kusunoki, S. and O. Arakawa, 2015: Are CMIP5 Models Better than CMIP3 Models in Simulating Precipitation over East Asia? *J. Climate*, **28 (14)**, 5601–5621, doi:10.1175/

JCLI-D-14-00585.1, URL http://dx.doi.org/10.1175/JCLI-D-14-00585.1http://journals.ametsoc.org/doi/abs/10.1175/JCLI-D-14-00585.1.

Lau, K.-M. and H. Weng, 2002: Recurrent teleconnection patterns linking summertime precipitation variability over East Asia and North America. *J. Meteor. Soc. Japan*, **80 (6)**, 1309–1324.

Lau, K.-M., G. J. Yang, and S. H. Shen, 1988: Seasonal and Intraseasonal Climatology of Summer Monsoon Rainfall over Eeat Asia. *Mon. Wea. Rev.*, **116 (1)**, 18–37, doi:10.1175/1520-0493(1988)116⟨0018:SAICOS⟩2.0.CO;2, URL http://dx.doi.org/10.1175/1520-0493(1988)116<0018:SAICOS>2.0.CO;2.

Lee, J.-Y. and B. Wang, 2014: Future change of global monsoon in the CMIP5. *Climate Dyn.*, **42 (1-2)**, 101–119, doi:10.1007/s00382-012-1564-0.

Li, C. and L. Zhang, 1999: Activity of the South China Sea summer monsoon and it effect. *Acta Atmos Sinica*, **23**, 257–266.

Li, J., Z. Wu, Z. Jiang, and J. He, 2010: Can Global Warming Strengthen the East Asian Summer Monsoon? *J. Climate*, **23 (24)**, 6696–6705, doi:10.1175/2010JCLI3434.1, URL http://dx.doi.org/10.1175/2010JCLI3434.1, http://dx.doi.org/10.1175/2010JCLI3434.1.

Li, W., L. Li, M. Ting, and Y. Liu, 2012: Intensification of Northern Hemisphere subtropical highs in a warming climate. *Nature Geoscience*, **5 (11)**, 830–834.

Liebmann, B. and C. A. Smith, 1996: Description of a Complete (Interpolated) Outgoing Longwave Radiation Dataset. *Bull. Amer. Meteor. Soc*, **77**, 1275–1277.

Lu, R., 2001: Interannual Variability of the Summertime North Pacific Subtropical High and its Relation to Atmospheric Convection over the Warm Pool. *J. Meteor. Soc. Japan*, **79 (3)**, 771–783, doi:10.2151/jmsj.79.771.

Lu, R. and B. Dong, 2001: Westward Extension of North Pacific Subtropical High in Summer. *J. Meteor. Soc. Japan.*, **79 (6)**, 1229–1241, doi:10.2151/jmsj.79.1229.

Lu, R., Y. Li, and C.-S. Ryu, 2008: Relationship between the zonal displacement of the western Pacific subtropical high and the dominant modes of low-tropospheric circulation in summer. *Progress in Natural Science*, **18 (2)**, 161–165, doi:10.1016/j.pnsc.2007.07.009.

Mao, J. and J. C. L. Chan, 2005: Intraseasonal Variability of the South China Sea Summer Monsoon. *J. Climate*, **18 (13)**, 2388–2402, doi:10.1175/JCLI3395.1, URL `http://dx.doi.org/10.1175/JCLI3395.1`.

Mao, J., Z. Sun, and G. Wu, 2010: 20-50-day oscillation of summer Yangtze rainfall in response to intraseasonal variations in the subtropical high over the western North Pacific and South China Sea. *Clim. Dyn.*, **34**, 747–761, doi:10.1007/s00382-009-0628-2.

McCrary, R. R., D. A. Randall, and C. Stan, 2014: Simulations of the West African Monsoon with a Superparameterized Climate Model. Part I: The Seasonal Cycle. *J. Climate*, **27 (22)**, 8303–8322, doi:10.1175/JCLI-D-13-00676.1, URL `http://dx.doi.org/10.1175/JCLI-D-13-00676.1`, `http://dx.doi.org/10.1175/JCLI-D-13-00676.1`.

Neale, R. B., J. Richter, S. Park, P. H. Lauritzen, S. J. Vavrus, P. J. Rasch, and M. Zhang, 2013: The Mean Climate of the Community Atmosphere Model (CAM4) in Forced SST and Fully Coupled Experiments. *J. Climate*, **26 (14)**, 5150–5168, doi:10.1175/JCLI-D-12-00236.1, URL `http://dx.doi.org/10.1175/JCLI-D-12-00236.1`.

Nigam, S., 1997: The Annual Warm to Cold Phase Transition in the Eastern Equatorial Pacific: Diagnosis of the Role of Stratus Cloud-Top Cooling. *J. Climate*, **10**, 2447–2467, doi:10.1175/1520-0442(1997)010⟨2447:TAWTCP⟩2.0.CO;2.

Nigam, S., C. Chung, and E. DeWeaver, 2000: ENSO Diabatic Heating in ECMWF and NCEP–NCAR Reanalyses, and NCAR CCM3 Simulation. *J. Climate*, **13 (17)**, 3152–3171, doi:10.1175/1520-0442(2000)013⟨3152:EDHIEA⟩2.0.CO;2, URL `http://dx.doi.org/10.1175/1520-0442(2000)013<3152:EDHIEA>2.0.CO;2`.

Qian, W., H.-S. Kang, and D.-K. Lee, 2002: Distribution of seasonal rainfall in the East Asian monsoon region. *Theor. Appl. Climatol.*, **73 (3)**, 151–168, doi:10.1007/s00704-002-0679-3, URL `http://dx.doi.org/10.1007/s00704-002-0679-3`.

Qian, W. and D.-K. Lee, 2000: Seasonal march of Asian summer monsoon. *Int. J. Climatol.*, **20 (11)**, 1371–1386.

Rajendran, K., A. Kitoh, and S. Yukimoto, 2004: South and East Asian Summer Monsoon Climate and Variation in the MRI Coupled Model (MRI-CGCM2). *J. Climate*, **17**, 763–782, doi:10.1175/1520-0442(2004)017⟨0763:SAEASM⟩2.0.CO;2.

Randall, D., et al., 2007: *Cilmate Models and Their Evaluation*, book section 8. Cambridge University Press, Cambridge, United Kingdom and New York, NY, USA.

Reynolds, R., N. Rayner, T. Smith, D. Stokes, and W. Wang, 2002: An improved in situ and satellite SST analysis for climate. *J. Climate*, **15**, 1609–1625, doi:10.1175/1520-0442(2002)015⟨1609:AIISAS⟩2.0.CO;2.

Rodwell, M. J. and B. J. Hoskins, 1996: Monsoons and the dynamics of deserts. *Quart. J. Roy. Meteor. Soc.*, **122 (534)**, 1385–1404, doi:10.1002/qj.49712253408, URL `http://dx.doi.org/10.1002/qj.49712253408`.

Seo, K.-H., J. Ok, J.-H. Son, and D.-H. Cha, 2013: Assessing Future Changes in the East Asian Summer Monsoon Using CMIP5 Coupled Models. *J. Climate*, **26 (19)**, 7662–7675, doi:10.1175/JCLI-D-12-00694.1, URL `http://dx.doi.org/10.1175/JCLI-D-12-00694.1`.

Song, F. and T. Zhou, 2014: Interannual Variability of East Asian Summer Monsoon Simulated by CMIP3 and CMIP5 AGCMs: Skill Dependence on Indian Ocean–Western Pacific Anticyclone Teleconnection. *J. Climate*, **27 (4)**, 1679–1697, doi:10.1175/JCLI-D-13-00248.1, URL `http://dx.doi.org/10.1175/JCLI-D-13-00248.1`.

Sperber, K. R., H. Annamalai, I.-S. Kang, A. Kitoh, A. Moise, A. Turner, B. Wang, and T. Zhou, 2013: The Asian summer monsoon: an intercomparison of CMIP5 vs. CMIP3 simulations of the late 20th century. *Climate Dyn.*, **41 (9-10)**, 2711–2744, doi:10.1007/s00382-012-1607-6.

Stan, C. and L. Xu, 2014: Climate simulations and projections with a super-parameterized climate model. *Environmental Modeling & Software*, **60**, 134–152, doi:http://dx.doi.org/10.1016/j.envsoft.2014.06.013, URL `http://www.sciencedirect.com/science/article/pii/S1364815214001789http://ac.els-cdn.com/S1364815214001789/1-s2.0-S1364815214001789-main.pdf?_tid=bc9d43d6-c606-11e5-82b9-00000aab0f26&acdnat=1454016974_6d64591303d2455e330d74f951ef3138`.

Stocker, T. F., et al., 2013: Climate change 2013: the physical science basis. Intergovernmental panel on climate change, working group I contribution to the IPCC fifth assessment report (AR5). New York: Cambridge University Press.

Sun, S. and M. Ying, 1999: Subtropical High Anomalies over the Western Pacific and Its Relations to the Asian Monsoon and SST Anomaly. *Adv. Atmos. Sci*, **16 (4)**, 559–568, doi:10.1007/s00376-999-0031-2.

Sun, Y. and Y. Ding, 2010: A projection of future changes in summer precipitation and monsoon in East Asia. *SCIENCE CHINA Earth Sciences*, **53 (2)**, 284–300, doi:10.1007/s11430-009-0123-y, URL `http://earth.scichina.com:8080/sciDehttp://link.springer.com/article/10.1007\%2Fs11430-009-0123-y`.

Tao, S. and L. Chen, 1987: *A review of recent research on the East Asian Monsoon in China*, 60–92. Oxford University Press, London.

Tao, S.-y. and Y.-h. Ding, 1981: Observational Evidence of the Influence of the Qinghai-Xizang (Tibet) Plateau on the Occurrence of Heavy Rain and Severe Convective Storms in China. *Bull. Amer. Meteor. Soc.*, **62 (1)**, 23–30, doi:10.1175/1520-0477(1981)062⟨0023:

OEOTIO⟩2.0.CO;2, URL http://dx.doi.org/10.1175/1520-0477(1981)062<0023:OEOTIO>2.0.CO;2.

Tsou, C.-H., P.-C. Hsu, W.-S. Kau, and H.-H. Hsu, 2005: Northward and Northwestward Propagation of 30-60 Day Oscillation in the Tropical and Extratropical Western North Pacific. *J. Meteor. Soc. Japan*, **83 (5)**, 711–726, doi:10.2151/jmsj.83.711.

Wang, B., 1992: The Vertical Structure and Development of the ENSO Anomaly Mode during 1979-1989. *J. Atmos. Sci.*, **49 (8)**, 698–712, doi:10.1175/1520-0469(1992)049⟨0698:TVSADO⟩2.0.CO;2, URL http://dx.doi.org/10.1175/1520-0469(1992)049<0698:TVSADO>2.0.CO;2, http://dx.doi.org/10.1175/1520-0469(1992)049<0698:TVSADO>2.0.CO;2.

Wang, B., F. Huang, Z. Wu, J. Yang, X. Fu, and K. Kikuchi, 2009: Multi-scale climate variability of the South China Sea monsoon: A review. *Dyn. Atmos. Ocn.*, **47 (1-3)**, 15–37, doi:10.1016/j.dynatmoce.2008.09.004.

Wang, B., T. Li, Y. Ding, R. Zhang, and H. Wang, 2005: East Asian-Western North Pacific Monsoon: A Distinctive Component of the Asian-Australian Monsoon System. *International Committee of the Third International Workshop on Monsoons (IWM-III)*, C.-P. Chang, B. Wang, and N.-C. Lau, Eds., 72–94.

Wang, B., R. Wu, and X. Fu, 2000: Pacific–East Asian Teleconnection: How Does ENSO Affect East Asian Climate? *J. Climate*, **13 (9)**, 1517–1536, doi:10.1175/1520-0442(2000)013⟨1517:PEATHD⟩2.0.CO;2, URL http://dx.doi.org/10.1175/1520-0442(2000)013<1517:PEATHD>2.0.CO;2.

Wang, B., R. Wu, and K.-M. Lau, 2001: Interannual Variability of the Asian Summer Monsoon: Contrasts between the Indian and the Western North PacificEast Asian Monsoons. *J. Climate*, **14 (20)**, 4073–4090, doi:10.1175/1520-0442(2001)014⟨4073:IVOTAS⟩2.0.CO;2, URL http://dx.doi.org/10.1175/1520-0442(2001)014<4073:IVOTAS>2.0.CO;2.

Wang, B., Z. Wu, J. Li, J. Liu, C.-P. Chang, Y. Ding, and G. Wu, 2008: How to Measure the Strength of the East Asian Summer Monsoon. *J. Climate*, **21 (17)**, 4449–4463, doi:10.1175/2008JCLI2183.1, URL http://dx.doi.org/10.1175/2008JCLI2183.1http://journals.ametsoc.org/doi/pdf/10.1175/2008JCLI2183.1.

Wang, B., B. Xiang, and J.-Y. Lee, 2013: Subtropical high predictability establishes a promising way for monsoon and tropical storm predictions. *Proc. Natl. Acad. Sci.*, **110 (8)**, 2718–2722, URL http://www.ncbi.nlm.nih.gov/pmc/articles/PMC3581955/pdf/pnas.201214626.pdf.

Wang, B. and X. Xu, 1997: Northern Hemisphere Summer Monsoon Singularities and Climatological Intraseasonal Oscillation. *J. Climate*, **10 (5)**, 1071–1085, doi:10.1175/1520-0442(1997)010⟨1071:NHSMSA⟩2.0.CO;2, URL http://dx.doi.org/10.1175/1520-0442(1997)010<1071:NHSMSA>2.0.CO;2.

Wang, B. and Q. Zhang, 2002: Pacific–East Asian Teleconnection. Part II: How the Philippine Sea Anomalous Anticyclone is Established during El Nino Development. *J. Climate*, **15**, 3252–3265, doi:10.1175/1520-0442(2002)015⟨3252:PEATPI⟩2.0.CO;2.

Wang, H., 2000: The interannual variability of East Asian Monsoon and its relationship with SST in a coupled Atmosphere-Ocean-Land climate model. *Advances in Atmospheric Sciences*, **17 (1)**, 31–47, URL http://search.proquest.com.mutex.gmu.edu/docview/198361874?accountid=14541, copyright - Advances in Atmospheric Sciences 2000; Document feature - ; Last updated - 2014-08-30.

Wang, H., 2001: The weakening of the Asian monsoon circulation after the end of 1970's. *Advances in Atmospheric Sciences*, **18 (3)**, 376–386, URL http://search.proquest.com.mutex.gmu.edu/docview/198304691?accountid=14541, copyright - Advances in Atmospheric Sciences 2001; Document feature - ; Last updated - 2014-08-30.

Willmott, C. J. and K. Matsuura, 2005: Advantages of the mean absolute error (MAE) over the root mean square error (RMSE) in assessing average model performance. *Clim Res*, **30 (1)**, 79–82, URL `http://www.int-res.com/abstracts/cr/v30/n1/p79-82/`.

Xiang, B., B. Wang, W. Yu, and S. Xu, 2013: How can anomalous western North Pacific Subtropical High intensify in late summer? *Geophys. Res. Lett.*, **40 (10)**, 2349–2354.

Xie, P. and P. A. Arkin, 1997: Global Precipitation: A 17-Year Monthly Analysis Based on Gauge Observations, Satellite Estimates, and Numerical Model Outputs. *Bull. Amer. Meteor. Soc.*, **78 (11)**, 2539–2558, doi:10.1175/1520-0477(1997)078⟨2539:GPAYMA⟩2.0.CO;2, URL http://dx.doi.org/10.1175/1520-0477(1997)078<2539:GPAYMA>2.0.CO;2.

Xu, G. and Q. Zhu, 2002: Feature analysis of summer monsoon LFO over SCS in 1998. *J. Tropical Meteor.*, **18**, 309–316, in Chinese.

Xu, Q., 2001: Abrupt change of the mid-summer climate in central east China by the influence of atmospheric pollution. *Atmospheric Environment*, **35 (30)**, 5029 – 5040, doi: http://dx.doi.org/10.1016/S1352-2310(01)00315-6, URL `http://www.sciencedirect.com/science/article/pii/S1352231001003156`, visibility, Aerosol and Atmospheric Optics.

Xue, F., 2001: Interannual to interdecadal variation of east asian summer monsoon and its association with the global atmospheric circulation and sea surface temperature. *Advances in Atmospheric Sciences*, **18 (4)**, 567–575, URL `http://search.proquest.com.mutex.gmu.edu/docview/198304371?accountid=14541`, copyright - Advances in Atmospheric Sciences 2001; Document feature - ; Last updated - 2014-08-30.

Yang, H. and S. Sun, 2003: Longitudinal Displacement of the Subtropical High in the Western Pacific in Summer and its Influence. *Adv. Atmos. Sci*, **20 (6)**, 921–933, doi: 10.1007/BF02915515.

Yu, R. and T. Zhou, 2007: Seasonality and Three-Dimensional Structure of Interdecadal Change in the East Asian Monsoon. *J. Climate*, **20 (21)**, 5344–5355, doi:10.1175/2007JCLI1559.1, URL `http://dx.doi.org/10.1175/2007JCLI1559.1`.

Zhang, L., B. Wang, and Q. Zeng, 2009: Impact of the Madden–Julian Oscillation on Summer Rainfall in Southeast China. *J. Climate*, **22**, 201–217, doi:10.1175/2008JCLI1959.1.

Zhang, Q. and S. Tao, 1999: The Study of the Sudden northward jump of the Subtropical High over the Western Pacific. *Acta Meteor. Sinicac*, **57**, 539–548.

Zhang, R., B. Wu, J. Han, and Z. Zuo, 2013: *Effects on Summer Monsoon and Rainfall Change Over China due to Eurasian Snow Cover and Ocean Thermal Conditions.* INTECH Open Access Publisher, 227–250 pp.

Zhang, R.-H., 2015: Natural and human-induced changes in summer climate over the East Asian monsoon region in the last half century: A review. *Advances in Climate Change Research*, **6 (2)**, 131–140.

Zhou, T., et al., 2009: Why the Western Pacific Subtropical High Has Extended Westward since the Late 1970s. *J. Climate*, **22**, 2199–2215, doi:10.1175/2008JCLI2527.1.

Zhou, T.-J. and Z.-X. Li, 2002: Simulation of the east asian summer monsoon using a variable resolution atmospheric GCM. *Clim. Dyn.*, **19**, 166–180, doi:10.1007/s00382-001-0214-8.

Zhu, C., W.-S. Lee, H. Kang, and C.-K. Park, 2005: A proper monsoon index for seasonal and interannual variations of the East Asian monsoon. *Geophys. Res. Lett.*, **32 (2)**, n/a–n/a, doi:10.1029/2004GL021295, URL `http://dx.doi.org/10.1029/2004GL021295`, l02811.

Zhu, C., B. Wang, W. Qian, and B. Zhang, 2012: Recent weakening of northern East Asian summer monsoon: A possible response to global warming. *Geophys. Res. Lett.*,

39 (9), URL http://search.proquest.com.mutex.gmu.edu/docview/1013533253?accountid=14541.

Zuo, Z., S. Yang, A. Kumar, R. Zhang, Y. Xue, and B. Jha, 2012: Role of Thermal Condition over Asia in the Weakening Asian Summer Monsoon under Global Warming Background. *J. Climate*, **25 (9)**, 3431–3436, doi:10.1175/JCLI-D-11-00742.1, URL http://dx.doi.org/10.1175/JCLI-D-11-00742.1, http://dx.doi.org/10.1175/JCLI-D-11-00742.1.

Curriculum Vitae

Yan Jin grew up in Wuxi, Jiangsu province, People's Republic of China. She graduated from Nanjing University of Information Science & Technology (former Nanjing Institute of Meteorology) in 2010 where she received a Bachelor of Science degree in Atmospheric Sciences. In 2012 Yan started her Ph.D. at George Mason University under Dr. Cristiana Stan.

During her Ph.D. study, Yan worked on topics related to the intraseasonal variability of the East Asian Summer Monsoon (EASM), and the mechanisms explaining the EASM response to global warming scenario. She used a climate model and designed numerical experiments in her study. Parts of her work has been presented at the American Geophysical Union (AGU) Fall Meeting, Center for Multiscale Modeling of Atmospheric Process (CMMAP) Team Meeting, and has been published online in a peer-reviewed journal: Journal of Geophysical Research-Atmospheres.